

DTIC FILE COPY

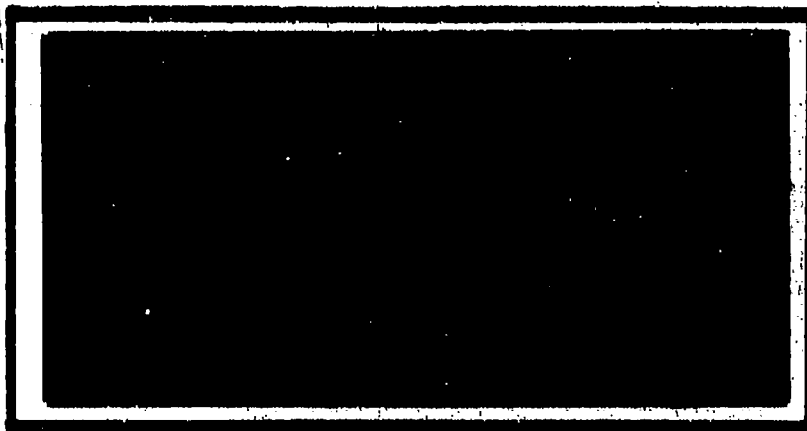
AD-A230 534



DTIC
ELECTE
JAN 07 1991

D

D



DISTRIBUTION STATEMENT A

Approved for public release;
Distribution Unlimited

DEPARTMENT OF THE AIR FORCE
AIR UNIVERSITY
AIR FORCE INSTITUTE OF TECHNOLOGY

Wright-Patterson Air Force Base, Ohio

91 1 3 105

AFIT/GEO/ENP/90D-1

①

DTIC
ELECTE
JAN 07 1991
S D D

DETECTION OF HIGH ALTITUDE
AIRCRAFT WAKE VORTICES
USING INFRARED DOPPLER LIDAR:
AN ASSESSMENT

THESIS

Michael J. Estes, Captain, USAF

AFIT/GEO/ENP/90D-1

Approved for public release; distribution unlimited

REPORT DOCUMENTATION PAGE			Form Approved OMB No 0704-0188	
<small>Public reporting burden for this section of information is estimated to average 1 hour per response, including the time for reviewing instructions, searching existing data sources, gathering and maintaining the data needed, and completing and reviewing the collection of information. Send comments regarding this burden estimate or any other aspect of this collection of information, including suggestions for reducing this burden, to Washington Headquarters Services, Directorate for Information Operations and Reports, 1215 Jefferson Davis Highway, Suite 1204, Arlington, VA 22202-4302, and to the Office of Management and Budget, Paperwork Reduction Project (0704-0188), Washington, DC 20503.</small>				
1. AGENCY USE ONLY (Leave blank)	2. REPORT DATE December 1990	3. REPORT TYPE AND DATES COVERED		
4. TITLE AND SUBTITLE DETECTION OF HIGH ALTITUDE AIRCRAFT WAKE VORTICES USING INFRARED DOPPLER LIDAR: AN ASSESSMENT		5. FUNDING NUMBERS		
6. AUTHOR(S) Michael J. Estes, Capt, USAF				
7. PERFORMING ORGANIZATION NAME(S) AND ADDRESS(ES) Air Force Institute of Technology, WPAFB OH 45433-6583		8. PERFORMING ORGANIZATION REPORT NUMBER AFIT/GEO/ENP/90D-1		
9. SPONSORING / MONITORING AGENCY NAME(S) AND ADDRESS(ES)		10. SPONSORING / MONITORING AGENCY REPORT NUMBER		
11. SUPPLEMENTARY NOTES				
12a. DISTRIBUTION AVAILABILITY STATEMENT Approved for public release; distribution unlimited		12b. DISTRIBUTION CODE		
13. ABSTRACT (Maximum 200 words) This thesis investigated the feasibility of air-to-air detection of high altitude aircraft wake vortices at long ranges using infrared Doppler lidar. The purpose of this technique is to detect otherwise stealthy aircraft. Three laser wavelengths were analyzed: 1.064, 2.091, and 9.115 microns. Analysis revealed that the spectral width of the return signal from an aircraft wake presented a good signature for detection. Based on this analysis, a minimum signal-to-noise ratio of 0 dB was established. Detection performance was then analyzed using signal-to-noise ratio calculations for backscatter by ambient atmospheric aerosols, jet engine exhaust soot particles, and condensation trail ice particles. Results indicated that atmospheric aerosols alone were not sufficient for detection in clean atmospheric regions. Backscatter enhancement by soot particles did, however, appear to be sufficient for detection out to 80 km. Enhancement by condensed ice particles in wake contrails provided detection well beyond 100 km in range. Interestingly, the shorter wavelength lidars did not perform as well as the 9.115 micron lidar due to degradations from shot noise, wavefront mismatch, refractive turbulence, and atmospheric extinction.				
14. SUBJECT TERMS Optical Radar, Doppler Systems, Aircraft Detection, Trailing Vortices, Laser Radar, Atmospheric Scattering, Jet Engine Exhaust, Condensation Trails			15. NUMBER OF PAGES 149	
			16. PRICE CODE	
17. SECURITY CLASSIFICATION OF REPORT Unclassified	18. SECURITY CLASSIFICATION OF THIS PAGE Unclassified	19. SECURITY CLASSIFICATION OF ABSTRACT Unclassified	20. LIMITATION OF ABSTRACT UL	

DETECTION OF HIGH ALTITUDE AIRCRAFT WAKE VORTICES
USING INFRARED DOPPLER LIDAR: AN ASSESSMENT

THESIS

Presented to the Faculty of the School of Engineering
of the Air Force Institute of Technology
In Partial Fulfillment of the
Requirements for the Degree of
Master of Science in Electrical Engineering

Michael J. Estes, B.S.
Captain, USAF

December 1990

Accession For	
NTIS	CRPAI
DTIC	LAB
Unannounced	
Justification	
By	
Distribution /	
Availability	
DM	Aviation Spec. Cat.
A-1	

Approved for public release; distribution unlimited



Preface

The purpose of this study was to assess the feasibility of detecting turbulent aircraft wakes using Doppler lidar. Hardware issues aside, the ultimate detectability of an aircraft wake is determined by the level of backscatter within the wake. Therefore, I explored the effects of three different scattering sources on wake detectability. The three scattering sources I analyzed were ambient atmospheric aerosols, jet engine exhaust soot particles, and condensation trail (contrail) particles. While I made every effort to be as complete as possible in the limited amount of time I had, by no means is this analysis the last word. In particular, I found that enhancement of the backscattered signal by the presence of exhaust soot is the pivotal issue on whether this technique will work. Unfortunately, my results on soot enhancement are only a rough, first-cut estimate. A good deal more research is required. I issue this statement both as a warning to the reader and as a suggestion to interested researchers.

Of course, I have many people to thank for their help on this project, not the least of which are my thesis committee members. First of all, I express my utmost gratitude to Maj (ret.) James Lange, my thesis advisor, for taking me on and for taking time out of his retirement to assist me. In addition, I extend great thanks to Dr Won Roh for his time. Despite the fact that he was at first unfamiliar with coherent lidar, his insightful questions and suggestions forced me to think out some of the more complex issues involved. I am also grateful to Dr Ted Luke for taking time out of his very full schedule to be on my thesis committee.

Many more people, from a variety of organizations, contributed their time. Of these, I especially wish to thank Lt Col George Koenig (AFGL/OPA) and Dr Eric Shettle (Naval Research Lab) for their helpful

comments and for copies of BACKSCAT, LOWTRAN, and the MIE scattering programs. Their help was instrumental in the completion of this thesis. I also extend thanks to Mr Ron Rodney (WRDC Staff Met) for running the FASCODE calculations. Others whose contributions are appreciated are Mr Steve Alejandro (AFGL/OPA), Dr Joe Wander (HQ/AFESC), Ms Patrice Ackerman (Boeing), and Dr Arnold Barnes (AFGL/LY).

Last, but far from least, I could not have completed this thesis without the understanding and support of my family. Thankyou, Barb! I know you have sacrificed for me. And, Kayla, I promise I will have more time to read books to you now that AFIT is almost over.

Michael J. Estes

Table of Contents

	Page
Preface	11
List of Figures	vi
List of Tables	xi
Abstract	x
1. Problem Background	1-1
2. Theory	2-1
2.1. Aircraft Wake Vortex Structure	2-1
2.2. Atmospheric Optics	2-9
2.2.1. Preliminary Definitions	2-9
2.2.2. Scattering by Atmospheric Gas Molecules	2-13
2.2.3. Absorption by Atmospheric Gases	2-19
2.2.4. Scattering and Absorption by Aerosols	2-20
2.3. Doppler Lidar	2-24
2.3.1. General Description	2-24
2.3.2. Characteristics of the Backscattered Signal	2-27
2.3.3. Signal-to-Noise Ratio	2-35
2.3.4. Velocity Estimation	2-38
3. Preliminary Considerations	3-1
3.1. Lidar System Parameters	3-1
3.2. Aircraft Examples	3-3
3.3. Geometry	3-5
3.4. Signal Processing	3-8
3.5. Molecular Absorption Effects	3-18
4. Atmospheric Aerosols	4-1
4.1. Vertical Aerosol Structure	4-1
4.1.1. Boundary Layer	4-1
4.1.2. Free Troposphere	4-2
4.1.3. Stratosphere	4-2
4.2. Backscatter and Extinction	4-3
4.2.1. Geophysics Laboratory Aerosol Models	4-4
4.2.2. Model Atmospheres for Calculations	4-5
4.2.3. Comparison with Measured Aerosol Data	4-15
4.3. Performance Analysis	4-17
4.3.1. Signal-to-Noise Ratio Computations	4-17
4.3.2. Analysis of Results	4-18
5. Exhaust Trails	5-1
5.1. Soot Emissions	5-1
5.1.1. Formation	5-1
5.1.2. Mie Scattering Calculations	5-3
5.1.3. Performance Analysis	5-11
5.2. Contrails	5-15
5.2.1. Formation	5-15
5.2.2. Backscatter Estimation	5-18

5.2.3. Performance Analysis	5-22
6. Conclusions	6-1
6.1. Summary of Results	6-1
6.2. Recommendations	6-2
Bibliography	BIB-1
Appendix	A-1
Vita	VITA-1

List of Figures

Figure	Page
2-1. Wake Vortex Formation	2-2
2-2. Wake Development Stages	2-3
2-3. Vortex Tangential Velocity Profile	2-6
2-4. Cross Sectional Flow in a Stable Wake	2-8
2-5.a. U.S. Standard Atmosphere Temperature Profile	2-14
2-5.b. U.S. Standard Atmosphere Pressure Profile	2-15
2-5.c. U.S. Standard Atmosphere Density Profile	2-16
2-6. General Layout of a Monostatic Heterodyne Lidar	2-25
2-7. Molecular Velocity Altitude Profile	2-31
2-8. Typical Power Spectrum of Molecular and Aerosol Returns	2-32
2-9. Transverse Coherence Length Versus Range	2-34
3-1. Tangential Velocity Profiles of Four Aircraft	3-4
3-2. Simplified Wake Detection Geometry	3-7
3-3. Simulated Wake Return Spectra	3-9
3-4. Velocity Width of Return Signals from Four Aircraft	3-10
3-5.a. Velocity Width of Return Signal from Large Transport	3-12
3-5.b. Velocity Width of Return Signal from Medium Transport	3-13
3-5.c. Velocity Width of Return Signal from Large Fighter	3-14
3-5.d. Velocity Width of Return Signal from Small Fighter	3-15
3-6.a. Velocity Width Estimation Error - Short Pulse	3-16
3-6.b. Velocity Width Estimation Error - Long Pulse	3-17
4-1.a. Molecular Backscatter Coefficient Profile	4-6
4-1.b. Molecular Scattering Coefficient Profile	4-7
4-2.a. Aerosol Backscatter Coefficient Profile - Clean Atmosphere	4-8
4-2.b. Aerosol Extinction Coefficient Profile - Clean Atmosphere	4-9

4-3.a. Aerosol Backscatter Coefficient Profile - Moderate Atmosphere	4-10
4-3.b. Aerosol Extinction Coefficient Profile - Moderate Atmosphere	4-11
4-4.a. Aerosol Backscatter Coefficient Profile - Dirty Atmosphere	4-13
4-4.b. Aerosol Extinction Coefficient Profile - Dirty Atmosphere	4-14
4-5. SAGE I 1 μm Aerosol Extinction Coefficient Profiles	4-16
4-6.a. SNR for Clean Atmosphere, 9 km Altitude, 1.064 μm	4-19
4-6.b. SNR for Clean Atmosphere, 9 km Altitude, 2.091 μm	4-20
4-6.c. SNR for Clean Atmosphere, 9 km Altitude, 9.115 μm	4-21
4-7.a. SNR for Clean Atmosphere, 13.7 km Altitude, 1.064 μm	4-22
4-7.b. SNR for Clean Atmosphere, 13.7 km Altitude, 2.091 μm	4-23
4-7.c. SNR for Clean Atmosphere, 13.7 km Altitude, 9.115 μm	4-24
4-8.a. SNR for Moderate Atmosphere, 9 km Altitude, 1.064 μm	4-25
4-8.b. SNR for Moderate Atmosphere, 9 km Altitude, 2.091 μm	4-26
4-8.c. SNR for Moderate Atmosphere, 9 km Altitude, 9.115 μm	4-27
4-9.a. SNR for Moderate Atmosphere, 13.7 km Altitude, 1.064 μm	4-28
4-9.b. SNR for Moderate Atmosphere, 13.7 km Altitude, 2.091 μm	4-29
4-9.c. SNR for Moderate Atmosphere, 13.7 km Altitude, 9.115 μm	4-30
4-10.a. SNR for Dirty Atmosphere, 9 km Altitude, 1.064 μm	4-31
4-10.b. SNR for Dirty Atmosphere, 9 km Altitude, 2.091 μm	4-32
4-10.c. SNR for Dirty Atmosphere, 9 km Altitude, 9.115 μm	4-33
4-11.a. SNR for Dirty Atmosphere, 13.7 km Altitude, 1.064 μm	4-34
4-11.b. SNR for Dirty Atmosphere, 13.7 km Altitude, 2.091 μm	4-35

4-11.c. SNR for Dirty Atmosphere, 13.7 km Altitude, 9.115 μm	4-36
5-1.a. Exhaust Backscatter Coefficients - 1.064 μm	5-6
5-1.b. Exhaust Backscatter Coefficients - 2.091 μm	5-7
5-1.c. Exhaust Backscatter Coefficients - 9.115 μm	5-8
5-2.a. SNR from Soot Enhanced Wakes - 1.064 μm	5-12
5-2.b. SNR from Soot Enhanced Wakes - 2.091 μm	5-13
5-2.c. SNR from Soot Enhanced Wakes - 9.115 μm	5-14
5-3. Jet Aircraft Contrail Formation Conditions	5-17
5-4. SNR from Contrail Enhanced Wakes	5-23

List of Tables

Table	Page
3-1. Base Lidar System Parameters	3-2
3-2. Test Aircraft Dimensions and Cruise Parameters	3-3
3-3. Test Aircraft Wake Parameters	3-5
3-4. Atmospheric Transmission due to Molecular Absorption	3-19
5-1. Published Soot Particle Size Distributions	5-2
5-2. Jet Engine Exhaust Data Sets	5-4
5-3. Refractive Index of Soot	5-5
5-4. Ratio of Maximum Thrust to Recirculation Cell Area	5-9
5-5. Mean Exhaust Backscatter Coefficients in Four Aircraft Wakes	5-9
5-6. Modeled Soot Backscatter Coefficients	5-10
5-7. Refractive Index of Ice	5-19
5-8. Comparison of Calculated Ice Crystal Scattering Coefficients	5-19
5-9. Backscatter Coefficients for Cirrus Cloud Models	5-19
5-10. Measured Cirrus Cloud Backscatter Coefficients	5-20
5-11. Estimated Contrail Backscatter Coefficients	5-21
A-1. Soot Size Distributions for TF30-P1 Engine Data	A-1
A-2. Soot Size Distributions for J52-P3 Engine Data	A-1
A-3. Soot Size Distributions for TF30-P103 Engine Data	A-2
A-4. Soot Size Distributions for TF30-P109 Engine Data	A-2
A-5. Soot Size Distributions for TF41-A2 Engine Data	A-3
A-6. Ice Crystal Size Distributions for Four Cirrus Cloud Models	A-3

Abstract

This thesis investigated the feasibility of detecting the highly turbulent air within high altitude aircraft wake vortices using infrared Doppler lidar mounted in a search aircraft. This technique was looked at for its ability to detect otherwise stealthy military aircraft. Three laser wavelengths were analyzed: 1.064 μm , 2.091 μm , and 9.115 μm . Analysis revealed that the spectral width of the return signal from an aircraft wake presented a good signature for detection. Based on this analysis, a minimum signal-to-noise ratio of 0 dB was established. Detection performance was then analyzed using signal-to-noise ratio calculations for backscatter by ambient atmospheric aerosols, jet engine exhaust soot particles, and contrail ice particles. Results indicated that atmospheric aerosols alone were not sufficient to provide enough backscattered signal for detection in clean regions of the atmosphere. Backscatter enhancement by exhaust soot particles did, however, appear to be sufficient for detection out to 80 km range. Enhancement by condensed ice particles in wake contrails provided the highest signal levels and detection well beyond 100 km in range. Interestingly, the shorter wavelength lidars did not perform nearly as well as the 9.115 μm lidar, due to degradations from shot noise, wavefront mismatch, and refractive turbulence.

DETECTION OF HIGH ALTITUDE AIRCRAFT WAKE VORTICES
USING INFRARED DOPPLER LIDAR: AN ASSESSMENT

1. Problem Background

Now, more than ever before, our fighter aircraft pilots must be keenly aware of the presence of approaching enemy aircraft. To this end, long range detection and classification of possibly hostile aircraft is desired; however, recent advances in stealth technology have made aircraft much more difficult to detect by conventional means, namely radar and passive infrared sensors. At the same time, we also desire that our fighter aircraft become more stealthy. That means avoiding the use of radar, which immediately flags the presence and location of the transmitting aircraft. In order to maintain control of the skies in future conflicts, we need to explore new detection schemes that satisfy both of these requirements.

One possible new detection scheme that shows promise is the detection of aircraft wake vortices using Doppler lidar. As a by-product of lift, every aircraft in flight leaves behind a turbulent wake of air consisting of two counter-rotating vortices. These vortices may persist for a considerable distance behind the aircraft before breaking up and dissipating. As an example, a Boeing 707 aircraft in high altitude cruise leaves behind wake vortices that persist for about 20 kilometers behind the aircraft (Lutchen, 1984:13). By measuring the highly turbulent air currents in the wake, it may be possible to detect the presence of an approaching aircraft and possibly even identify it. Doppler lidar is a remote sensing instrument that appears capable of detecting such turbulent airflow.

A lidar is a remote sensing instrument used to probe the atmosphere. Lidar is an acronym that stands for *L*ight *D*etection And *R*anging. It operates much the same way as conventional radar, except that instead of transmitting pulses of radio waves a lidar uses a laser to transmit pulses of light waves. The transmitted laser pulse scatters off of small particles (i.e. - dust particles, water droplets, molecules, etc.) suspended in the atmosphere and a small fraction of this scattered light is collected by the lidar receiver. Doppler lidar is a specialized type of lidar that senses the Doppler frequency shift in the backscattered light caused by the relative motion of the scattering particles towards or away from the lidar. In this way, a Doppler lidar can measure the radial air flow along the beam path and thus seems to be ideally suited for detecting aircraft wake vortices.

It should be mentioned here that lidar may also be used to detect trace gas species in the exhaust trail of the aircraft. This detection scheme does not use the Doppler shift phenomenon to measure air flow, but rather it uses spectroscopic lidar techniques such as DIAL (Differential Absorption Lidar), Raman scattering, or resonance fluorescence to identify specific gases peculiar to aircraft exhaust. Spectroscopic techniques will not be addressed in this thesis; however, the reader should be aware of their existence and possible usefulness for aircraft detection. For more information on spectroscopic lidar techniques, see Measures (1984) and Hinkley (1976).

The concept of Doppler lidar detection of aircraft vortices has been around almost as long as the laser itself. Possibly the first study was made in the late 1960's and employed a continuous wave CO₂ laser-Doppler velocimeter to detect the spinning vortices of a low flying C-47 aircraft (Huffaker et al., 1970). This experimental effort seemed to prove the viability of the concept. Since that time, several more studies have been conducted, some of which were concerned with low

altitude vortex detection around airports for the purpose of aircraft safety. While related, this research does not address long range detection and thus is not of great interest for this thesis. Two studies, however, were located that considered long range detection of aircraft vortices (Thomson et al., 1989; Lutchen, 1984). One problem evident in these studies is that maximum detection range is extremely sensitive to the amount and type of atmospheric aerosol and exhaust particulate present both in the aircraft wake itself as well as along the laser beam path. The purpose of this thesis, therefore, is to explore how maximum detection range varies with atmospheric conditions and aircraft exhaust products.

Three infrared laser wavelengths will be considered in this analysis: Nd:YAG at 1.06 μm , Ho:YAG at 2.09 μm , and isotopic CO_2 at 9.11 μm . Each of these laser systems has its own relative merits. The Nd:YAG and Ho:YAG lasers, for example, are both solid state lasers and are thus smaller, simpler, and more reliable than CO_2 gas lasers; however, CO_2 laser technology is much more mature. In addition, the Nd:YAG laser is not nearly as eyesafe as the longer wavelength lasers. These relative advantages and disadvantages will not be addressed in this thesis. The only criteria to be compared between the three lasers will be detection performance as a function of wavelength.

Maximum detection range will be analyzed for backscatter due to naturally occurring atmospheric aerosols and for jet engine exhaust aerosols. Each of these aerosol types will be analyzed separately. Atmospheric aerosols are considered here to be non-cloud particulates such as dust, haze, and volcanic debris that are present in the atmosphere and vary with altitude, season, geographic location, and weather. The type and amount of atmospheric aerosol affects both extinction of light along the beam path as well as the amount of light backscattered to the lidar receiver. Exhaust aerosols, on the other hand, are consid-

ered to be by-products of combustion and thus do not occur naturally. Particles in the exhaust trails of aircraft may provide enhancement in the backscattered signal. Exhaust aerosols to be analyzed include both soot from combustion and ice particles formed in condensation trails (contrails). The magnitude and variation in all these effects, which are strongly a function of wavelength, will be analyzed.

Specific signal processing algorithms and wake physics will not be covered in this thesis. While overall detection performance obviously depends on the processing algorithm used, the ultimate detectability is limited more by physical constraints such as backscatter and attenuation of the lidar beam as well as the sensitivity of the lidar itself. The analysis of detection algorithms will be left for future research. In addition, wake vortex physics is a complex subject and will only be synopsized here. Only simple models of wake vortex behavior will be required for this analysis.

The scenario of interest is a tactical air-to-air environment. Therefore, the most probable geometry is for the search aircraft (the one with the lidar) to be at normal cruise altitude of from 20,000 to 50,000 feet with the lidar looking nearly horizontally, scanning for aircraft wakes at these altitudes. Ground-to-air detection and air-to-air detection of low flying aircraft will not be considered here. A study by Thomson et al. (1989) analyzes air-to-air detection of aircraft in the boundary layer and lower troposphere.

This thesis is organized into six chapters. The first is the current background chapter. The second chapter covers theory, including the definitions and equations to be used in succeeding analyses. The third chapter covers preliminary considerations that set the conditions and assumptions for the analyses. The fourth and fifth chapters present the analysis of atmospheric aerosols and exhaust aerosols, respectively.

Each aerosol type is treated independently. Finally, the sixth chapter summarizes the results and discusses recommendations for further research.

2. Theory

This chapter presents the background theory to be used in subsequent analyses. It is assumed that the reader has a general background in optics and engineering, but is perhaps not familiar with the specific concepts and definitions of aircraft wake vortices, atmospheric optics, or Doppler lidar. The first subsection in this chapter deals with the general structure of aircraft wake vortices. The second subsection presents a quick overview of applicable atmospheric optics effects such as scattering and absorption. Finally, the third subsection describes how Doppler lidar works and develops equations for signal-to-noise ratio and velocity estimation error. These equations will be used to quantify detection performance and thus maximum detection range for the three conditions to be analyzed.

2.1. Aircraft Wake Vortex Structure

Every fixed wing aircraft in flight generates a set of two wake vortices that spin off of the wing tips and form in parallel behind the aircraft. Since the vortices are a by-product of lift by the wing, they are difficult to eliminate. This feature makes wake vortices good targets for detection of otherwise stealthy aircraft. The general structure of aircraft wake vortices is described below along with some simple mathematical models of airflow in the vortices.

As an aircraft moves through the air, high pressure below the wing and low pressure above the wing generate lift. In addition, this pressure gradient also produces air circulation about the wing, which eventually sheds off the trailing edge of the wing and forms into two parallel vortices. This process illustrated in Figure 2-1. Wake development may be subdivided into three stages: 1) rollup or formation, 2) equilibrium, and 3) breakup and dissipation. Figure 2-2 shows the three wake stages, which are discussed further below.

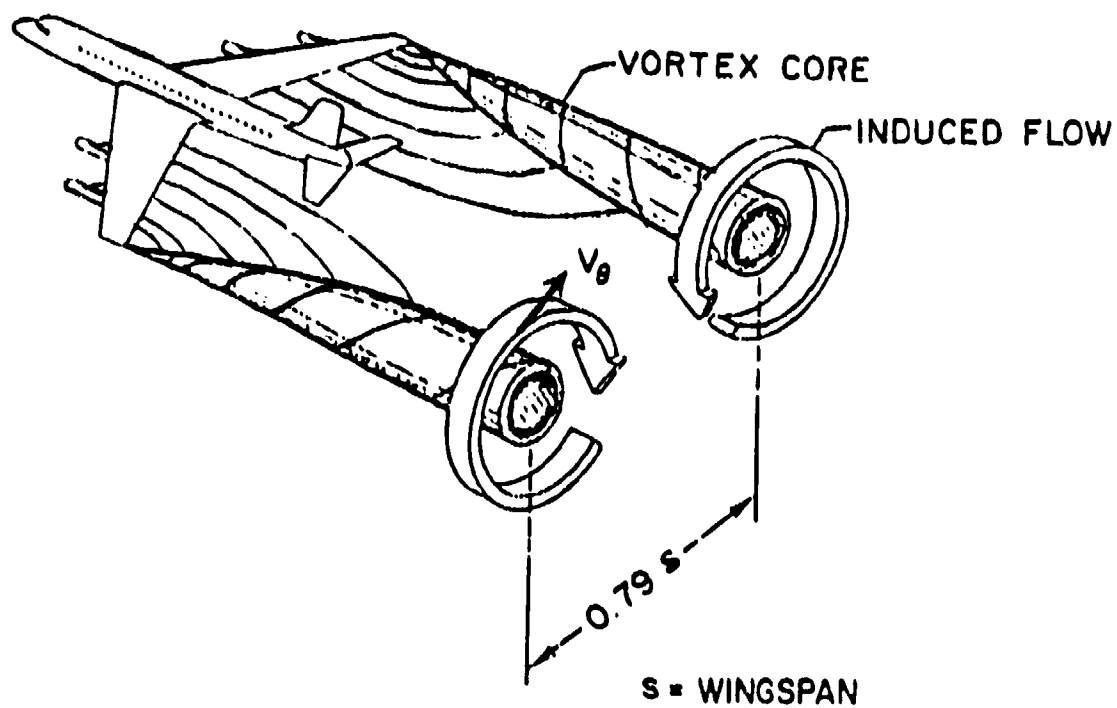


Figure 2-1. Wake Vortex Formation Behind a Lifting Wing (Lutchen, 1984:6)

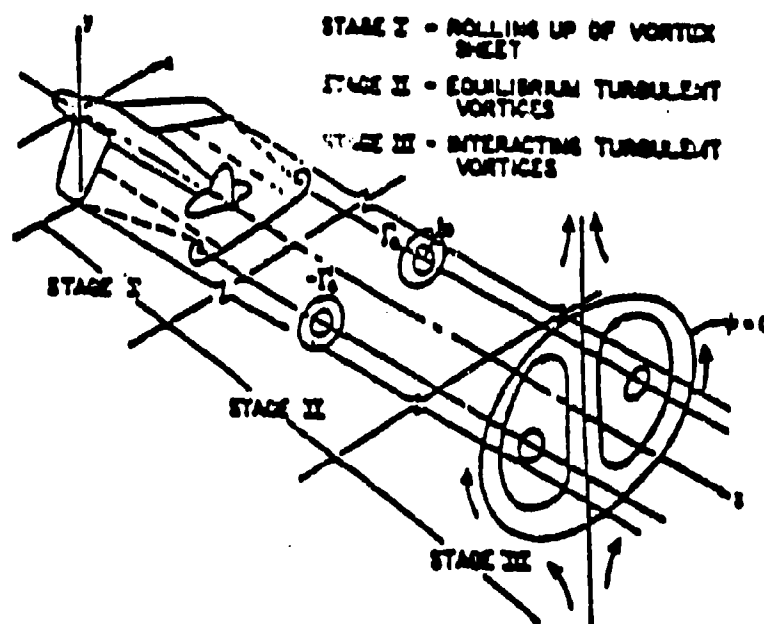


Figure 2-2. Wake Development Stages (Thomson et al., 1989:3-2 as taken from Neilson and Schwind, 1971)

The first stage of wake development is the wake roll up stage during which the trailing vortices start to form. As seen in Figure 2-1, the circulating "vortex sheet" rolls up behind the aircraft forming two counter-rotating columns of air parallel to the line of flight. Roll up is usually complete within 5 to 10 wingspans behind the aircraft and thus is not of much interest for wake detection (Thomson et al., 1989:3-1). The total circulation of each vortex is given by

$$\Gamma = \frac{Mg}{\rho K s V_0} \quad (2-1)$$

where

- Γ = circulation parameter (m^2/s)
- M = aircraft mass (kg)
- g = acceleration of gravity (m/s^2)
- ρ = air density (kg/m^3)
- s = aircraft wingspan (m)
- K = wing loading constant
 - = $\pi/4$ for an elliptically loaded wing
- V_0 = aircraft velocity (m/s)

The separation distance between vortex centers, b , is proportional to wingspan by the wing loading constant, or

$$b = K s \quad (2-2)$$

Once the wake has rolled up, it stabilizes into a relatively time invariant flow structure. This stable flow field is the second, or equilibrium, stage of wake development. The length of the equilibrium wake, which may be anywhere from 100 to 1000 wingspans, may be expressed as (Thomson et al., 1989:3-9)

$$L_1 = \frac{2\pi \xi_1 \rho V_0^2 b^3}{Mg} \quad (2-3)$$

where

L_v = equilibrium wake length (m)

ζ_v = dimensionless wake length

The parameter ζ_v indicates how long the wake remains stable before ambient shear and turbulence in the atmosphere start to break it apart. A model of the dependence of ζ_v on atmospheric conditions may be found in Crow and Bate (1976). For this analysis, we will use a value of $\zeta_v=3$ (Thomson et al., 1989:3-10).

Several models exist of the tangential velocity at a distance r from the vortex center. A model by Betz (1932, 1933) fits experimental data well, but has a discontinuity at the vortex center where velocity goes to infinity. Spreiter and Sacks (1951) proposed a model to eliminate this discontinuity. The Spreiter-Sacks model is given by (Thomson et al., 1989:3-13)

$$V_\theta(r) = \begin{cases} \frac{\Gamma r}{2\pi r_c^2}, & r \leq r_c \\ \frac{\Gamma}{2\pi r}, & r > r_c \end{cases} \quad (2-4)$$

where

$V_\theta(r)$ = tangential velocity component (m/s)

Γ = circulation of vortex (m^2/s)

r = distance from vortex center (m)

r_c = vortex core radius (m)

A plot of $V_\theta(r)$ is shown in Figure 2-3. The peak tangential velocity occurs at the edge of the center region of each vortex, known as the vortex core. The core radius is given by

$$r_c = \frac{1}{2}\epsilon_v b \quad (2-5)$$

where $\epsilon_v=0.197$ (Spreiter and Sacks, 1951).

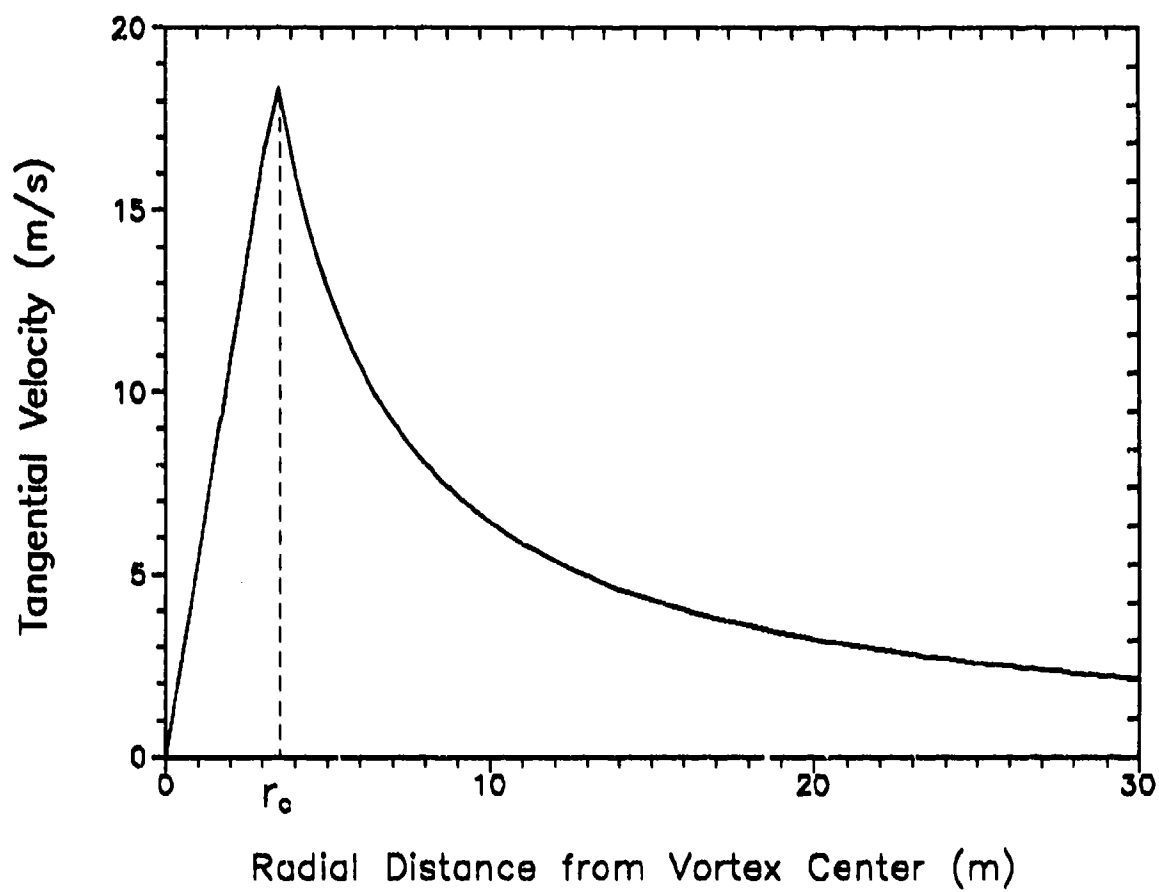


Figure 2-3. Wake Vortex Tangential Velocity Profile for a Boeing 707 Aircraft Travelling at 237 m/s at 10.7 km Altitude (Lutchen, 1984:9)

The flow vector at any point within the equilibrium wake is found by the vector addition of the flow vectors from each of the two vortices. A cross section of the wake with contours of constant velocity is shown in Figure 2-4.

The elliptical region surrounding both vortices (the shaded region in Figure 2-4) is called the recirculation cell. The dimensions of this region are 1.64s in width by 1.35s in height (Lutchen, 1984:8). One of the key features of the equilibrium stage is the fact that the size of this cell remains fairly constant. The recirculation cell is bounded by a streamline across which no mass is transferred, hence the name. The fact that no mass is transferred across this streamline implies that all the exhaust emissions become entrained in the recirculation cell. This point will be important later when we analyze exhaust trails. The flow at the edges of the recirculation cell cause the entire cell to move downward with a vertical sink velocity given by (Lutchen, 1984:8)

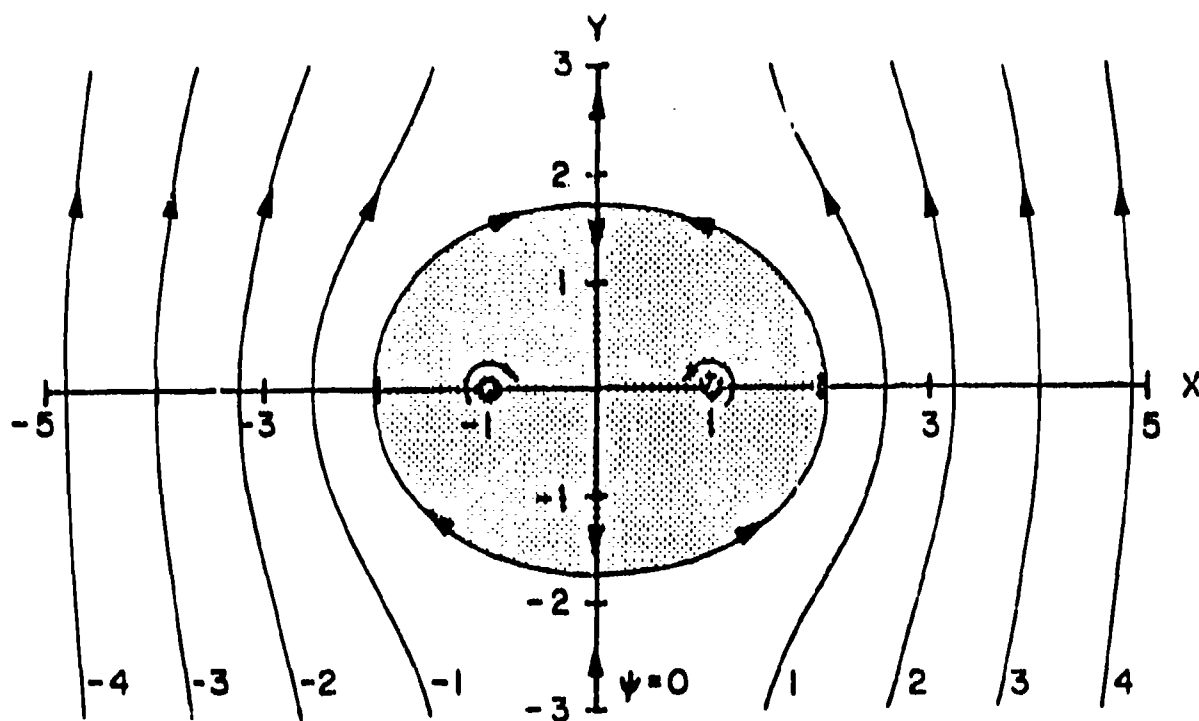
$$V_{sink} = -\frac{2\Gamma}{\pi^2 s} \quad (2-6)$$

In addition to the vertical and tangential velocities of the wake, axial velocities also exist due to thrust and drag. The vortex cores have a forward axial velocity due to drag given by (Thomson et al., 1989:3-13)

$$V_z = \frac{\Gamma}{2\sqrt{2}\pi r_c} \quad (2-7)$$

while the entire recirculation cell has a backward axial velocity due to thrust, which is given by (Thomson et al., 1989:3-13)

$$V_z = \frac{0.021\Gamma_c}{(1.64)(1.35)} \quad (2-8)$$



SHADED REGION IS RECIRCULATION CELL
 ψ = VALUE OF THE STREAM FUNCTION

Figure 2-4. Cross Sectional Flow in a Stable Wake (Lutchen, 1984:12)

where both U , and V , are in units of m/s. Again, the actual vector velocity at any given point within the wake is the vector sum of all tangential, vertical, and axial velocity vectors at that point.

Eventually, interaction between the vortices and turbulent forces in the atmosphere cause the wake to break up and dissipate. This is the third and final wake stage. During this stage, the recirculation cell begins to grow and dissipate in the atmosphere. According to the literature, the transverse dimensions of the wake grow at a time rate proportional to about $t^{1/3}$, where t is time (Thomson et al., 1989:3-16). Due to its unstable nature, we will not be concerned with the third wake stage for this analysis.

2.2. Atmospheric Optics

This subsection gives a quick introduction to optical scattering and absorption by both gases and aerosols in the atmosphere. Since the subject of atmospheric optics is very complex, only the basic concepts are presented here. In addition, we will only consider elastic scattering processes in which the frequency of the scattered light is exactly the same as the frequency of the incident light. Wherever possible, existing models of these atmospheric processes are described as they will be used extensively in the analysis sections.

2.2.1. Preliminary Definitions

Consider a monochromatic light wave incident on a small particle. A portion of the incident light will be scattered off in all directions (not necessarily equally), a portion of the light energy will be absorbed by the particle, and a portion of the light will travel on unaffected. The scattering cross section of the particle is defined as the ratio of the total scattered power to the incident irradiance (Fenn et al., 1985:18-15):

$$\sigma_s = \frac{P_s}{E_0} = \frac{1}{E_0} \int_0^{4\pi} I_s(\theta) d\Omega \quad (2-9)$$

where

σ_s = scattering cross section (m^2)

P_s = total scattered power (W)

E_0 = incident irradiance (W/m^2)

$I_s(\theta)$ = scattered intensity at angle θ (W/sr)

Note the use of radiometric symbols E for irradiance and I for intensity. Similarly, for absorption, the absorption cross section of the particle may be defined as the ratio of the total absorbed power to the incident irradiance:

$$\sigma_a = \frac{P_a}{E_0} \quad (2-10)$$

where

σ_a = absorption cross section (m^2)

P_a = total power absorbed (W)

It is important to note that both σ_s and σ_a are generally strong functions of wavelength, as are all the parameters that will be defined in this subsection. The primary consideration, at least for scattering, is the size of the particle relative to the wavelength of light. This wavelength dependence will become more clear in the following sections on molecular scattering and aerosol scattering.

Now consider the case where many particles, all separated with random spacing, are illuminated by the light. Assuming low particle density and single scattering, we can define two new parameters called the scattering and absorption coefficients that define how much of the incident light is scattered or absorbed per unit path length by this group of particles (Fenn et al., 1985:18-15):

$$\beta_s = N\sigma_s \quad (2-11)$$

$$\beta_a = N\sigma_a \quad (2-12)$$

where

β_s = scattering coefficient (m^{-1})

β_a = absorption coefficient (m^{-1})

N = particle density (m^{-3})

Furthermore, we can define the extinction coefficient of the group of particles as the total power both scattered and absorbed per unit length:

$$\beta_e = \beta_s + \beta_a \quad (2-13)$$

Thus, light propagating through a medium of particles with extinction coefficient β , undergoes an incremental decrease in irradiance per path length dR of

$$dE = -E\beta_e dR \quad (2-14)$$

Integrating this equation yields the Beer-Lambert law for the irradiance at a distance R from the source

$$E(R) = E(0)\exp(-\beta_e R) \quad (2-15)$$

where

$E(R)$ = irradiance at distance R (W/m^2)

Note that the equation above applies only to a uniform medium where β_e is constant throughout. For a medium, such as the atmosphere, where β_e is non-uniform, the Beer-Lambert law becomes

$$E(R) = E(0)\exp\left(-\int_0^R \beta_e(r) dr\right) \quad (2-16)$$

The transmission over this one-way optical path of distance R is

$$\tau(R) = \frac{E(R)}{E(0)} = \exp\left(-\int_0^R \beta_e(r) dr\right) \quad (2-17)$$

For a single scatterer, the intensity of the scattered light generally depends on the scattering direction. The angular scattering dependency for a particle is summed up in a parameter called the phase function, which defines how much of the scattered power scatters in a

given direction and in a given solid angle. The phase function is normalized such that integral over all solid angles is unity (McCartney, 1976:200):

$$\frac{1}{4\pi} \int_0^{4\pi} P(\theta) d\omega = 1 \quad (2-18)$$

where

$P(\theta)$ = normalized phase function (sr^{-1})

θ = scattering angle (rad)

For a volume of scatterers, the angular scattering coefficient indicates how much light will be scattered in direction θ per steradian. The angular scattering coefficient, $\beta_s(\theta)$, is the normalized phase function per particle times the scattering coefficient for the ensemble of particles. In symbols,

$$\beta_s(\theta) = \frac{\beta_s}{4\pi} P(\theta) \quad (2-19)$$

which has units of $\text{m}^{-1}\text{sr}^{-1}$. Note that the previously defined quantity β_s is really the total scattering coefficient, as it is the sum of the angular scattering coefficient over all solid angles

$$\beta_s = \int_0^{4\pi} \beta_s(\theta) d\omega \quad (2-20)$$

For lidar applications we are interested primarily in the angular scattering back towards the light source at $\theta = \pi$. The angular scattering coefficient at this angle is also known as the volume backscatter coefficient, $\beta_s(\pi)$ and is given as

$$\beta_s(\pi) = \frac{P(\pi)}{4\pi} \beta_s \quad (2-21)$$

Now let us see how these scattering parameters may be used in actual calculations. For a single scatterer, the scattered intensity at a given angle may be expressed in terms of the incident irradiance as

$$I_s(\theta) = \frac{P(0)}{4\pi} \sigma_s E_0 \quad (2-22)$$

where

E_0 = incident irradiance (W/m²)

$I_s(\theta)$ = scattered intensity (W/sr)

For a volume of identical scatterers with N particles per unit volume, the scattered intensity is given by

$$\begin{aligned} I_s(\theta) &= \beta_s(\theta) E_0 V' \\ &= \beta_s(\theta) P_0 L \end{aligned} \quad (2-23)$$

where

V' = volume of scatterers illuminated (m³)

L = longitudinal length of scattering volume (m)

P_0 = total power of incident light (W)

Take note of the fact that the scattered light is linear in terms of power. That is, the scattered power or intensity is a linear function of the number of particles. This observation implies that the scattered light *incoherently* adds, even though we have made no mention of the coherence properties of the incident radiation. Indeed this is the case for both coherent and incoherent illumination if we assume that the number of scatterers is large and that they are randomly spaced. Since the scattered waves from all particles interfere constructively just as much as destructively due to the random spacing, the interference terms average out and the total scattered power is then just the sum of the power scattered from each individual particle.

2.2.2. Scattering by Atmospheric Gas Molecules

The lower 80 kilometers of the earth's atmosphere is composed of a uniform mixture of gases consisting of 79% N₂, 21% O₂, and much smaller quantities of CO₂, CH₄, N₂O, and CO (Fenn et al., 1985:18-2). Figures 2-5.a-c show how temperature, pressure, and density vary with altitude.

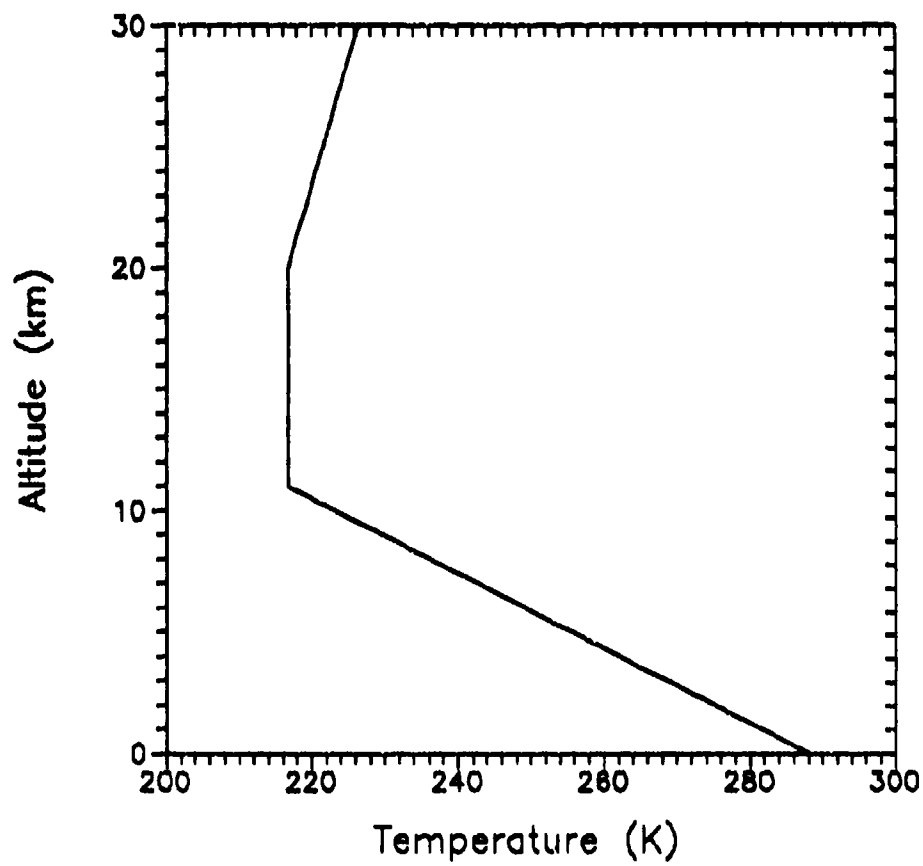


Figure 2 5.a. Atmospheric Temperature versus Altitude (from the U.S. Standard Atmosphere, 1976)

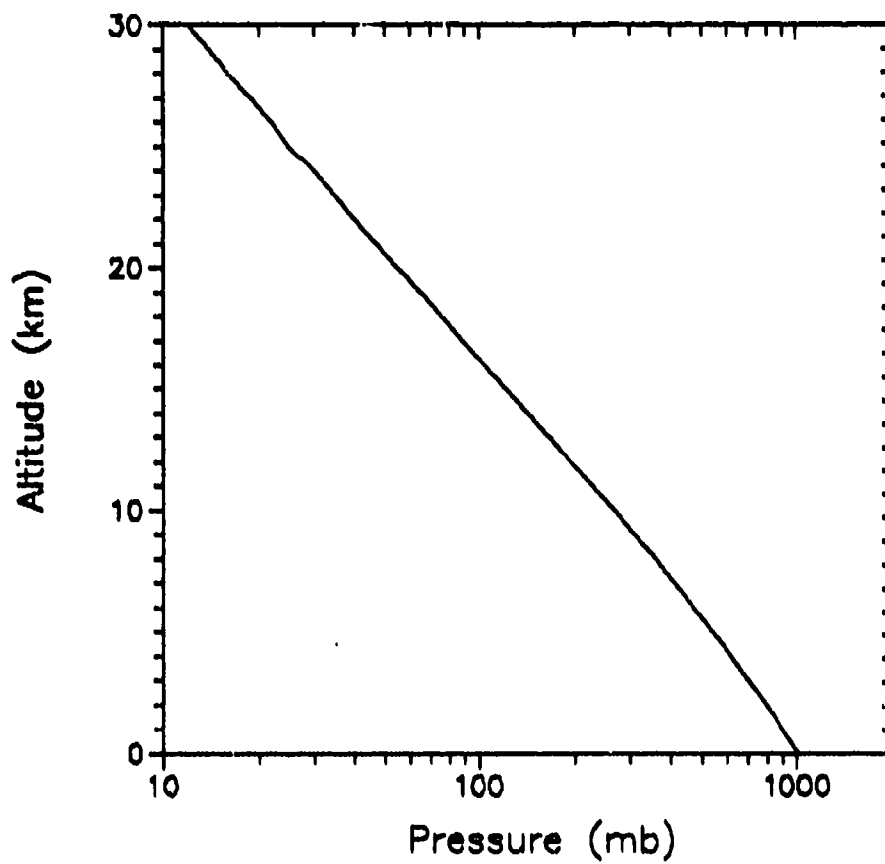


Figure 2-5.b. Atmospheric Pressure versus Altitude (from the U.S. Standard Atmosphere, 1976)

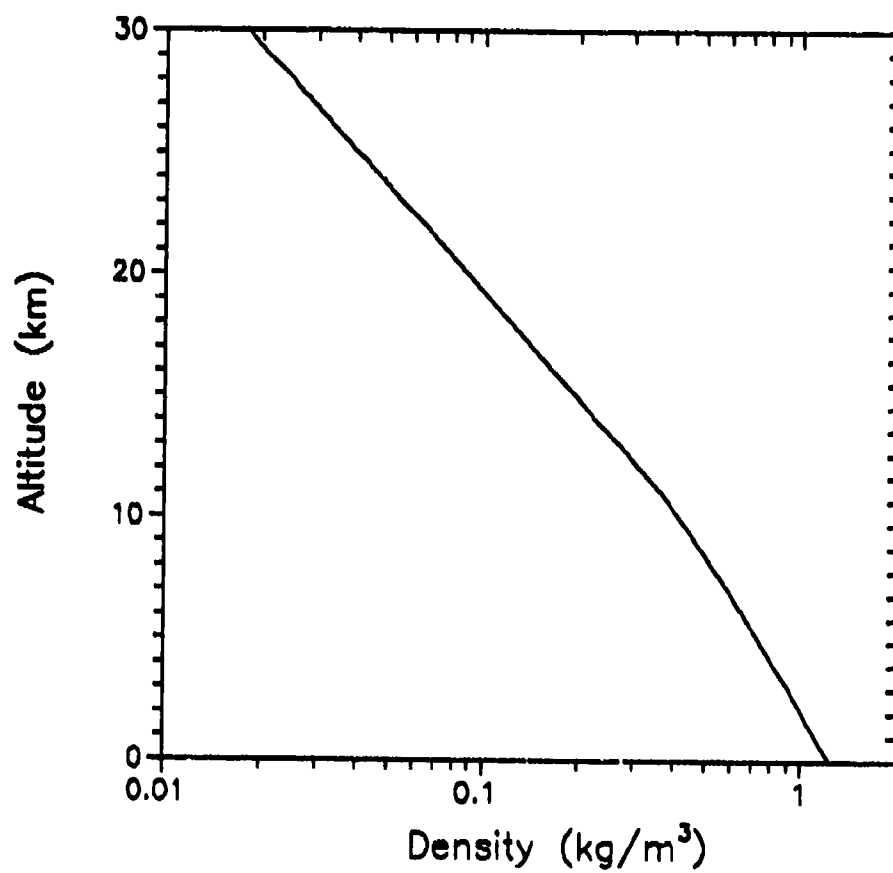


Figure 2-5.c. Atmospheric Density versus Altitude (from the U.S. Standard Atmosphere, 1976)

The data shown in these figures is from the U.S. Standard Atmosphere (1976) model. The scattering of light by atmospheric gases is a function of the index of refraction of air. For wavelengths from 0.23 μm through the infrared, the index of refraction is given by (Edlen, 1966)

$$n = 1 + 10^{-6} \left\{ \left[a_0 + \frac{a_1}{1 - (\nu/b_1)^2} + \frac{a_2}{1 - (\nu/b_2)^2} \right] \frac{P(T_0 + 15.0)}{P_0 T} - [c_0 - (\nu/c_1)^2] \frac{P_w}{P_0} \right\} \quad (2-24)$$

where

n = index of refraction

P = total air pressure in millibars (mb)

P_0 = 1013.25 mb

P_w = partial pressure of water vapor (mb)

T = temperature (K)

T_0 = 273.15 K

ν = optical wavenumber (cm^{-1})

a_0 = 83.42

a_1 = 185.08

a_2 = 4.11

b_1 = $1.140 \times 10^5 \text{ cm}^{-1}$

b_2 = $6.24 \times 10^4 \text{ cm}^{-1}$

c_0 = 43.49

c_1 = $1.70 \times 10^4 \text{ cm}^{-1}$

The dependence of optical scattering on index of refraction is described by Rayleigh scattering theory, which is discussed below.

Rayleigh scattering theory, developed by Lord Rayleigh in 1871 to explain blue sky light (McCartney, 1976:176), describes the scattering of electromagnetic radiation by particles whose size is much smaller than the wavelength of the incident radiation. Such is the case of light scattered by atmospheric gas molecules. A thorough treatment of Rayleigh scattering in the atmosphere may be found in McCartney (1976)

and to some extent in Fenn et al. (1985:Section 18-1). Here we will only be concerned with the general characteristics of Rayleigh scattering and how to compute the extinction and backscatter coefficients.

The Rayleigh scattering coefficient (total) for a volume of gas molecules is given as (Fenn et al., 1985:18-7)

$$\beta_r = \frac{24\pi^3}{N\lambda^4} \left(\frac{n^2 - 1}{n^2 + 2} \right)^2 \left(\frac{6 + 3\Delta}{6 - 7\Delta} \right) \quad (2-25)$$

where

λ = wavelength of light (m)

N = particle density (m^{-3})

n = refractive index of the gas

Δ = depolarization factor

The depolarization factor accounts for the fact that air molecules are not completely isotropic. The depolarization factor for dry air is given as $\Delta=0.0279$ (Young, 1980).

Note that β_r is a strong function of wavelength. One of the main characteristics of Rayleigh scattering is the λ^{-4} wavelength dependence of the scattered light intensity. Thus, blue light scatters much more efficiently than red light, and hence the blue color of the sky. In addition, we see that the amount of light scattered from gas molecules is 10,000 times higher at a wavelength of 1 μm than at 10 μm . Other unique characteristics of Rayleigh scattering (McCartney, 1976:176) include the fact that the forward- and backscattered intensities are equal, and that the "light scattered at 90 degrees is almost completely polarized".

The angular distribution of scattered light, or phase function, for Rayleigh scattering is given by

$$P(\theta) = \frac{3}{16\pi} \frac{2}{(2 + \Delta)} [(1 + \Delta) + (1 - \Delta)\cos^2\theta] \quad (2-26)$$

With knowledge of the scattering coefficient and phase function we may easily compute the backscatter coefficient as

$$\begin{aligned} \beta_b(\pi) &= \frac{\beta_s}{4\pi} P(\pi) \\ &= \frac{27\pi}{2N\lambda^4} \left(\frac{n^2 - 1}{n^2 + 2} \right)^2 \left(\frac{1}{6 - 7\Delta} \right) \end{aligned} \quad (2-27)$$

These equations thus allow us to calculate the angular scattering of a volume of gas of index of refraction n . Absorption of light by gas molecules is a much more complicated subject, as seen in the next section.

2.2.3. Absorption by Atmospheric Gases

Like molecular scattering, absorption of light by atmospheric gases is also a strong function of wavelength, although in a much more complicated way. Each gas species has its own absorption spectrum consisting of a number of narrow absorption peaks centered about the electronic, vibrational, and rotational energy transitions of the gas molecules. Atmospheric gas absorption is then the combination of all of the gas species present and is a function of the number of molecules of each gas, the wavelength, and the temperature of the air. The physics to model this process in the atmosphere is far beyond the scope of this thesis; however, some rather accurate computer models of atmospheric absorption have been developed, most notably by the Air Force's Geophysics Laboratory. These models are discussed below as they will be used in later analysis sections.

FASCODE is probably the most extensive model of atmospheric absorption and scattering. FASCODE takes into account the absorption and scattering characteristics of both atmospheric gases and aerosols to calculate transmission and radiance along an optical path. FASCODE computations are valid in the spectral region from the microwave to the

near ultraviolet (Clough et al., 1986:1). FASCODE is well suited for modeling the transmission of laser light, which is spectrally very narrow. FASCODE will be used to compute molecular absorption at 1.064, 2.091, and 9.115 μm in the atmosphere.

2.2.4. Scattering and Absorption by Aerosols

Aerosol particles suspended in the atmosphere, such as dust, haze, smoke, and fog, also scatter and absorb light. These particles are much larger than molecules, typically 0.01 to 10 μm in diameter. Scattering by aerosol particles may be reasonably modeled by Mie scattering theory. Mie scattering applies to particles that are close in size to the wavelength of light. Mie scattering theory has been used with good results to model scattering and absorption of many atmospheric aerosols (Fenn et al., 1985:18-9 - 18-35).

Mie scattering theory was developed around the turn of the century by Gustav Mie and others to explain the scattering and absorption of light by *spherical* particles of arbitrary index of refraction. Mie theory is much more inclusive than the Rayleigh theory in that it explains scattering by any size particle by any wavelength of electromagnetic radiation, and it also includes absorption. The literature abounds with in-depth treatments of Mie scattering theory, which is computationally complex (McCartney, 1976; Blattner, 1972; and van de Hulst, 1957). The following is a quick overview of Mie scattering that excludes computational details.

In Mie theory, the absolute values of wavelength and particle radius are unimportant. Only the relative ratio of particle radius to wavelength matters. Thus a convenient parameter called the size parameter is defined as

$$\alpha = kr = \frac{2\pi}{\lambda} r \quad (2-28)$$

where

α = Mie size parameter

$k = 2\pi/\lambda$ (m^{-1})

r = particle radius (m)

Consider light incident upon a single spherical scatterer. The scattered radiation field consists of two electric field components with polarizations parallel and perpendicular to the plane of observation. The angular distribution of the scattered field is proportional to two dimensionless field distribution functions, S_1 and S_2 , which are in turn functions of the size parameter, α , the complex index of refraction of the particle, m , and the scattering angle, θ . These field distribution functions are defined as

$$S_1(\alpha, m, \theta) = \sum_{n=1}^{\infty} \frac{2n+1}{n(n+1)} (\alpha_n \pi_n + b_n \tau_n) \quad (2-29)$$

$$S_2(\alpha, m, \theta) = \sum_{n=1}^{\infty} \frac{2n+1}{n(n+1)} (b_n \pi_n + \alpha_n \tau_n) \quad (2-30)$$

where the functions α_n, b_n are the complex amplitude coefficients computed from Ricatti-Bessel functions and depend on the size parameter and complex index of refraction. The functions π_n, τ_n are computed from Legendre polynomials and are only dependent on the scattering angle (McCartney, 1976:229; Blattner, 1972:2). The field distribution functions are related to two intensity distribution functions (also known as phase functions), which are proportional to the scattered intensity from the particle at a given angle. The intensity distribution functions, denoted by i_1 and i_2 , are proportional to the scattered intensities of the polarization components perpendicular and parallel to the plane of observation and are given by

$$i_1 = S_1 S_1' = |S_1|^2 \quad (2-31)$$

$$i_2 = S_2 S_2' = |S_2|^2 \quad (2-32)$$

The units of i_1 and i_2 are sr^{-1} . At scattering angles $\theta = 0$ and $\theta = \pi$, i_1 and i_2 are equal (McCartney, 1976:264).

The total intensity backscattered at $\theta = \pi$ is proportional to the incident irradiance as

$$\begin{aligned} I_s(\pi) &= E_0 \frac{\lambda^2}{4\pi^2} i_1(\pi) \\ &= E_0 \frac{\lambda^2}{4\pi^2} i_2(\pi) \end{aligned} \quad (2-33)$$

where

E_0 = incident irradiance (W/m^2)

$i_1(\pi)$ = backscattered intensity (W/sr)

It may be seen that the polarization of the backscattered light is the same as the polarization of the incident light.

The total scattering cross section, σ_s , and extinction cross section, σ_e , of the particle are given by (McCartney, 1976:247-248)

$$\sigma_s = \frac{\lambda^2}{2\pi} \sum_{n=1}^{\infty} (2n+1) (|a_n|^2 + |b_n|^2) \quad (2-34)$$

$$\sigma_e = \frac{\lambda^2}{2\pi} \sum_{n=0}^{\infty} (2n+1) \text{Re}\{a_n + b_n\} \quad (2-35)$$

The preceding equations assumed a single scatterer of fixed size. Now consider the more realistic case of a volume of particles of the same index of refraction but different sizes. The scattering and extinction coefficients for the *polydispersion* must be integrated over the size distribution of particles to give (McCartney, 1976:265)

$$\beta_s = \frac{1}{k} \int_{a_1}^{a_2} \sigma_s(\alpha) n(\alpha) d\alpha \quad (2-36)$$

$$\beta_e = \frac{1}{k} \int_{a_1}^{a_2} \sigma_e(\alpha) n(\alpha) d\alpha \quad (2-37)$$

where

$n(\alpha)$ = particle size distribution (m^3)

The absorption coefficient is again defined by

$$\beta_a = \beta_r - \beta_s$$

The scattering phase functions must also be modified to incorporate the integration of scattering from all particle sizes. We may define two new phase functions, $P_1(\theta)$ and $P_2(\theta)$, for the polydispersion of scatters in terms of the phase functions for each individual particle as (McCartney, 1976:265)

$$P_j(\theta) = \frac{4\pi}{k^3\beta_s} \int_{\alpha_1}^{\alpha_2} n(\alpha) i_j(\theta, \alpha) d\alpha \quad (2-38)$$

for $j = 1, 2$

As before, $P_1(0)$ and $P_2(0)$ are proportional to the scattered intensity at an angle θ per unit solid angle for the polarizations perpendicular and parallel to the plane of observation. Since the backscattered polarization is the same as the incident polarization, $P_1(\pi) = P_2(\pi)$, and the backscatter coefficient for the polydispersion of particles is given by

$$\beta_s(\pi) = \frac{\beta_s}{4\pi} \left[\frac{P_1(\pi) + P_2(\pi)}{2} \right] \quad (2-39)$$

As mentioned previously, Mie scattering theory applies to spherical particles. In general, though, atmospheric aerosols are not spherical. Liquid aerosols, such as water droplets, are approximately spherical, but dry aerosols like dust and soot are definitely not. Some researchers feel that this discrepancy is not really a problem since most particle sizing instruments tend to assign an "equivalent" particle radius for a spherical particle with similar scattering properties as the actual particle. The resulting models of atmospheric aerosols derived from these measurements therefore should remain approximately valid (Fenn et al., 1985:18-15). In the specific case of cirrus clouds, however, the spherical approximation gives generally poor results (Shettle, 1990). In addition, depolarization from cirrus clouds may be

substantial. That is, the polarization of the backscattered light may be significantly different from the polarization of the incident light. In this case, the single parameter backscatter coefficient previously defined does not apply and scattering matrices must be used to account for polarization.

2.3. Doppler Lidar

By measuring the Doppler frequency shift in backscattered light, a Doppler lidar may be used to measure the relative motion of air currents. The technique most commonly used for this measurement is heterodyne detection, which is described below.

A complete and thorough treatment of Doppler lidar does not really exist in the open literature since the topic pulls in expertise from a number of diverse fields such as radar, laser physics, atmospheric physics, etc. Menzies and Hardesty (1989), though, do give an excellent overview of Doppler lidar for atmospheric wind measurements and include a number of classic references on the subject.

2.3.1. General Description

Most Doppler lidars use heterodyne detection to obtain the very fine spectral resolution required to measure small Doppler shifts. Such lidars are generally monostatic or coaxial, meaning that the transmitted and received beams use the same optics. Figure 2-6 shows the general layout of a monostatic heterodyne lidar system. A highly coherent pulsed laser generates the output beam, which is expanded by a telescope and transmitted out into the atmosphere. Backscattered light is then collected by the telescope, photomixed with a stable reference beam from a local oscillator laser, and then focused down onto a square-law photodetector. The local oscillator frequency is slightly offset from the transmitter frequency so that the irradiance on the detector is

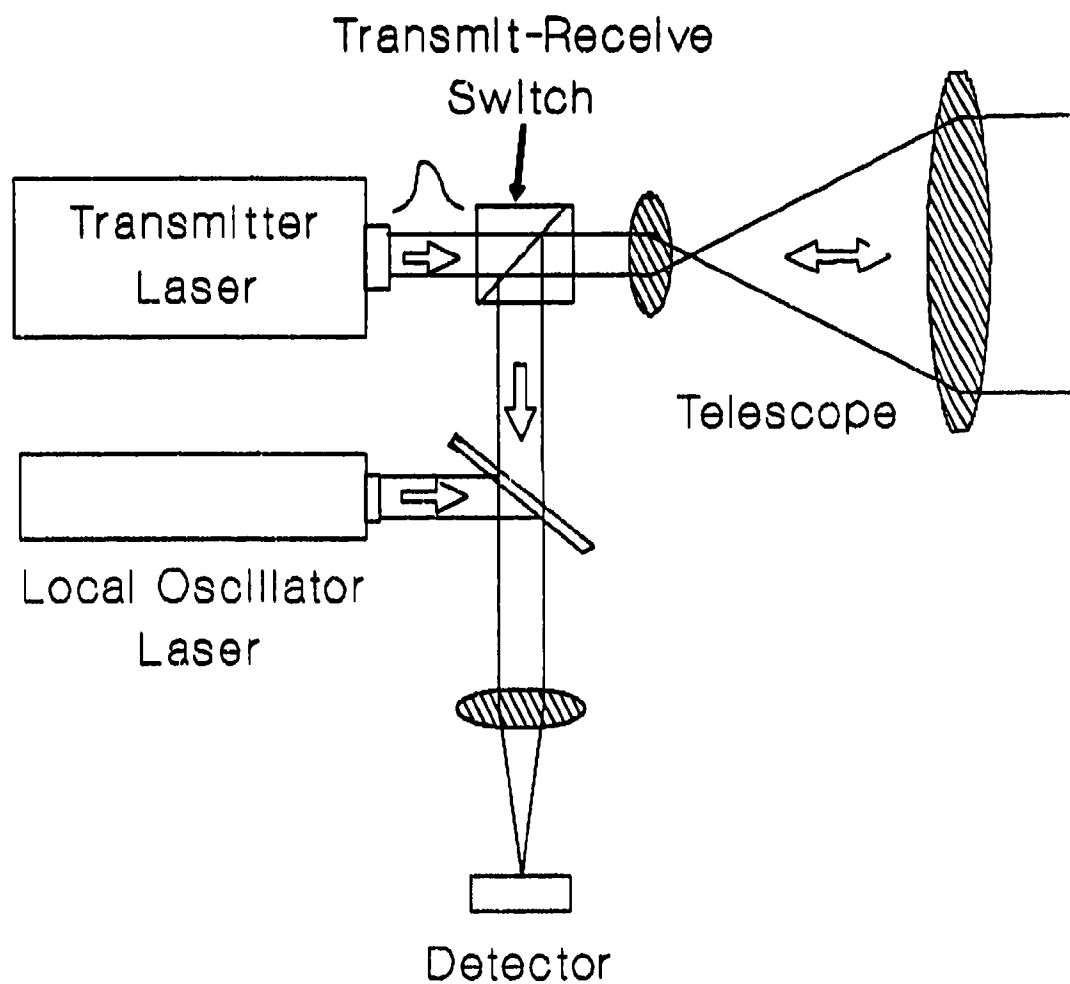


Figure 2-6. General Layout of a Monostatic Heterodyne Lidar

modulated by the difference or beat frequency between the reference and received beams. The detector output then consists of a beat signal whose mean frequency is proportional to the average wind velocity within the scattering volume and whose frequency spread is proportional to the wind variability or turbulence. The electronic bandwidth of the detector and downstream amplifiers filter the output signal to a finite bandwidth B .

The Doppler frequency shift Δf_D in the backscattered signal due to a wind velocity v along the beam path is given by

$$\Delta f_D = \frac{2}{\lambda} v \quad (2-40)$$

where λ is the wavelength of the transmitted light. The resulting beat frequency, f_m , is then

$$f_m = |f_{ref} - (f_t + \Delta f_D)| \quad (2-41)$$

where

f_{ref} = local oscillator optical frequency (Hz)

f_t = transmitter optical frequency (Hz)

Microscale turbulence within the scattering volume generates a distribution of particle velocities. The resulting backscattered signal has a Doppler frequency "spread" due to this distribution. The spectral width of the received signal, then, is due to the combined spectral widths of the transmitted pulse beam, the local oscillator beam, and the backscattered light. The spectral widths of the transmitter and local oscillator beams are inversely related to the coherence times of these beams. Therefore, in order to measure wind velocity with any accuracy, the coherence times for these lasers should be long. This requirement leads to the commonly used term *coherent lidar* in reference to heterodyne detection lidar.

Since the transmitted beam is pulsed, range information may be extracted from the received signal. If the output pulse is transmitted at time $t=0$, then the received signal at time t is due to a scattering volume at a range of $\frac{1}{2}ct$, where c is the speed of light. The scattering volume has transverse dimensions equal to the beam spot size at that range and longitudinal dimension $\frac{1}{2}c\tau$, where τ is the transmitted pulse length. Thus the lidar cannot resolve scattering volumes shorter than one half the pulse length. The minimum resolved scattering volume is often referred to as a range gate interval.

2.3.2. Characteristics of the Backscattered Signal

In this subsection, we will look at the key properties of the back-scattered light that is incident upon the lidar receiver. We may describe this optical signal statistically in terms of its power, frequency, and coherence.

The electric field of the backscattered signal is a sum of the electric fields from a large number of independent scatterers. Since the scatterers are randomly distributed throughout the scattering volume, the resulting electric field is a random phasor sum whose amplitude is Rayleigh distributed and whose phase is uniformly distributed (Goodman, 1985:44-50). In terms of instantaneous power, the return signal is then an exponentially distributed random variable with equal mean and standard deviation. The relative uncertainty in power is therefore 100%. For N independent measurements, the relative uncertainty falls to $100\%/\sqrt{N}$ (Hardesty et al., 1981:3768-3769).

The average optical power collected by the lidar receiver from a scattering volume at range R may be found using radiometry. Since we are primarily interested in long range detection, we may assume that the scattering volume is in the far field of the lidar receiver. That is, we assume that the scattering volume is essentially a point target. If

the transmitted pulse begins at $t=0$ and ends at $t=\tau_p$, then the total power collected by the receiver is the convolution of the pulse temporal power profile with the range dependent backscatter coefficient and transmission (Menzius and Hardesty, 1989:452). In symbols,

$$P_r(t) = \eta_o \int_{\frac{1}{2}c(t-\tau_p)}^{\frac{1}{2}ct} P_i\left(t - 2\frac{R}{c}\right) \beta_n(R) \left(\frac{A}{R^2}\right) \tau^2(R) dR \quad (2-42)$$

where

η_o = collection efficiency of optics

$P_r(t)$ = total optical power incident on receiver (W)

$P_i(t)$ = transmitted pulse temporal power profile (W)

$\beta_n(R)$ = volume backscatter coefficient ($\text{m}^{-1}\text{sr}^{-1}$)

A = area of receiver entrance aperture (m^2)

$\tau(R)$ = one-way transmission to range R

R = range to scattering volume (m)

Note the change in notation on the backscatter coefficient from previous definitions. The notation used here is more common in the lidar community, while the previous notation is more common in the optical scattering community. The backscatter coefficient and one-way transmission have been written as functions of range to underscore their strong range dependence.

If we assume that $\beta_n(R)$, $\tau(R)$, and R^{-2} do not change appreciably over the range gate interval between $\frac{1}{2}c(t-\tau_p)$ and $\frac{1}{2}ct$, then these terms may be pulled out of the integral above leaving only the pulse temporal profile term. The integral of the pulse power over the pulse length just gives the total energy E_i in the pulse times one half the speed of light. Note that E here denotes energy, not irradiance as in previous definitions. The simplified expression for received average power is then

$$P_r(t) = E_i \left(\frac{1}{2}c\right) \beta_n(R) \left(\frac{A}{R^2}\right) \tau^2(R) \quad (2-43)$$

The backscatter coefficient $\beta_n(R)$ at range R is the sum of the backscatter coefficients for molecules and aerosols, or

$$\beta_n(R) = \beta_n^m(R) + \beta_n^a(R) \quad (2-44)$$

where

$\beta_n^m(R)$ = molecular backscatter coefficient ($\text{m}^{-1}\text{sr}^{-1}$)

$\beta_n^a(R)$ = aerosol backscatter coefficient ($\text{m}^{-1}\text{sr}^{-1}$)

Likewise, the extinction coefficient $\beta_e(R)$ that contributes to the one-way path transmission $\tau(R)$ at range R is also the sum of molecular and aerosol extinction coefficients:

$$\beta_e(R) = \beta_e^m(R) + \beta_e^a(R) \quad (2-45)$$

where

$\beta_e^m(R)$ = molecular extinction coefficient (m^{-1})

$\beta_e^a(R)$ = aerosol extinction coefficient (m^{-1})

We noted above that the instantaneous power in the backscattered signal is an exponentially distributed random variable. As the particles move in random motion within the scattering volume, the instantaneous power changes. The rate at which signal power fluctuates is a function of particle velocities. After a short period of time, the particles have rearranged themselves enough that the new instantaneous signal power is independent of the previous power. In addition, the phase of the return signal is independent of the earlier phase; hence the two signals are uncorrelated or temporally incoherent. The time period over which the return signal remains coherent (at least partially) is the coherence time and depends on the distribution of particle velocities.

Using the Wiener-Khinchin Theorem, the power spectrum of the return signal is related to the autocorrelation of the signal by the Fourier transform (Goodman, 1985:74). Thus, high particle velocities cause short coherence times or narrow autocorrelations, which in turn mean

broad power spectrums. Low particle velocities correspond to narrow power spectrums. Assuming perfectly monochromatic, and hence infinitely continuous, illumination, the shape of the power spectrum is the same as the distribution of particle velocities. Therefore, we may interpret the spectrum as the distribution of Doppler shifts from the volume of particles.

At this point, let us consider backscatter from molecules and backscatter from aerosols separately. Most atmospheric aerosols are small enough that they move freely with the wind, and thus the mean Doppler shifts from aerosols and molecules within a scattering volume are equivalent. The distributions of velocities, however, are very different.

Molecular velocity distribution is a function of absolute temperature as given by the Maxwell velocity distribution (Tipler, 1987:69). The velocity distribution in one direction, say the x-direction, is a Gaussian distribution with standard deviation

$$\sigma_v = \sqrt{\frac{R'T}{M_A}} \quad (2-46)$$

where

σ_v = velocity standard deviation (m/s)

R' = universal gas constant (8.314 J/mole·K)

T = absolute temperature (K)

M_A = molar mass of air (kg/mole)

McCartney (1976:52) gives the molar mass of air as $M_A = 28.964$ g/mole.

Figure 2-7 shows a plot of σ_v versus altitude. As the plot indicates, molecular velocities in the atmosphere are fairly high. Even the very cold tropopause region sees molecular velocities of ≈ 250 m/s. The resulting power spectrum from molecular backscatter is very broad.

Because of their larger size, aerosols have a typical velocity spread of only about 1-2 m/s (Menzies and Hardesty, 1989:454), and the resulting power spectrum is relatively narrow. The range of mean wind s

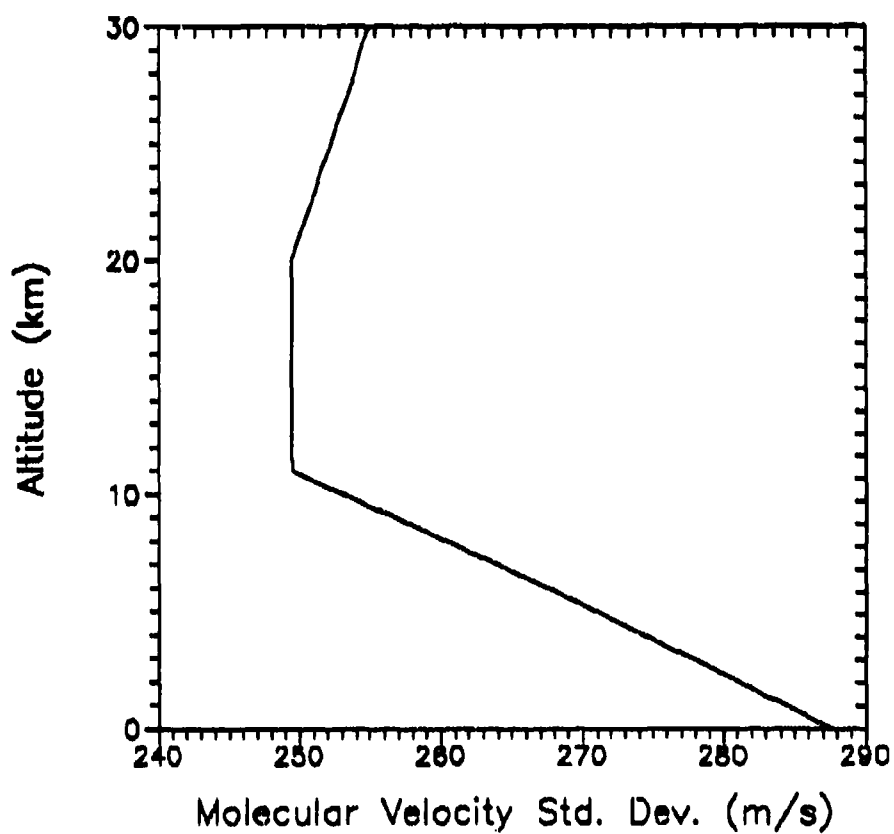


Figure 2-7. Standard Deviation of Molecular Velocity versus Altitude.
Computed using the U.S. Standard Atmosphere (1976).

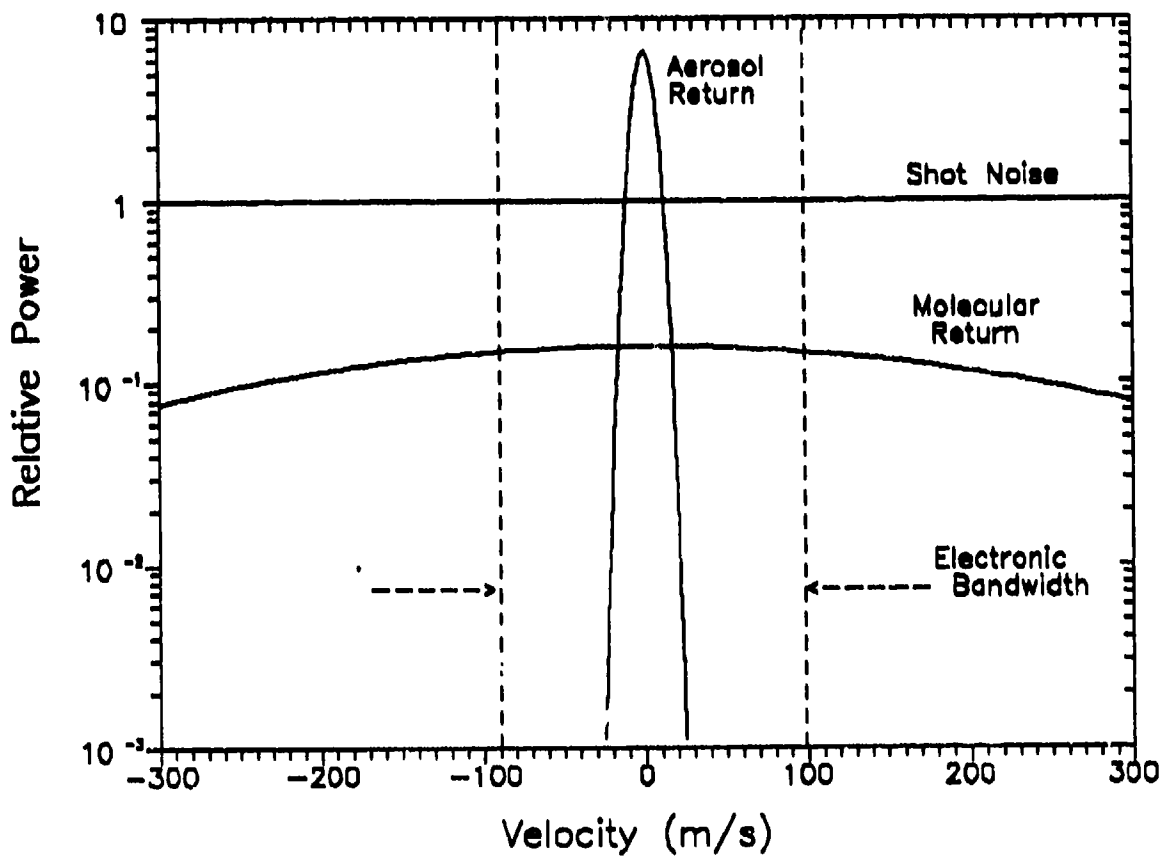


Figure 2-8. Typical Power Spectrum of Molecular and Aerosol Returns

peeds in the atmosphere is usually well within ± 50 m/s. Even the peak velocity in the 707 wake vortex is only 18 m/s. Over the range of mean air velocities, the power spectrum of molecular backscatter is approximately flat. For this reason, molecular backscatter should really be considered as noise power, not signal power. Signal power, therefore only comes from aerosol backscatter. Figure 2-8 illustrates the relationship between aerosol and molecular Doppler spectrums.

The spatial coherence of the backscattered signal is also degraded by the atmosphere. Random fluctuations in the refractive index of air between the lidar and the scattering volume are known as refractive turbulence. The refractive index structure constant, C_n^2 , indicates the strength of refractive turbulence and is given by

$$C_n^2 = \frac{\overline{(n_1 - n_2)^2}}{L^{2/3}} \quad (2-47)$$

where

n_1 = refractive index at point 1

n_2 = refractive index at point 2

L = distance between points 1 and 2 (m)

C_n^2 has units of $m^{-2/3}$. The bar over the numerator in the previous equation denotes ensemble average.

The effect of propagating light through a turbulent medium is a reduction in the spatial coherence of the wavefront. The transverse coherence length, r_0 , is a measure of spatial coherence as it indicates the distance along the wavefront over which the wavefront is coherent. The transverse coherence length of the backscattered signal is given by (Huffaker and Targ, 1988:66)

$$r_0 = 0.0581 \lambda^{3/5} R \left[\int_0^R C_n^2(r) r^{5/3} dr \right]^{-3/5} \quad (2-48)$$

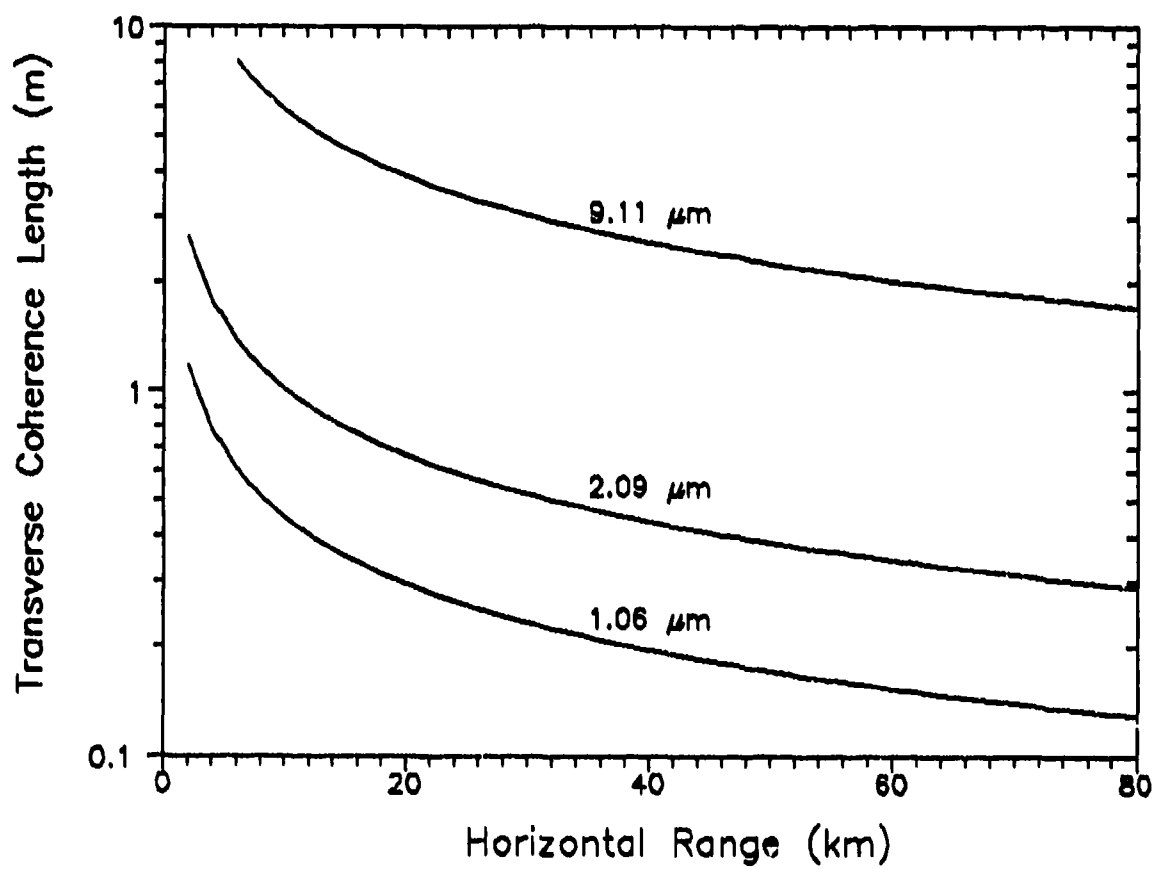


Figure 2-9. Transverse Coherence Length versus Range for $C_n^2=10^{-17} \text{ m}^{-2/3}$

where R is the range to the scattering volume. All lengths in this equation are in units of meters.

At nominal aircraft cruise altitudes between 5-15 kilometers (16-50 kft), C_0^2 is fairly constant at around $10^{-17} \text{ m}^{-2/3}$ (Fenn et al., 1985:18-72; Goodman, 1985:429). This value will be used in subsequent analyses. Figure 2-9 shows the transverse coherence length plotted versus range over a horizontal path for the three infrared wavelengths of interest.

2.3.3. Signal-to-Noise Ratio

Noise limits the ultimate sensitivity of any lidar system. Therefore, the ratio of signal power to noise power in the output signal gives a good one-parameter indicator of the performance capability of a given lidar under a given set of conditions. Here we will develop an equation to express the signal-to-noise ratio of a heterodyne detection Doppler lidar.

After collection by the telescope, the received light is photomixed with the local oscillator reference beam and focused down onto the detector. The resulting heterodyne optical signal incident on the detector has the form (Post, 1985)

$$P_i = P_{i0} + P_r + 2\eta_h \sqrt{P_{i0} P_r} \cos(\omega_r - \omega_{i0})t \quad (2-49)$$

where

$P_i(t)$ = optical power incident on detector (W)

P_{i0} = local oscillator power (W)

P_r = return signal power (W)

η_h = heterodyne mixing efficiency

ω_{i0} = local oscillator optical frequency (rad/s)

ω_r = received optical frequency (rad/s)

Following the previous discussion about molecular and aerosol signal characteristics, only the aerosol backscatter contributes to meaningful signal. If we denote the optical power from aerosols as P_{10} , then the signal current $i_s(t)$ out of the detector, with D.C. components filtered out, has the form

$$i_s(t) = 2\eta_h \left(\frac{\eta_{qs}e}{h\nu} \right) \sqrt{P_{10}P_s} \cos(\omega_{10} - \omega_s)t \quad (2-50)$$

where

η_{qs} = detector quantum efficiency

e = electron charge (C)

h = Planck's constant ($6.626 \cdot 10^{-34}$ J s)

ν = optical frequency (Hz)

We may now find an expression for the noise power in the output current. Shot noise in the output signal is due primarily to local oscillator power and is given by

$$\begin{aligned} \langle i_n^2 \rangle_{shot} &= 2eBi \\ &\approx 2eB \left(\frac{\eta_{qs}e}{h\nu} \right) P_{10} \end{aligned} \quad (2-51)$$

where

$\langle i_n^2 \rangle_{shot}$ = average shot noise power (A^2)

i = average detector current (A)

B = electronic bandwidth (Hz)

Shot noise usually dominates thermal noise, and thus thermal noise is neglected. The noise contribution from molecular backscatter may be considered background noise. Background noise power is then

$$\langle i_n^2 \rangle_{back} = 2 \left(\frac{\eta_{qs}e}{h\nu} \right)^2 P_b P_{10} \quad (2-52)$$

where

$\langle i_n^2 \rangle_{back}$ = average background noise power (A^2)

P_b = optical power from molecular backscatter in bandwidth B (W)

The total noise power is the sum of all noise power terms. At the wavelengths of interest, however, shot noise dominates background noise from molecular scattering. Simulations show that background noise is less than 2% of shot noise for a lidar located at 9 kilometers altitude looking horizontally. Thus we may neglect background noise.

Signal-to-noise ratio, SNR , is the ratio of total average signal power to average noise power as given by

$$SNR = \frac{\langle I_s^2 \rangle}{\langle I_n^2 \rangle_{shot} + \langle I_n^2 \rangle_{back}} \quad (2-53)$$

$$= \frac{\langle I_s^2 \rangle}{\langle I_n^2 \rangle_{shot}}$$

Averaging signal power over time gives

$$\langle I_s^2 \rangle = 2\eta_h \left(\frac{\eta_{qs} c}{h\nu} \right)^2 P_s P_{lo} \quad (2-54)$$

where

$\langle I_s^2 \rangle$ = average signal power (A^2)

P_s = optical power from aerosol backscatter (W)

Assuming shot noise dominates other noise terms, then signal-to-noise ratio reduces to

$$SNR = \frac{E_s \eta_o \eta_h \eta_{qs} \beta_{sh}''(R) A \lambda \tau^2(R)}{2hBR^2} \quad (2-55)$$

after substituting for $\langle I_s^2 \rangle$ and $\langle I_n^2 \rangle_{shot}$ and simplifying. The term $\beta_{sh}''(R)$ is the aerosol backscatter coefficient at range R . This equation is the ideal signal-to-noise ratio for an unfocused heterodyne lidar assuming each scattering volume acts as a point target.

A number researchers have studied receiving efficiency for optical heterodyne receivers. Sonnenschein and Horrigan (1971) derived a signal reduction factor to take into account the effect of wavefront curvature of the backscattered light and the finite size of the scattering volume.

The authors assumed an untruncated Gaussian output beam, spherical scatterers, and a Gaussian plane wave output from the local oscillator. Clifford and Wandzura (1981) modified the signal reduction factor to include the reduction of spatial coherence of the backscattered light due to atmospheric refractive turbulence. The resulting signal reduction factor, which multiplies the signal-to-noise ratio above, is given by

$$SRF = \left[1 + \left(\frac{D}{2r_0} \right)^2 + \left(\frac{\pi D^2}{4\lambda R} \right)^2 \left(1 - \frac{R}{f} \right)^2 \right]^{-1} \quad (2-56)$$

where

SRF = signal reduction factor

D = diameter of receiver (m)

r_0 = transverse coherence length (m)

f = telescope focus range (m)

Incorporating the signal reduction factor and an additional factor, A_1 , to account for the fact that the system may not be completely shot noise limited (Post, 1985), the final form of the heterodyne lidar signal-to-noise ratio becomes

$$SNR = \frac{E_s \eta_s \eta_a \eta_o \beta_n^2(R) \pi D^2 \lambda \tau^2(R) A_1 SRF}{8 h B R^2} \quad (2-57)$$

where the receiving aperture is assumed to be circular with area $\pi D^2/4$.

2.3.4. Velocity Estimation

Since our primary objective is to measure airflow characteristics within an aircraft wake, we need a method of extracting this information from the backscattered signal. The two most meaningful parameters to describe the airflow characteristics in a scattering volume are mean velocity and velocity width. Mean velocity is simply the average velocity of aerosols along the beam path within a range gate. Velocity width indicates the variance or spread of aerosol velocities within a

scattering volume. Most of the existing velocity and velocity width estimation techniques have been developed for Doppler weather radar and are easily adapted for Doppler lidar.

The pulse pair estimation algorithm is probably the most widely used estimator of velocity and velocity width. Zrnic (1977) described the pulse pair algorithm for estimating first three spectral moments (signal power, mean velocity, and velocity width) from Doppler radar weather echoes. In a later paper (Zrnic, 1979) he compares the pulse pair estimator to estimates derived from spectral processing using Fourier transforms and then compares the estimation errors to the Cramer-Rao lower bound error derived from Maximum Likelihood estimates. It is the estimation error expressions that we are most interested in for our performance analysis.

To simplify the analysis procedure, we will only be interested in estimation of velocity (or spectral) width. The primary justification for this decision is that typical range gate lengths are longer than the transverse wake dimensions and thus the average velocity in the range gate generally averages to zero. In addition, we will only look at the Cramer-Rao lower bound error for width estimation, keeping in mind that most practical signal processors will not be able to equal this performance. This decision was made because the error expressions for the pulse pair and spectral processing width estimators are very complex and not really worth the extra analysis effort.

Since the Doppler shift is much higher at infrared wavelengths than at microwave wavelengths, complete velocity information may be extracted from a single lidar pulse, as compared to many radar pulses. Thus the Cramer-Rao error expression given by Zrnic was modified for lidar by making the following substitutions and redefinitions:

$T_s = T$ - intrapulse sample time

$\rho = \omega T_s$ - ratio of signal spectral width (ω) to the full electronic bandwidth

$\tau_p = MT_s$ - pulse duration

M - number of intrapulse samples

In addition, the expression has been converted from frequency domain, as given by Zrnic, to velocity domain using

$$\sigma_{\Delta v} = \frac{\lambda}{2} \sigma_{\omega} \quad (2-58)$$

where

$\sigma_{\Delta v}$ - standard deviation of velocity width estimate (m/s)

σ_{ω} - standard deviation of frequency width estimate (Hz)

So finally, the Cramer-Rao lower bound velocity width error is given by (Zrnic, 1979: eq.'s A.39 and A.41)

for high SNR: (2-59)

$$\sigma_{\Delta v} = \frac{3\sqrt{5}\rho^3\lambda}{\sqrt{\tau_p T_s}}$$

and for low SNR:

$$\sigma_{\Delta v} = \frac{\pi^{1/4}\rho^{3/2}\lambda}{\sqrt{\tau_p T_s SNR}}$$

These expressions indicate the typical errors associated with estimating velocity spread or width.

3. Preliminary Considerations

At this point, some discussion of preliminary considerations is in order to set the groundwork for analysis of atmospheric and exhaust aerosols. This chapter lays out the criteria that will be used in the analysis along with applicable assumptions and justifications. In particular, lidar system parameters to be used will be given, wake parameters for four different test case aircraft will be computed, detection geometry will be defined, signal processing requirements will be established, and molecular absorption effects will be quantified.

3.1. Lidar System Parameters

Most of the base lidar system parameters to be used in this analysis were taken from Thomson et al. (1989). Table 3-1 lists the base system parameters for all three lidars. The laser parameters, pulse energy and pulse width, reflect modest requirements for an airborne lidar system. These parameters do not necessarily imply the existence of such lasers; however, active development work on all three lasers is currently underway, and it is not unreasonable to assume that they will be available in the next few years (Thomson et al., 1989:36,60-62).

The detector quantum efficiencies used were verified by knowledgeable researchers. In the 9-10 μm band, Mercury-Cadmium-Telluride (HgCdTe) detectors are available, both photoconductive and photovoltaic, with quantum efficiencies from 60-90% at bandwidths below 300 MHz (Schreiber, 1990). A nominal value of 80% was chosen. For the 1-2 μm band, Indium-Gallium-Arsenide (InGaAs) and Germanium (Ge) detectors are available with quantum efficiencies of 70-80% at low bandwidths (Spears, 1990). Again, a value of 80% was chosen for both 1.064 and 2.091 μm detectors. Electronic bandwidth for each wavelength corresponds to a velocity bandwidth of 50 m/s.

Table 3-1. Base Lidar System Parameters

Parameter	System #1	System #2	System #3
Laser Medium	Nd:YAG	Ho:YAG	CO ₂
Wavelength, λ (μm)	1.064	2.091	9.115
Pulse Energy, E (J)	0.2	0.2	0.2
Pulse Duration, τ_p (μs)	0.1	0.2	1.0
Receive/Transmit Aperture Diameter, D (m)	0.3	0.3	0.3
Optics Transmission (two-way), η_o	0.5	0.5	0.5
Heterodyne Mixing Efficiency, η_h	0.5	0.5	0.5
Detector Quantum Efficiency, η_d	0.8	0.8	0.8
Shot Noise Correction Term, A_s	0.5	0.5	0.5
Electronic Bandwidth, B (MHz)	94	48	11
Telescope Focus Range, f (km)	∞	∞	∞

Detection out to 50 miles (80 km) in range is desirable. Lidar performance, therefore, will be evaluated at ranges between 0-80 km. An unfocused telescope (focused at ∞) will be used in all calculations. While the signal-to-noise ratio at a given range may be improved significantly by focusing the telescope at or somewhat farther than that range, the signal-to-noise ratio at other ranges suffers (Thomson et al., 1989). In addition, for Gaussian output beams, focusing at ranges beyond the Rayleigh range of the telescope is not possible due to diffraction limitations. The Rayleigh range is given by the equation (Verdeyen, 1989:69)

$$z_o = \frac{\pi w_o^2}{\lambda} \quad (3-1)$$

where

z_o = Rayleigh range (m)

w_o = radius of beam waist (m)

λ = wavelength (m)

The Rayleigh ranges for the three wavelengths of interest and for a 0.3 m telescope are 66.4 km, 33.8 km, and 7.7 km at 1.064 μm , 2.091 μm , and 9.115 μm , respectively. Furthermore, practical hardware considerations limit telescope focusing to less than about 50 km (Zhao and Post, 1989:188).

3.2. Aircraft Examples

Four hypothetical aircraft will be used to analyze wake detection. These aircraft were chosen to span a wide range of potential aircraft sizes and missions. Included are large and medium transport aircraft and large and small fighter aircraft. The pertinent dimensions and cruise parameters for each of these aircraft are listed in Table 3-2. Note that aircraft velocities used here are subsonic or transonic. Supersonic velocities will not be considered.

Table 3-2. Test Aircraft Dimensions and Cruise Parameters

Parameter	Large Transport	Medium Transport	Large Fighter	Small Fighter
Wingspan, s (m)	65	45	13	8
Mass (fully loaded), M (kg)	350,000	135,000	25,000	11,000
Cruise Speed, V_∞ (m/s)	250	235	300	300
Cruise Altitude, h (km)	10.3	10.3	12.2	12.2
Air Density at Altitude, ρ (kg/m ³)	0.398	0.398	0.302	0.302
Wing Loading Constant, K	0.785	0.785	0.785	0.785
Engines	4 @ 40,000 lbs thrust each	4 @ 14,000 lbs thrust each	2 @ 25,000 lbs thrust each	1 @ 10,000 lbs thrust

Applying the wake models presented in chapter 2, we may calculate the size of the stable wake and the air velocities within it for each of these aircraft at the given cruise conditions. Table 3-3 lists these

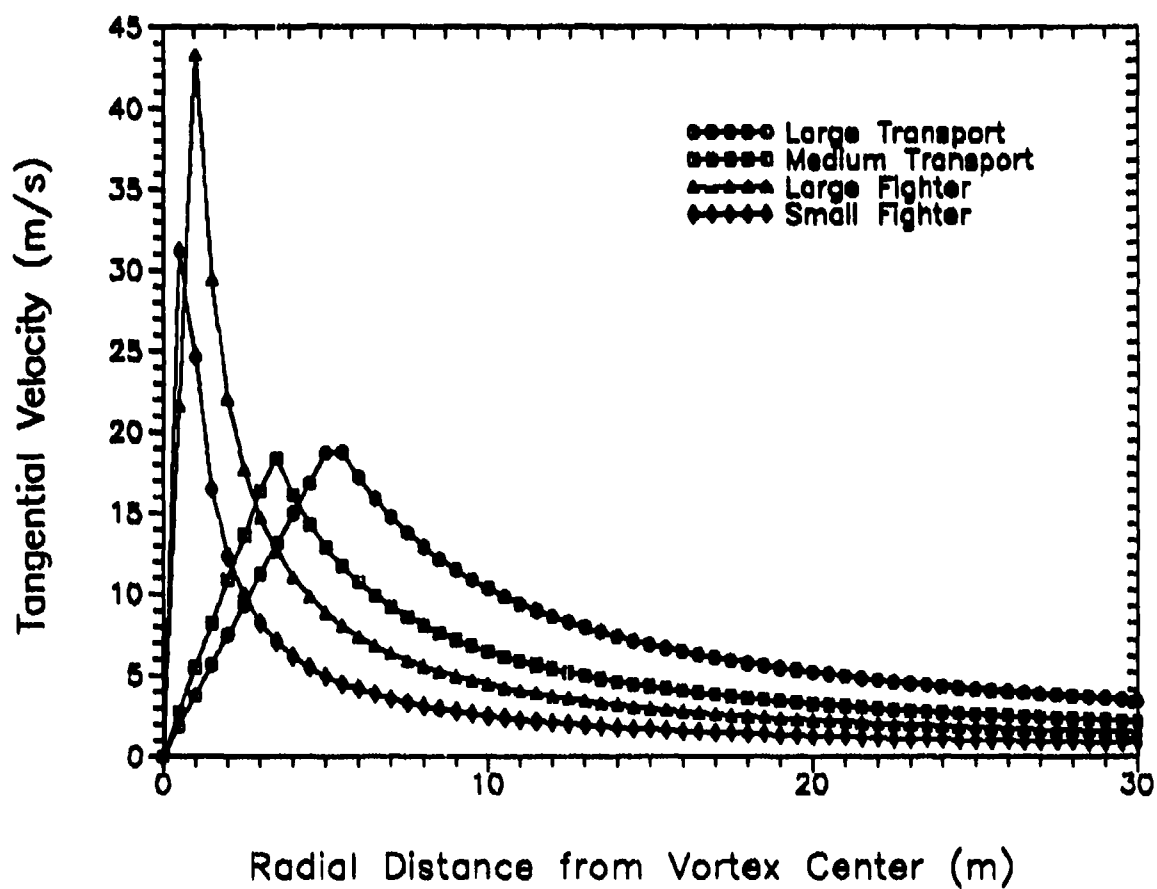


Figure 3-1. Tangential Velocity Profiles of Test Aircraft

wake parameters for all four aircraft. In addition, Figure 3-1 shows the tangential air velocity about one of the wake vortices as a function of distance from the vortex center.

Table 3-3. Wake Parameters for the Four Test Aircraft

Parameter	Large Transport	Medium Transport	Large Fighter	Small Fighter
Vortex Separation, b (m)	53.3	34.9	10.2	6.4
Vortex Core Radius, r_c (m)	5.3	3.4	1.0	0.6
Peak Tangential Velocity, V_{peak} (m/s)	19.1	18.6	42.3	48
Sink Velocity, V_s (m/s)	1.9	1.8	4.2	4.7
Core Drag Velocity, V_d (m/s)	13.5	13.2	29.9	33.9
Thrust Velocity, V_t (m/s)	0.1	0.1	0.3	0.3
Recirculation Cell Width (m)	111	73	21	13
Recirculation Cell Height (m)	92	60	18	11
Wake Length, L_w (km)	21.6	13.5	2.2	1.2

3.3. Geometry

To reduce the analysis problem to a manageable level, we must make some assumptions about the detection geometry. First, let us assume that the laser beam passes horizontally through the wake. This assumption is a good one since we are primarily interested in near horizontal air-to-air detection at long range. Second, we may assume that the transverse dimension of the laser beam (the width) is small compared to the wake dimensions. Assuming the transmitted beam has a Gaussian profile and is unfocused, the beam spot size at a distance z from the lidar transmitter is given by (Verdeyen, 1989:69)

$$w(z) = w_0 \left[1 + \left(\frac{z}{z_0} \right)^2 \right]^{1/2} \quad (3-2)$$

where

$w(z)$ = beam spot radius at distance z (m)

z_0 = Rayleigh range (m)

Since the output beam is roughly 0.3 m in diameter (see Table 3-1), the beam diameters at a range of 80 km are 0.47 m, 0.77 m, and 3.1 m at 1.064 μm , 2.091 μm , and 9.115 μm , respectively. These beams are all smaller than the recirculation cell diameters given in Table 3-3.

In analyzing return signals from aircraft wakes, we therefore only need to consider the vertical height of the beam within the wake and the horizontal angle between the laser and the aircraft flight direction. Figure 3-2 shows this simplified geometry.

Two final geometric assumptions concerning the beam path will be made. First, we will use the flat earth assumption; that is, curvature of the earth will be neglected. This assumption leads to an error in vertical height of about 0.2 km over a 50 km horizontal path on the ground. Second, we will neglect any refractive bending of the lidar beam due to the change in atmospheric index of refraction with altitude.

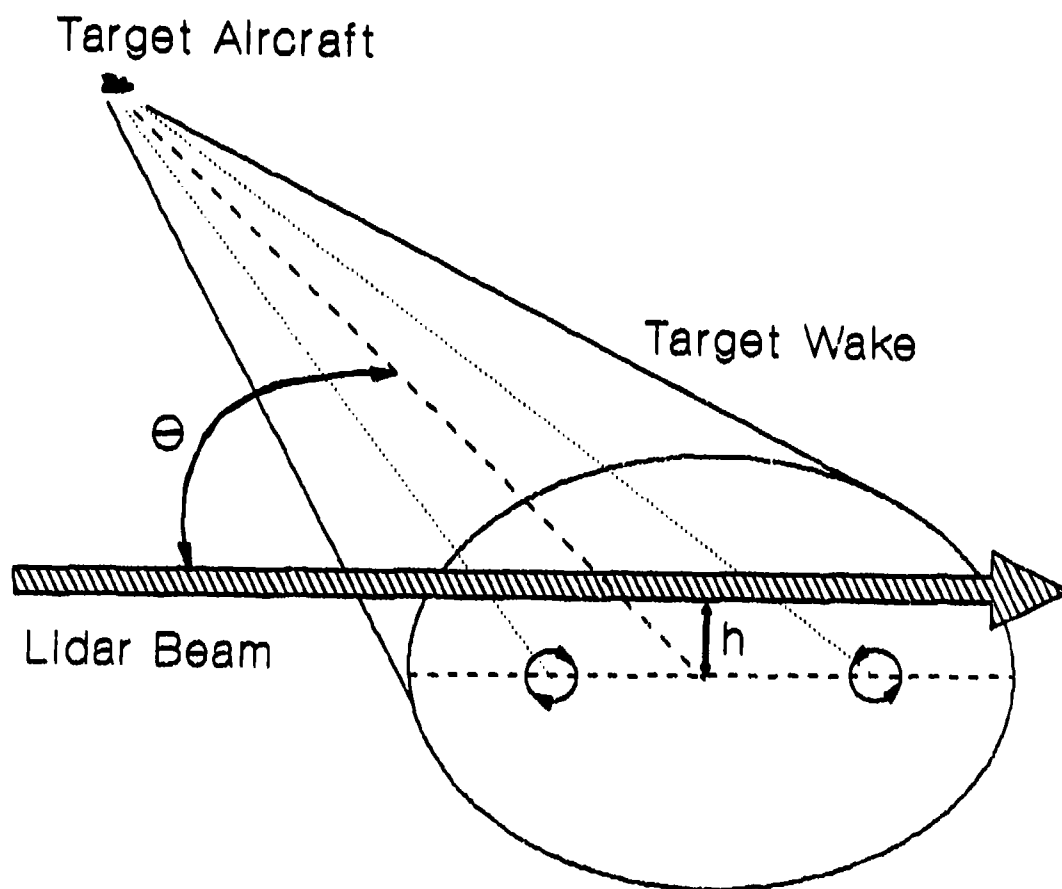


Figure 3-2. Simplified Wake Detection Geometry

3.4. Signal Processing

The return signal from any given range gate interval contains spectral information on the distribution of aerosol velocities within the scattering volume. In order to better understand how to extract this information and identify signals containing wake signatures, we should see what the returns from a wake look like.

To get an idea of the general shape of the return spectrum from within a wake, a computer simulation was performed to generate a two dimensional flow field in the cross section of the medium transport wake. The return signal consisted of the sum of all the horizontal velocity components along a 150 m segment, or "range gate", centered horizontally on the wake. The "beam" was then scanned vertically from the vortex center to see how the return spectrum varied with vertical distance. The simulation assumed that the beam width was smaller than the 2 m resolution of sample points within the flow field. In addition, the lidar beam was assumed to be perpendicular to the length of the wake. Figure 3-3 show these simulated return spectrums for vertical samples from 2-14 m from the vortex center.

As Figure 3-3 indicates, the return signal from the wake center is very narrow, with all the energy centered about the zero velocity point. As the beam moves vertically up or down from the center, however, the return spectrum quickly becomes very broad, with significant energy in the higher velocity components. The majority of the signal energy remains, though, near zero velocity. As the beam continues to scan vertically up or down, the spectrum slowly begins to narrow again. While the spectra do only have one main lobe, they do not appear to be Gaussian in shape. In all cases, since the simulated range gate was centered on the wake, the average velocity was zero.

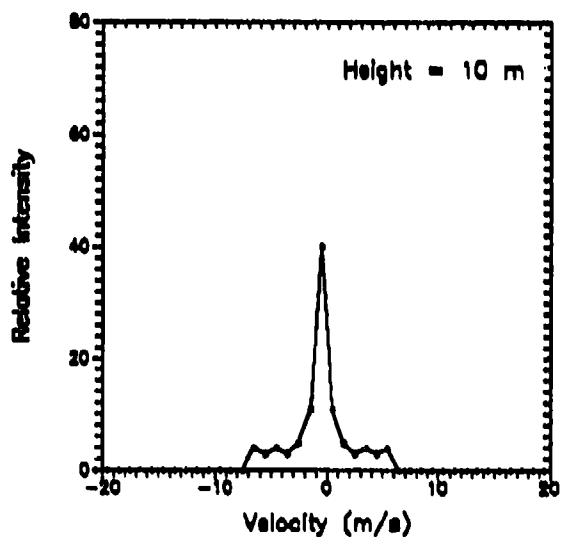
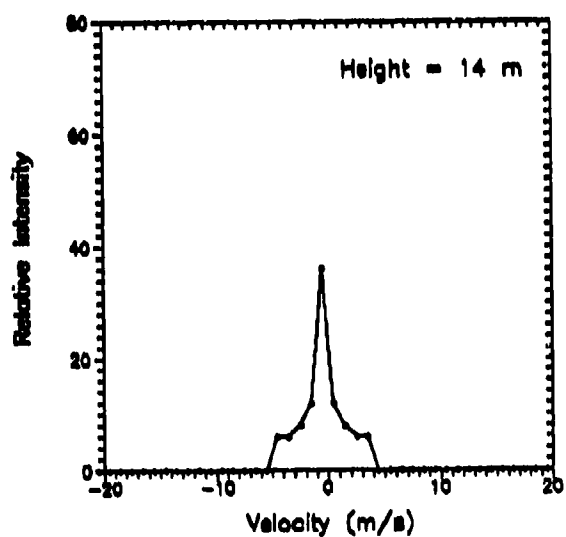
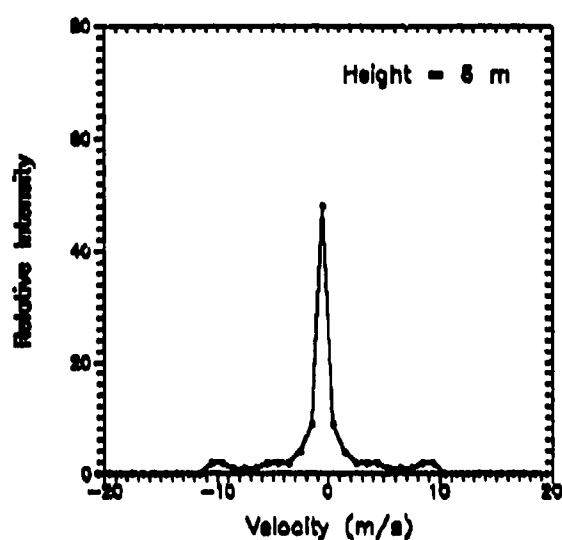
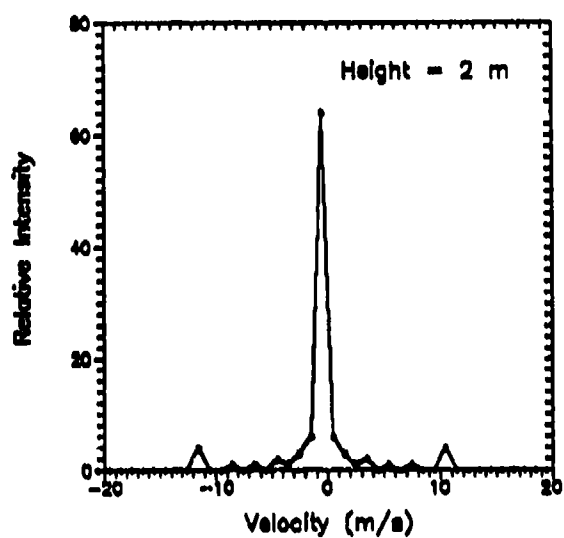


Figure 3-3. Simulated Return Spectra for Several Vertical Samples through the Wake of a Medium Sized Transport Aircraft

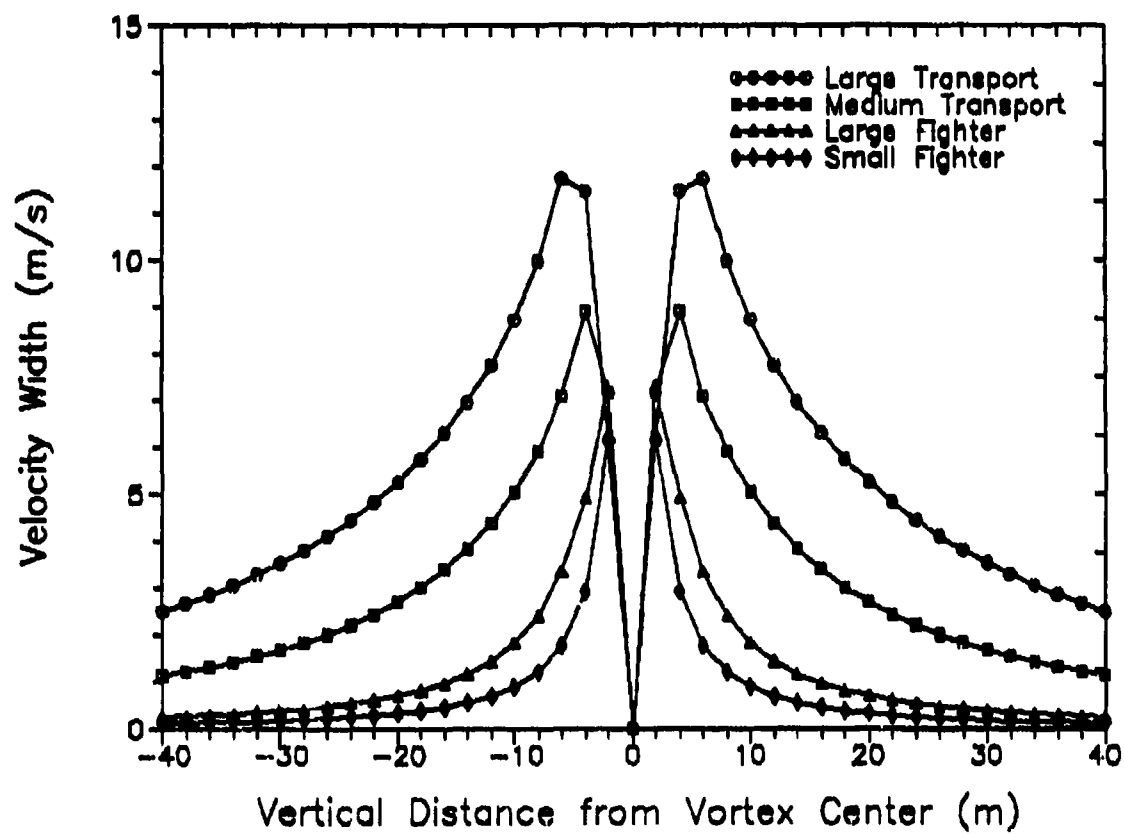


Figure 3.4. Velocity Width of Return Spectra from the Vertically Scanned Wakes of 4 Aircraft

Probably the most obvious feature of the return spectra from the wake is the wide spread of velocities. Figure 3-4 shows the velocity width (taken as twice the velocity standard deviation) of the return signal plotted versus vertical distance from the vortex center for the four test aircraft. The graph clearly shows the wide spread in velocity distribution near the vortex cores. Since typical spectrum width due to atmospheric turbidity is only about 1-2 m/s, the 6-12 m/s spread due to wake turbulence seems to be a good indicator of the presence of a wake in the return signal.

Range gate width affects the return spectrum a great deal. For the previous simulation, the range gate interval was 150 m, which corresponds to a pulse duration of 1 μ s. Better range resolution may be obtained by using shorter pulse durations, but this improvement comes at the expense of lower frequency resolution. On the other hand, better frequency/velocity resolution may be obtained at the expense of longer range resolution by using longer pulses. Figures 3-5.a-d show the effect of different range gate lengths (80, 150, and 750 m) on the return signal velocity width for the four test aircraft. As the graphs show, the velocity width decreases with increasing range gate length since the turbulent wake makes up a smaller fraction of the total signal.

To estimate how much signal-to-noise is required to detect wake signals we will use the Cramer-Rao lower bound error for the Maximum Likelihood velocity width estimator as presented in chapter 2. Plots of width estimation error are shown in Figures 3-6.a and 3-6.b for four different "true" spectral widths. Figure 3-6.a is for the 1.064 μ m case with a pulse duration of 0.1 μ s, while Figure 3-6.b is for the same wavelength with a 0.5 μ s pulse duration. Due to wavelength scaling effects, these plots are approximately identical to the error plots for

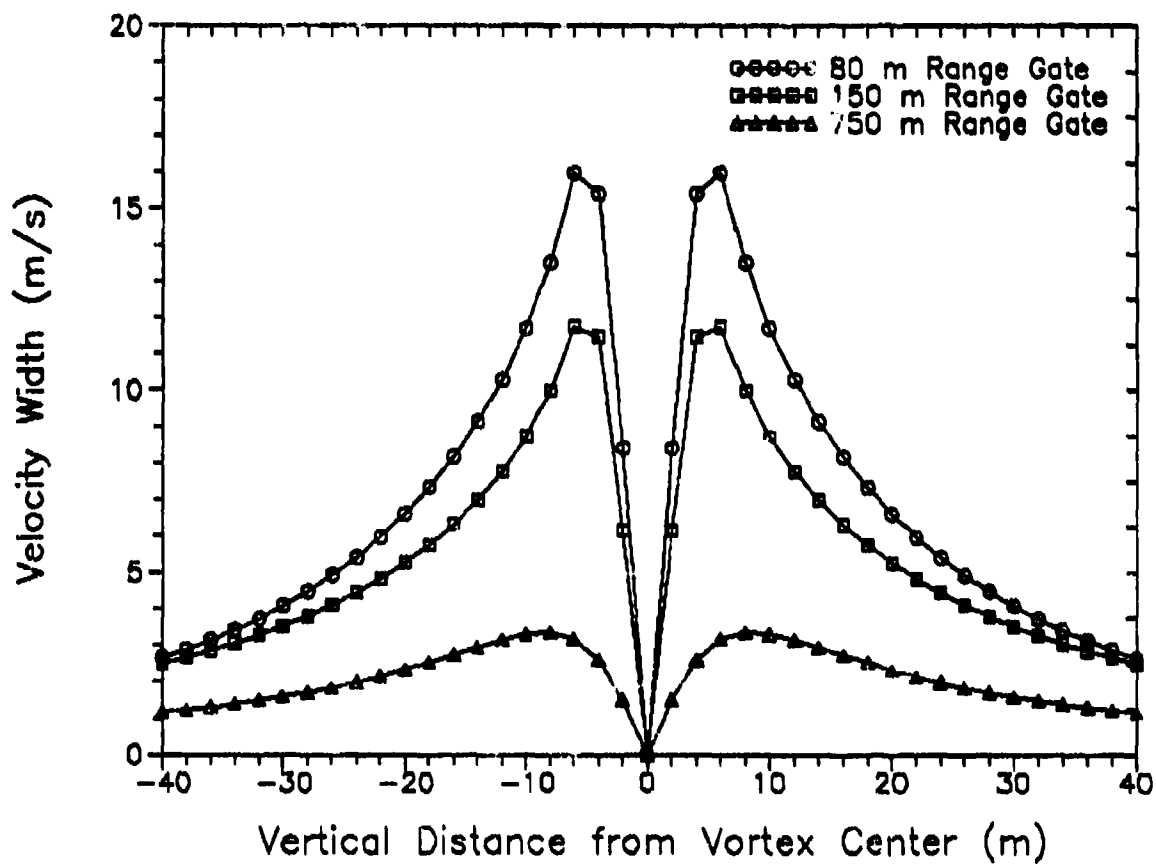


Figure 3-5.a. Velocity Width of Return Spectra from the Large Transport Wake for 3 Different Range Gate Intervals

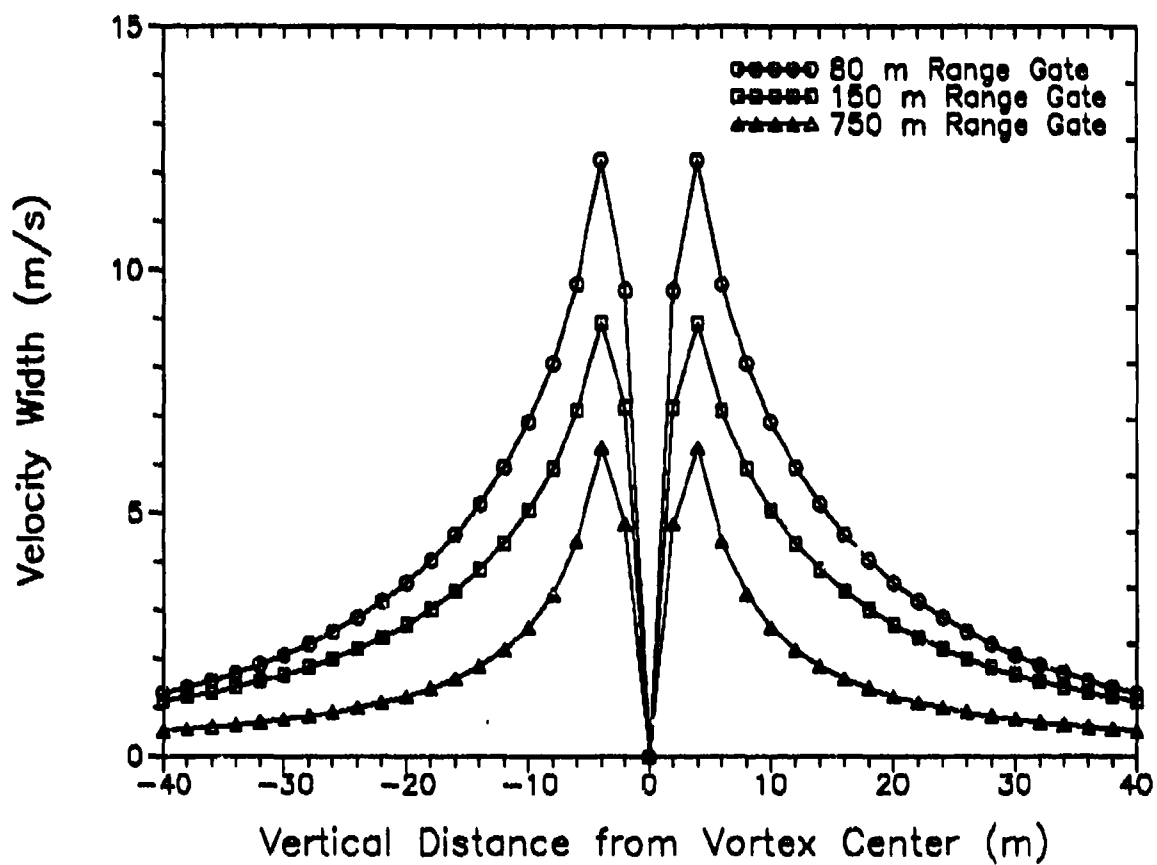


Figure 3-5.b. Velocity Width of Return Spectra from the Medium Transport Wake for 3 Different Range Gate Intervals

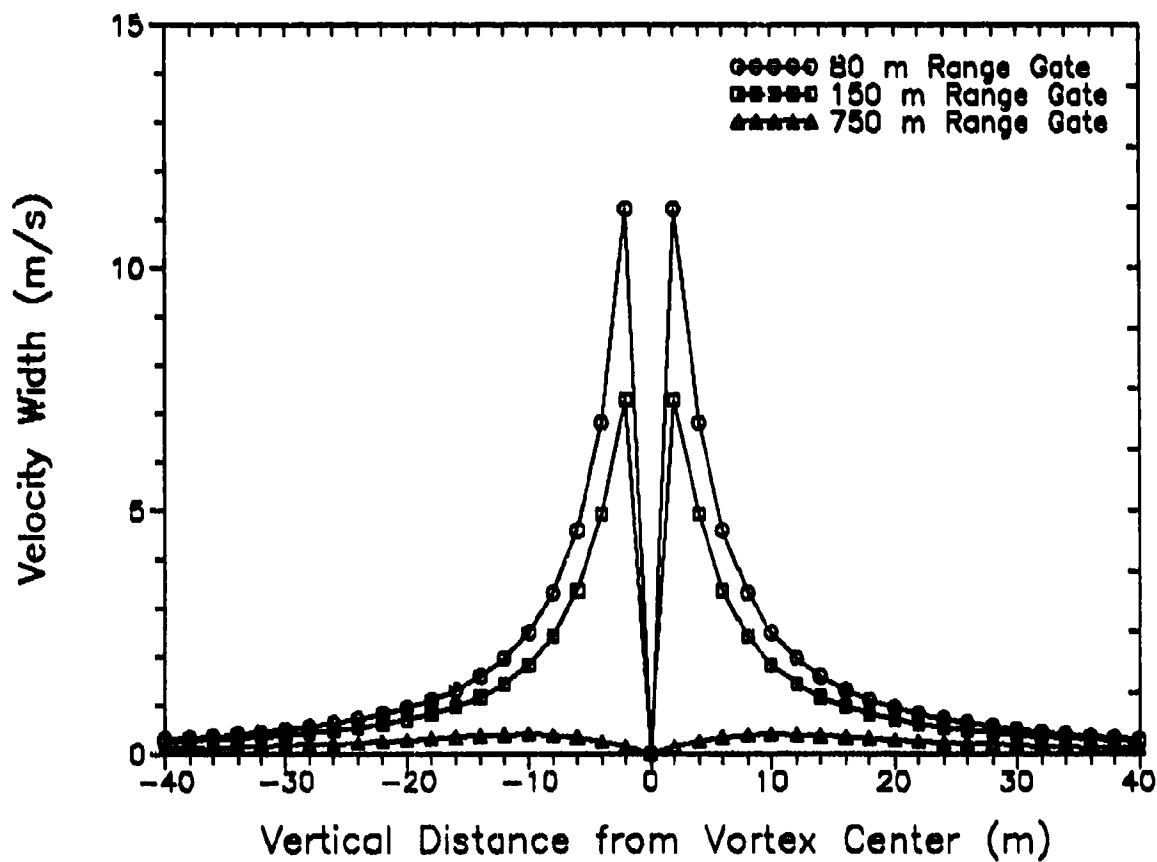


Figure 3-5.c. Velocity Width of Return Spectra from the Large Fighter Wake for 3 Different Range Gate Intervals

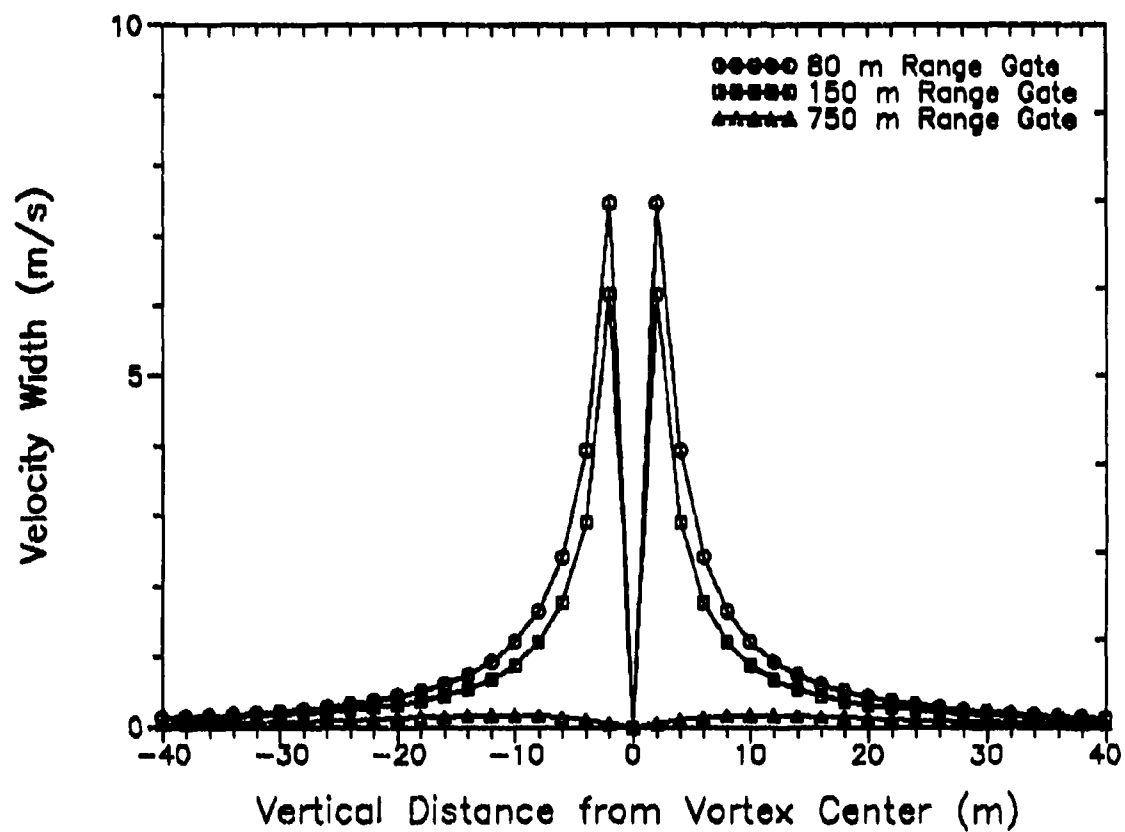


Figure 3-5.d. Velocity Width of Return Spectra from the Small Fighter Wake for 3 Different Range Gate Intervals

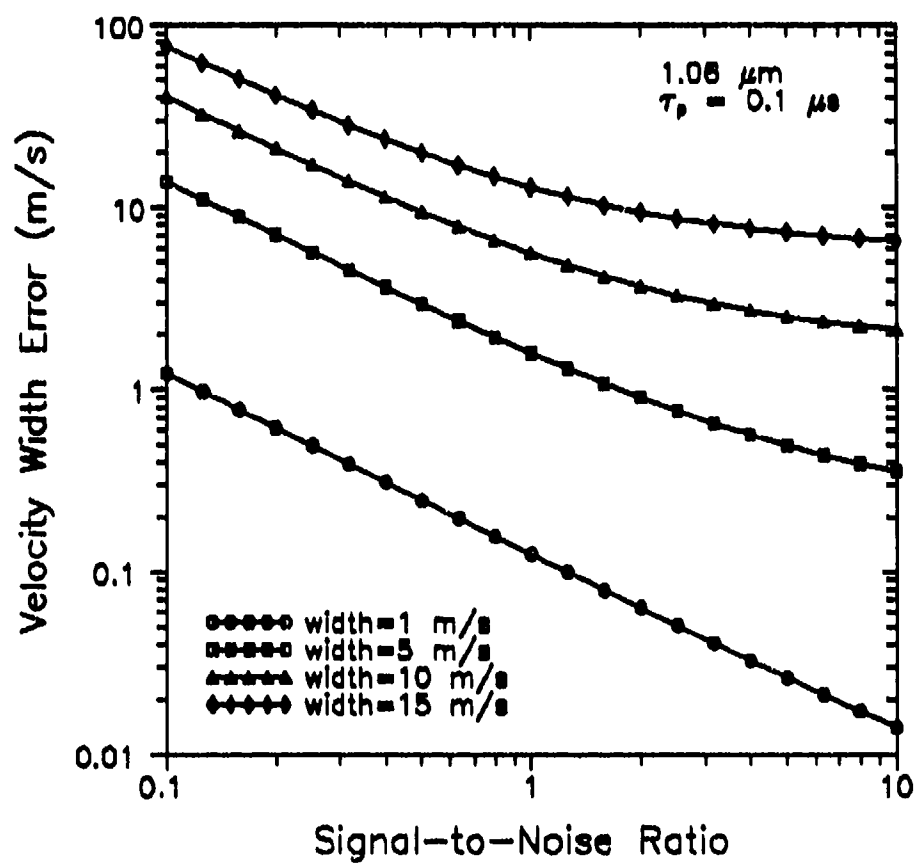


Figure 3-6.a. Velocity Width Estimation Error for Short Pulse Duration and Four "True" Spectral Widths

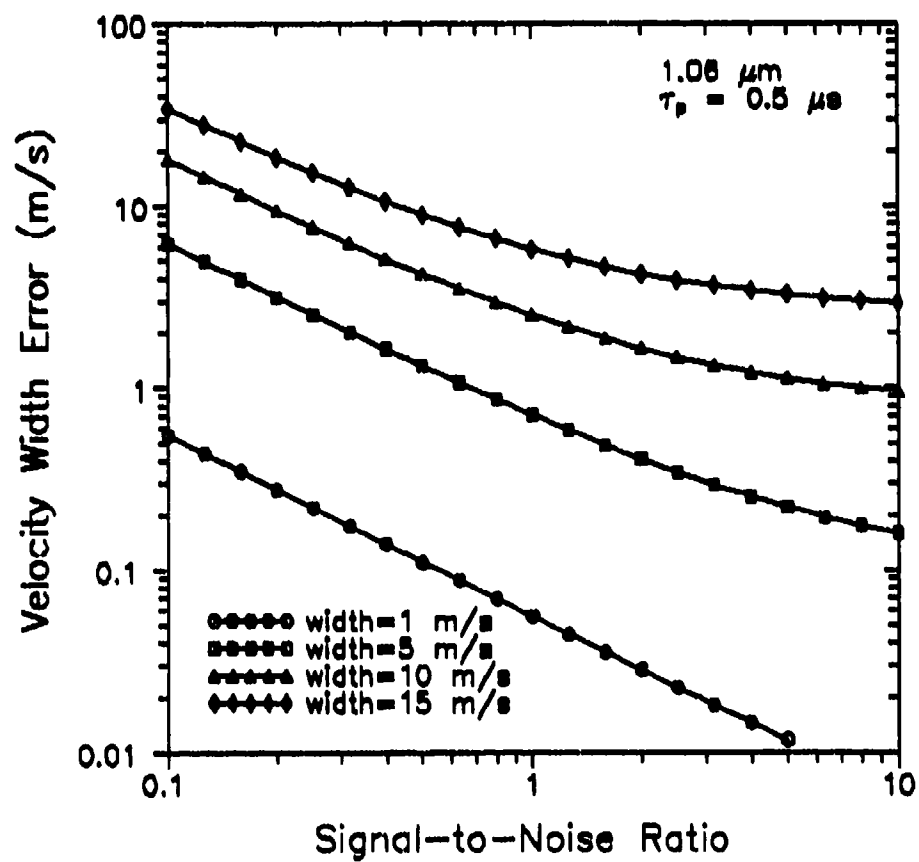


Figure 3-6.b. Velocity Width Estimation Error for Long Pulse Duration and Four "True" Spectral Widths

0.2 μ s and 1.0 μ s pulse durations at 2.091 μ m and 1.0 μ s and 5.0 μ s pulse durations at 9.115 μ m. The plots were generated assuming Nyquist sampling and a velocity bandwidth of 50 m/s.

Figure 3-6 shows that estimation error increases with increasing spectral width. In addition, estimation error is higher for the shorter pulse length case since the shorter range gate interval contains fewer signal samples. Minimum "reasonable" signal-to-noise ratios are in the vicinity of 0 to +5 dB for the short pulse length case and -5 to 0 dB for the long pulse length case. Since the Cramer-Rao error is a lower bound, we will use the more pessimistic values of 5 dB and 0 dB for the short and long pulse length cases, respectively. At these signal-to-noise ratios, the optimum width estimators are within 50% of the true width for velocity widths below 15 m/s. Thus, signals below 0 dB in wideband power signal-to-noise ratio are not very useful for wake detection using the spectral width method.

3.5. Molecular Absorption Effects

Three runs of the computer program FASCODE were made to estimate the magnitude of molecular absorption in the atmosphere at the three laser wavelengths. The geometry used was chosen to give a worst case scenario to see if molecular absorption was a factor or not. The program computed the one-way transmission over a 50 km long path from an initial height of 12.2 km (40,000 ft) to a final height of 7.62 km (25,000 ft). The resulting look angle was about 5 degrees down. Table 3-4 lists the resulting one- and two-way transmissions. As Table 3-4 clearly shows, molecular absorption along the beam path is negligible for this analysis.

Table 3-4: Atmospheric Transmission due to Molecular Absorption for a
50 km Path from 12.2 km to 7.62 km Altitude

Wavelength	Transmission	
	One-way	Two-way
1.064 μm	0.9994	0.9987
2.091 μm	0.9906	0.9813
9.115 μm	0.9934	0.9868

4. Atmospheric Aerosols

In this chapter, we will try to see what effect atmospheric aerosols have on the performance of a Doppler lidar wake detection system. Atmospheric aerosols, at least in this report, refer to naturally occurring aerosol particles. Dense aerosol regions, such as clouds, will not be analyzed since it is assumed that lidar beams cannot probe very far into them. We will assume a cloud-free line of sight (CFLOS).

This chapter is broken down into three main subsections. In the first subsection, the vertical structure of aerosols in the atmosphere will be described. In the second subsection, models of aerosol backscatter and extinction coefficients will be presented for use as test cases. Finally, in the third subsection, signal-to-noise ratio will be analyzed for these model atmospheres. Wake detectability assuming scattering from atmospheric aerosols alone will be assessed.

4.1. Vertical Aerosol Structure

The atmosphere consists of several well defined altitude regions, each with its own unique properties. Below 30 km in altitude, these regions include the boundary layer, the free troposphere, and the stratosphere. Each region is described below.

4.1.1. Boundary Layer

The boundary layer is the lower part of the troposphere and exists from the earth's surface up to around 2 km in height. The salient feature of the boundary layer is a very high aerosol content (the haze we see as we look toward the horizon). In addition, the boundary layer aerosols tend to be larger than aerosols at higher altitudes (heavier particles sink). Thus, backscatter and attenuation in the boundary layer are generally very high. Boundary layer aerosol type depends largely on geographic location.

For this study, boundary layer aerosols are not very important since we are only interested in detecting aircraft at cruise altitudes.

4.1.2. Free Troposphere

The free troposphere is the upper portion of the troposphere and extends from the top of the boundary layer to the tropopause, which separates the troposphere from the stratosphere. Tropopause height varies both seasonally and geographically, but is generally between 8-17 km. Mean tropopause height is highest at latitudes near the equator and lowest at latitudes near the poles. Daily variations in tropopause height often exceed seasonal variations (Brown and Kunkel, 1985:16-46). Aerosol concentrations in the free troposphere decrease rapidly from the boundary layer up to the tropopause. In contrast to the boundary layer, the tropopause is cleanest part of the lower atmosphere and thus exhibits relatively low backscatter. Aerosols in the free troposphere generally consist of water soluble particles (ammonium and calcium sulfate and organic compounds) and dust-like particles (Fenn et al., 1985:18-12).

Aerosol concentration and type in the free troposphere are of great importance in this study since many aircraft cruise at these altitudes. Since this is typically the most aerosol-free layer in the lower atmosphere, it is expected that wake detection here will be the most difficult.

4.1.3. Stratosphere

Above the troposphere lies the stratosphere. The stratosphere extends from the top of the tropopause up to around 45 km in altitude. For this analysis, we are only interested in altitudes up to about 20 km (roughly 60,000 ft), which is the limit of most aircraft. The majority of aerosols in the stratosphere are of volcanic origin. During times of

increased volcanic activity, the stratosphere becomes heavily laden with volcanic debris and thus exhibits very high backscatter. Over time, these aerosols tend to fall out, and the stratosphere becomes slowly cleaner. There is some evidence that suggests that volcanic aerosols tend to filter out only at the higher latitudes near the earth's poles since tropical and mid-latitude tropopause appear to remain very clean despite high volcanic loading in the stratosphere (Kent et al., 1986:2-31).

Most military aircraft are capable of flying at stratospheric altitudes. For this reason, the stratosphere is an important region in this study. Since stratospheric aerosol loading can vary a great deal depending on recent volcanic activity, it is expected that wake detectability in the stratosphere will also vary greatly.

4.2. Backscatter and Extinction

The general atmospheric structure described above is fairly well known. The problem is in quantifying what the backscatter and extinction levels are for a given wavelength of light, at a given altitude, at a given geographic location, and during a given season. Furthermore, we would like to know how much variability exists in these levels and how often they occur. Unfortunately, a complete statistical model of global backscatter and extinction does not exist. Adequate models of mean aerosol characteristics are available and they will be described below.

Using these aerosol models, three test atmospheres were developed to evaluate lidar performance under a wide range of atmospheric aerosol conditions. In this analysis, the atmosphere is assumed to be horizontally homogeneous; that is, backscatter and extinction are constant at any given altitude.

Finally, absorption of laser light by atmospheric gas molecules must not be overlooked. The results of computer analyses for the three wavelengths of interest are presented.

4.2.1. Geophysics Laboratory Aerosol Models

The Air Force's Geophysics Laboratory has developed an extensive set of atmospheric aerosol models (Fenn et al., 1985:section 18-2). The models consist of particle size distributions for several types of aerosol in the boundary layer, free troposphere, and stratosphere. The size distributions for each aerosol type are based on experimental measurements by many researchers and assume spherical particles. Optical scattering and absorption parameters are calculated from these models using Mie scattering theory. Variations in the aerosol characteristics due to humidity, visibility, geographic location, season, and volcanic activity are included in the models.

The Geophysics Laboratory aerosol models have been implemented on a computer program called BACKSCAT that simulates lidar backscatter for a wide range of wavelengths from 0.20 to 40.0 μm (Guivens et al., 1988). BACKSCAT runs on an IBM-PC type computer and computes backscattered power versus range for any given lidar system and atmospheric model. In addition, the program generates altitude profiles of aerosol and molecular backscatter and extinction.

While these models do give mean backscatter and extinction levels for different atmospheres, they do not indicate how much variability may occur in the levels. Furthermore, the models are based on assumed size distributions and aerosol types and not on actual lidar measurements. As discussed later, some limited validation of the models, at least at 0.5 μm and 10.6 μm , indicates good correlation with lidar data (Koenig,

1990). Though not ideal, the Geophysics Laboratory aerosol models appear to be one of the most extensive available and so will be used in this study to generate model atmospheres to use as test cases.

4.2.2. Model Atmospheres for Calculations

BACKSCAT was used to generate three model atmospheres for use as test cases to compute signal-to-noise ratio. The three test cases represent atmospheres with a wide range of aerosol loading from very clean to very dirty air. The atmospheric models consist of altitude profiles of backscatter and extinction coefficients from both aerosols and molecules at the three infrared wavelengths of interest. In all cases, the tropopause height was 9 km, the top of the stratosphere was at 29 km, and the top of the boundary layer was at 2 km. These values were fixed by BACKSCAT. Hopefully, future upgrades to this program will allow layer heights to be changed.

The molecular backscatter and total scattering coefficients were computed by BACKSCAT using the Rayleigh scattering theory presented in chapter 2. These parameters do not change with varying aerosol models. Molecular backscatter coefficients for the three wavelengths are shown in Figure 4-1.a and total scattering coefficients are shown in Figure 4-1.b. For negligibly small molecular absorption, the total molecular scattering coefficients are also the molecular extinction coefficients.

The clean atmosphere was developed to give the lowest possible backscatter and extinction values at all altitudes. The boundary layer model used was the rural aerosol model at 0% humidity and 50 km visibility. The tropospheric model also used 0% relative humidity. For the stratosphere, the background fall/winter model was implemented, which assumed almost no volcanic aerosol loading. Figure 4-2.a shows the

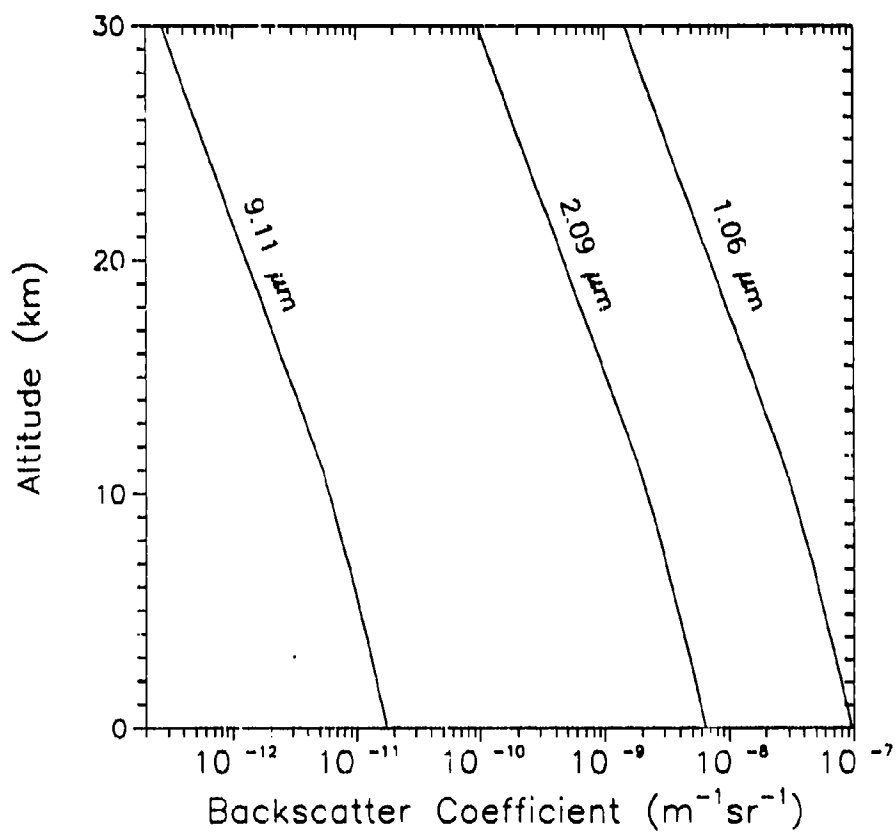


Figure 4-1.a. Molecular Backscatter Coefficient Profiles

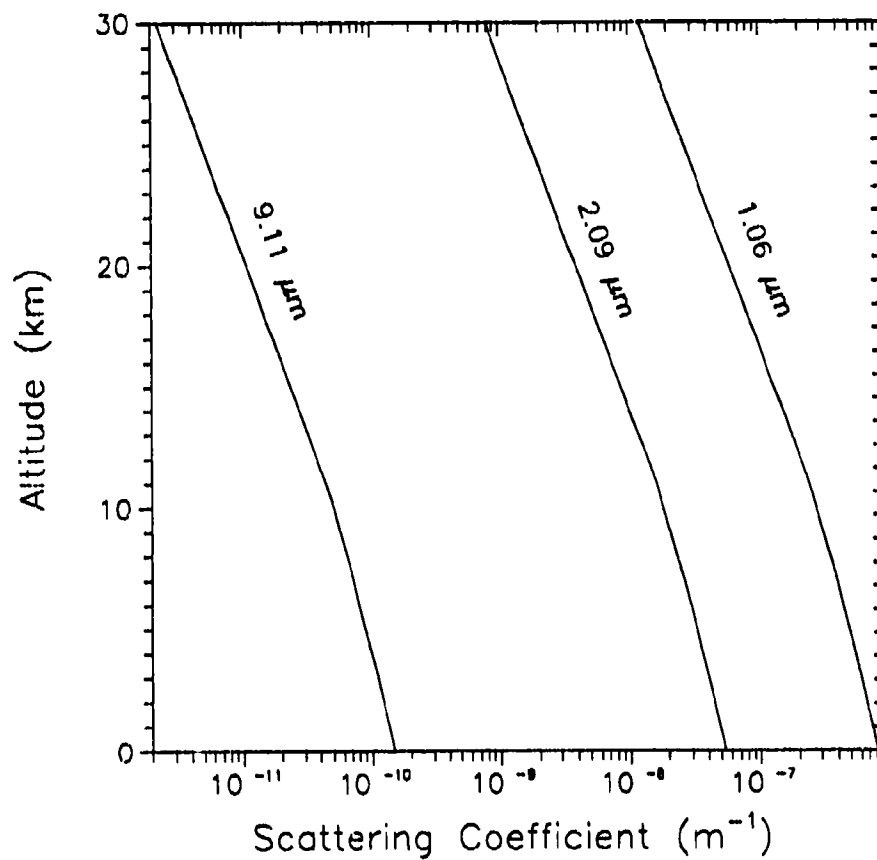


Figure 4-1.b. Total Molecular Scattering Coefficient Profiles

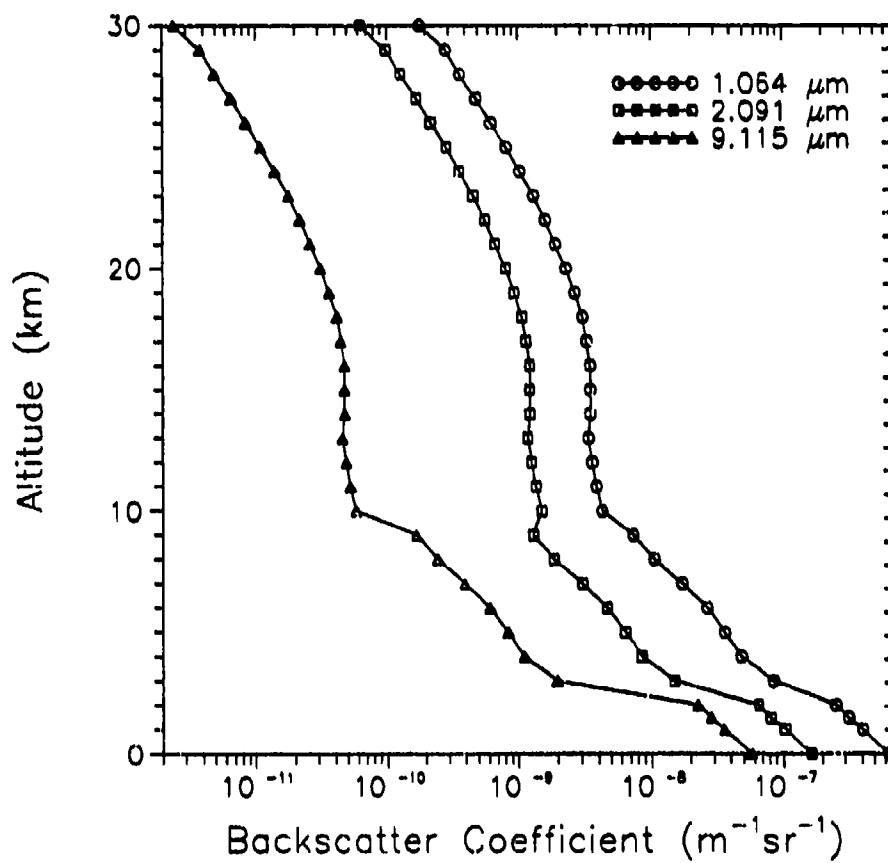


Figure 4-2.a. Aerosol Backscatter Coefficient Profile for the Clean Atmosphere Model

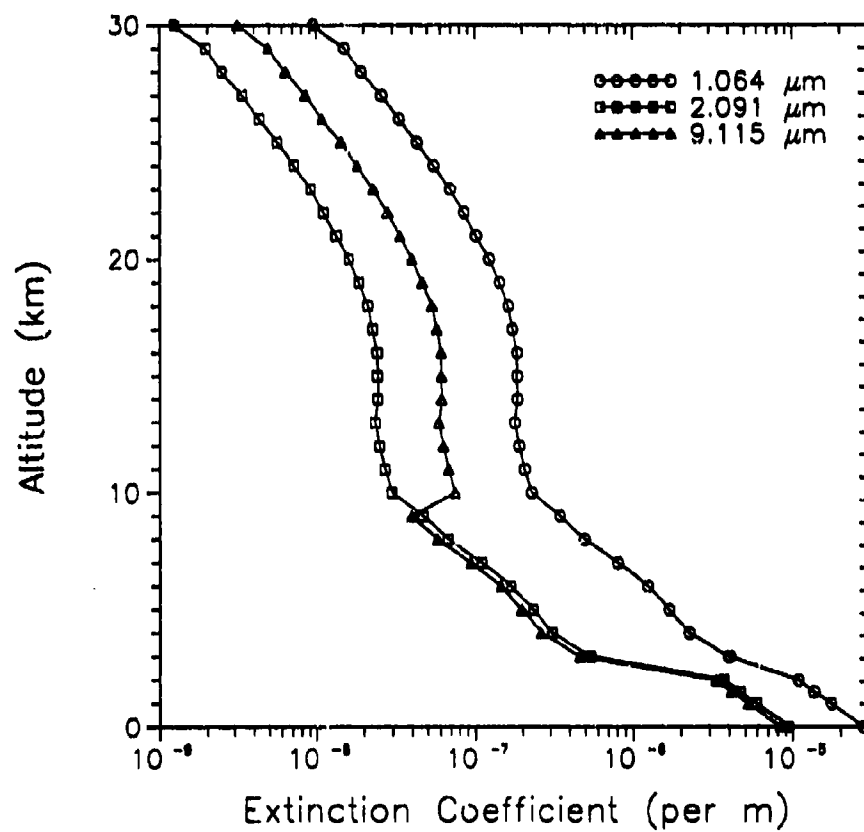


Figure 4-2.b. Aerosol Extinction Coefficient Profile for the Clean Atmosphere Model

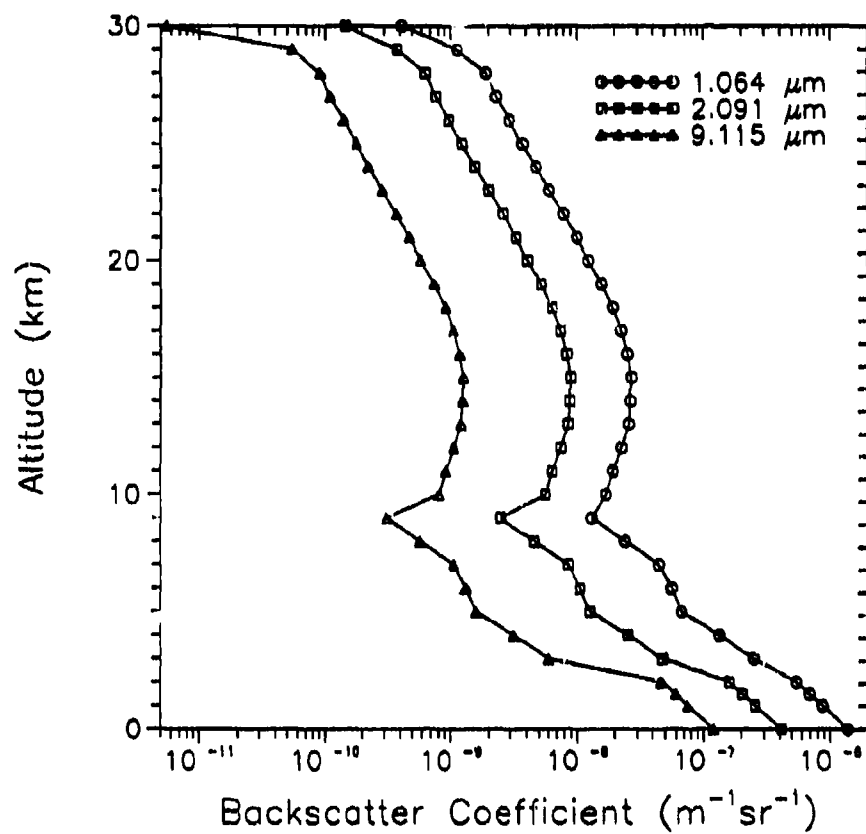


Figure 4-3.a. Aerosol Backscatter Coefficient Profile for the Moderate Atmosphere Model

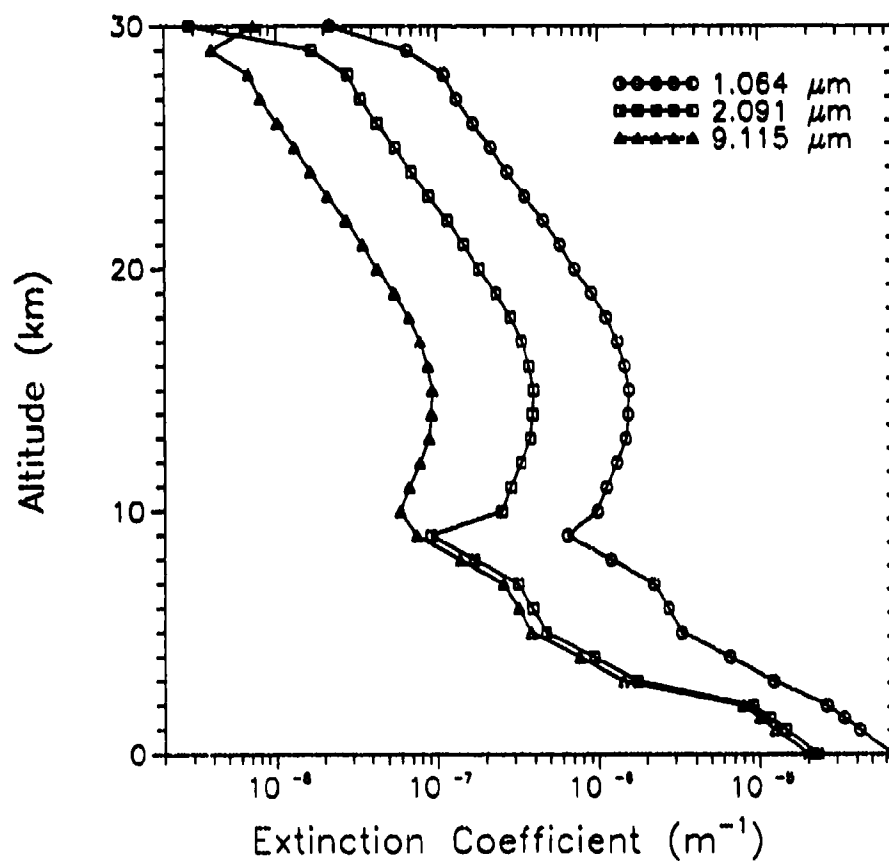


Figure 4.3.b. Aerosol Extinction Coefficient Profile for the Moderate Atmosphere Model

resulting aerosol backscatter coefficient profiles and Figure 4-2.b shows the aerosol extinction coefficient profiles for the clean atmosphere.

The moderate atmosphere was developed to give backscatter values roughly halfway between the clean and dirty atmospheres. In no way, however, does this imply that the moderate atmosphere is representative of statistical average or most probable backscatter levels. The boundary layer model used was a rural aerosol model at 70% relative humidity and 23 km visibility. The tropospheric humidity was also set at 70%, and the stratospheric model used was the spring/summer aged-moderate volcanic model. The aged volcanic model assumes that enough time has elapsed since injection that the larger volcanic particles have settled out. The moderate volcanic model relates to the total particle number density. Figure 4-3.a shows the resulting aerosol backscatter coefficient profiles for the moderate atmosphere. Figure 4-3.b shows the resulting aerosol extinction coefficient profiles.

The dirty atmosphere model was developed to give the highest possible backscatter values over all altitudes. The boundary layer model used for the dirty atmosphere was the urban aerosol model at 99% relative humidity and 2 km visibility. In the troposphere, relative humidity was also set to 99%. The stratospheric model used the spring/summer fresh-extreme volcanic aerosol model. The fresh volcanic model assumes a recent eruption, resulting in a lot of large particles. Figures 4-4.a-b show the aerosol backscatter and extinction coefficient profiles of the dirty atmosphere model.

In the three atmosphere models above, it is apparent that the backscatter coefficients for the shorter wavelengths are higher than those for the longer wavelengths. Also note that molecular backscatter is very significant at 1.064 μm compared to aerosol backscatter, but it is completely negligible at 9.115 μm . From clean atmosphere to dirty

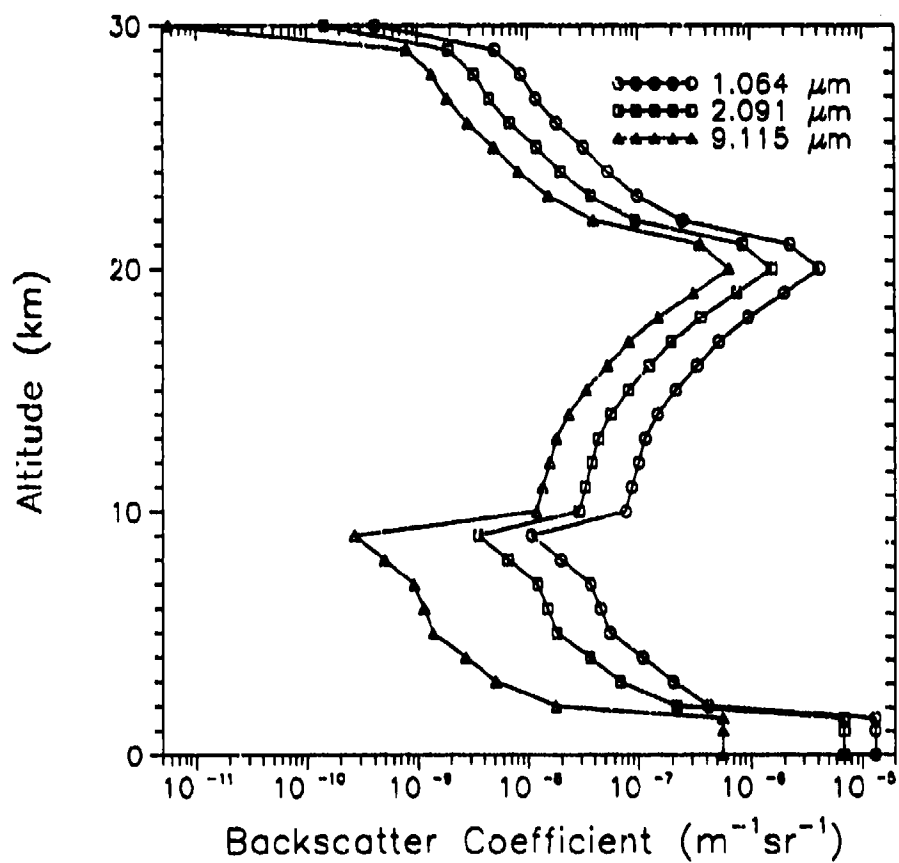


Figure 4-4.a. Aerosol Backscatter Coefficient Profile for the Dirty Atmosphere Model

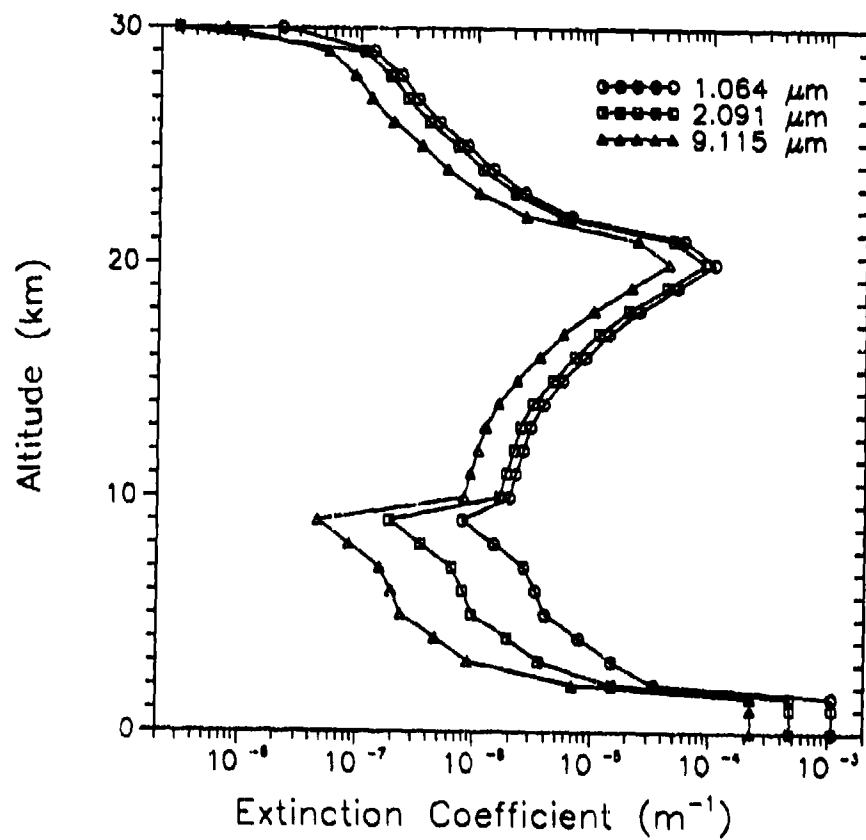


Figure 4-4.b. Aerosol Extinction Coefficient Profile for the Dirty Atmosphere Model

atmosphere, backscatter in the free troposphere changes very little, while backscatter in the stratosphere changes 3-4 orders of magnitude! Boundary layer backscatter varies by about an order of magnitude from clean to dirty.

4.2.3. Comparison with Measured Aerosol Data

The three models of atmospheric aerosol backscatter and extinction were compared to measured data for validation. Unfortunately, no usable lidar data was found for the 1.064 and 2.091 μm cases; however, some published 1 μm extinction data from the SAGE I satellite was located for comparison. Figure 4-5 shows two SAGE I extinction coefficient profiles. One profile, taken between September-November 1979, represents a relatively clean atmosphere, free of volcanic aerosols (Kent et al., 1986:2-17). The second profile, taken between June-August 1980, shows the effects of the eruption of Mount St. Helens (Kent et al., 1986:2-29). Both profiles were taken between 20°-40° north latitude.

The extinction data in Figure 4-5 compares well with the clean and moderate atmosphere models; however, the dirty atmosphere model shows much more volcanic enhancement than the SAGE I data following the eruption of Mount St. Helens. For this reason, the 1.064 μm dirty atmosphere model should be taken as an absolute extreme case.

A fair amount of published 10.6 μm lidar data exists, which was used for comparison with the 9.115 μm models. Backscatter coefficients in the clean atmosphere model compare quite well with 10.6 μm lidar data measured in the northern hemisphere. Rothermel et al. (1989) report "a high frequency of occurrence for a narrow range of low backscatter values in the troposphere - a background mode." At altitudes between 9-12 km, the background backscatter coefficient is roughly $3 \times 10^{-11} \text{ m}^{-1} \text{sr}^{-1}$ (Rothermel, et al., 1989:1041). The clean atmosphere model developed

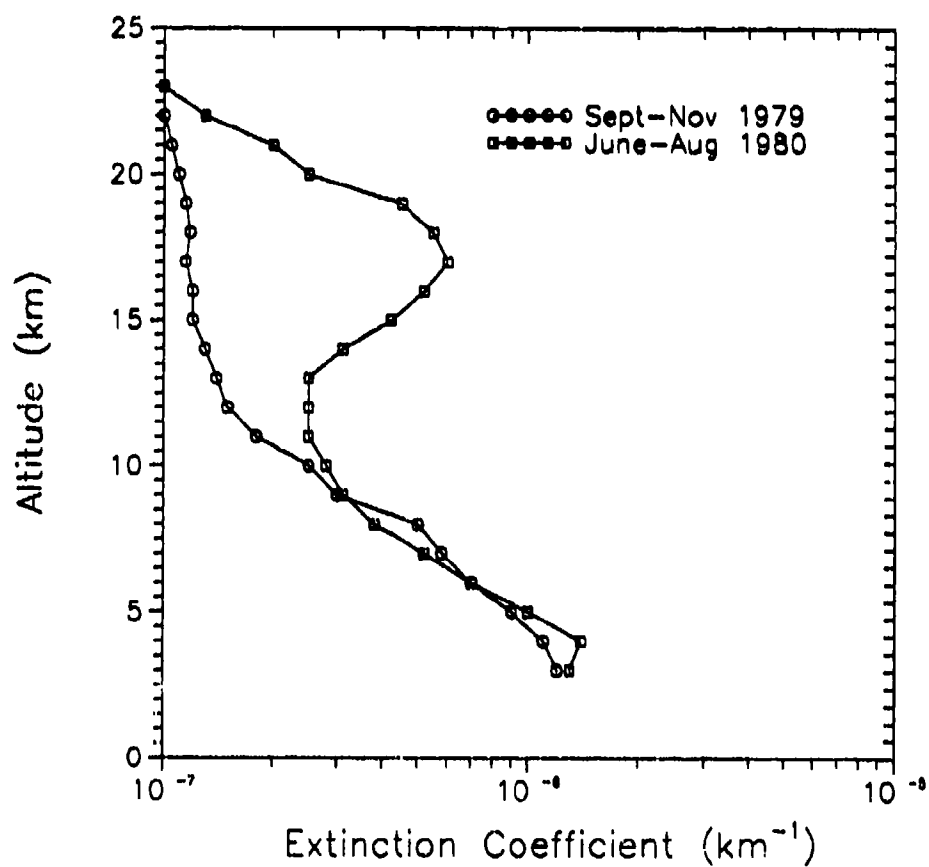


Figure 4-5. 1 μ m Aerosol Extinction Coefficient Profiles from SAGE I Satellite Data for Both Clean and High Volcanic Periods

above indicates backscatter coefficients around $5-6 \times 10^{-11} \text{ m}^{-1} \text{sr}^{-1}$ at these altitudes. The small difference may be attributed to the expected higher backscatter at 9μ (Ancellet et al., 1988).

Volcanic enhancement at $9.115 \mu\text{m}$ was also compared to $10.6 \mu\text{m}$ lidar data. Post (1984) reports an increase in backscatter between about 18-23 km altitude over Boulder, CO following the eruption of El Chichon in Mexico in 1982. Peak volcanic backscatter coefficient was $8 \times 10^{-9} \text{ m}^{-1} \text{sr}^{-1}$, which was about an order of magnitude above ambient levels before the eruption (Post, 1984:2509). This level of volcanic backscatter enhancement is a factor of 8 above the $1 \times 10^{-9} \text{ m}^{-1} \text{sr}^{-1}$ level shown in the moderate atmosphere model but is almost two orders of magnitude below the $7 \times 10^{-7} \text{ m}^{-1} \text{sr}^{-1}$ level shown in the dirty atmosphere model. Again, volcanic enhancement in the dirty atmosphere model appears to be at least an order of magnitude too extreme.

The clean and moderate atmosphere models compare well with measured data at 1 and $10 \mu\text{m}$. Stratospheric backscatter and extinction in the dirty atmosphere model are 1-2 orders of magnitude above published values. Results from this model, therefore, should be accepted as absolute extremes at best.

4.3. Performance Analysis

The results of signal-to-noise computations using the model atmospheres are presented below. An analysis of these results identifies implications for wake detectability from atmospheric aerosols alone.

4.3.1. Signal-to-Noise Ratio Computations

Signal-to-noise ratio was computed using the equations developed in chapter 2, the lidar system parameters given in chapter 3, and the test atmospheres developed in this chapter. Simulations were run for two different aircraft altitudes (lidar altitudes): 9 km (30 kft) and 13.7

km (45 kft). The 9 km altitude is in the tropopause. Signal-to-noise ratio was computed at each altitude for lidar beam angles from +6 degrees up to -6 degrees down in 2 degree increments. Range varied from 2 to 80 km in 2 km increments. Signal-to-noise ratio values presented here represent wideband signal-to-noise for a single laser pulse (no pulse integration).

For each scenario, the signal-to-noise ratio versus range curves for the 7 look angles were plotted. The data on these graphs was then converted to contour lines of constant signal level and plotted on graphs of altitude versus horizontal range. These graphs gave the clearest picture of which areas of the atmosphere the signal level was sufficient for wake detection. The resulting graphs are shown below in Figures 4-6 through 4-11. The cross hatched areas show where signal-to-noise ratio is above 1 (0 dB). Contours are cubic spline fits to the data points shown on the graphs.

4.3.2. Analysis of Results

The overall results for atmospheric aerosols alone are rather discouraging. In the clean atmosphere case, none of the lidars show any appreciable detection capability. Only the 9.115 μm lidar has areas where the signal-to-noise ratio exceeded 0 dB, and these are only at close range or at very low altitudes where aerosol loading was high. Furthermore, if we use the 5 dB minimum for short pulse lengths (see chapter 3), the situation is even worse. Overall, wake detection for the clean atmosphere case and the given lidar configurations is out of the question.

The results for the moderate atmosphere case are only slightly better. As before, the 1.064 μm and 2.091 μm lidars do not show any real wake detection capability. The 9.115 μm lidar does, however, have some rather large areas where signal-to-noise is over 0 dB. At 9 km

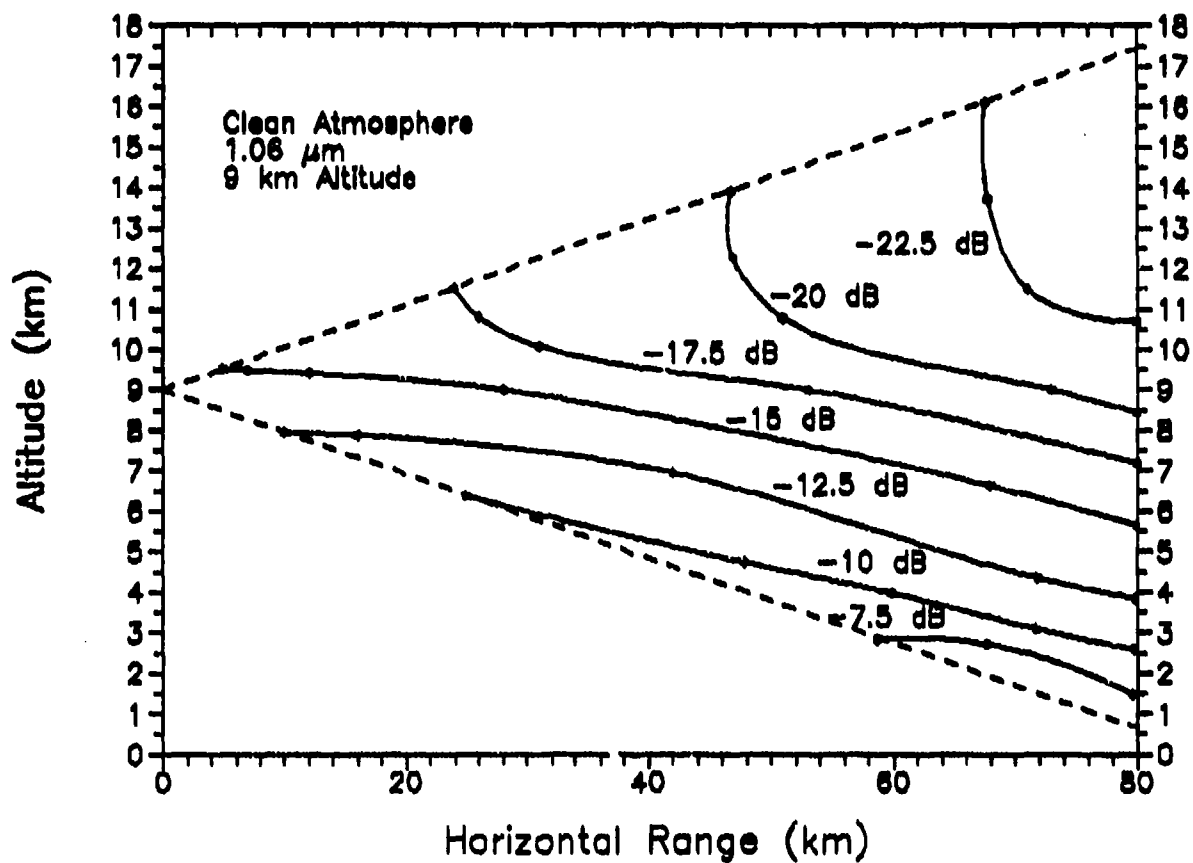


Figure 4-6.a. Signal-to-Noise Ratio for Clean Atmosphere, Aircraft at 9 km Altitude, and 1.064 μm

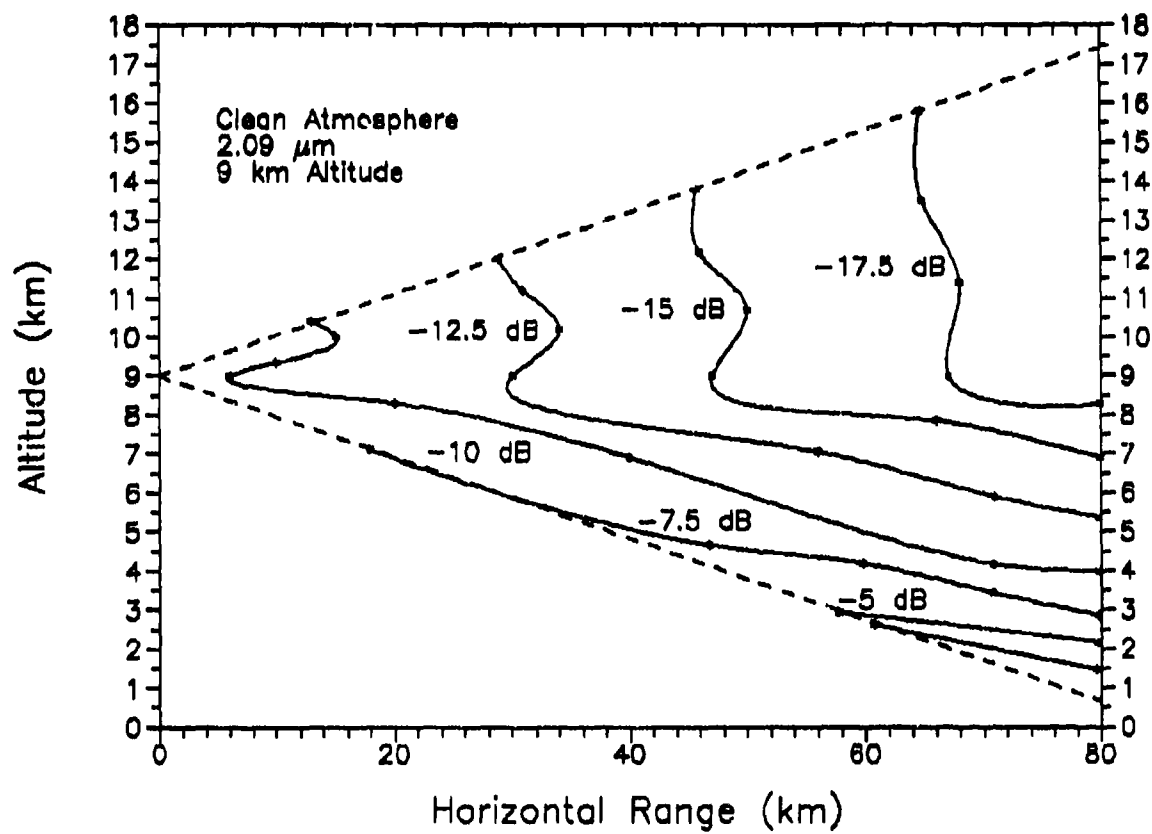


Figure 4-6.b. Signal-to-Noise Ratio for Clean Atmosphere, Aircraft at 9 km Altitude, and 2.091 μm

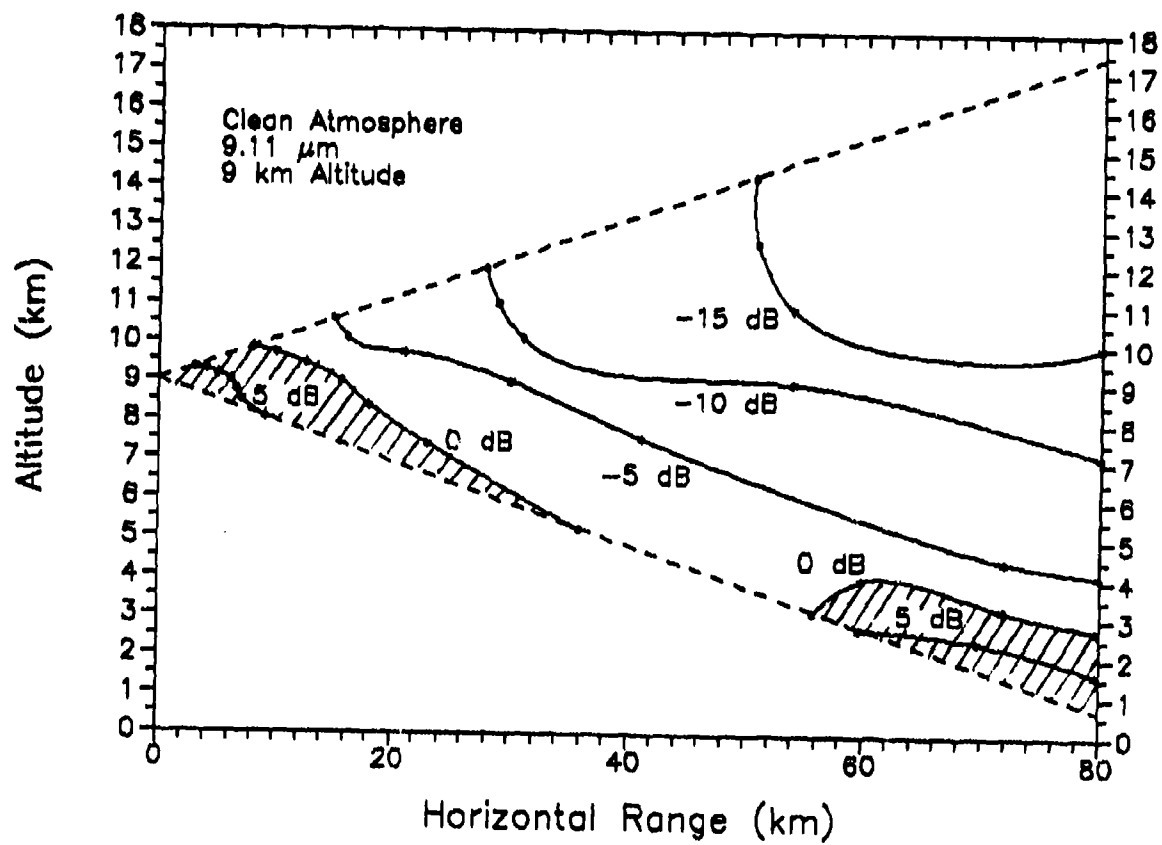


Figure 4-6.c. Signal-to-Noise Ratio for Clean Atmosphere, Aircraft at 9 km Altitude, and 9.115 μm

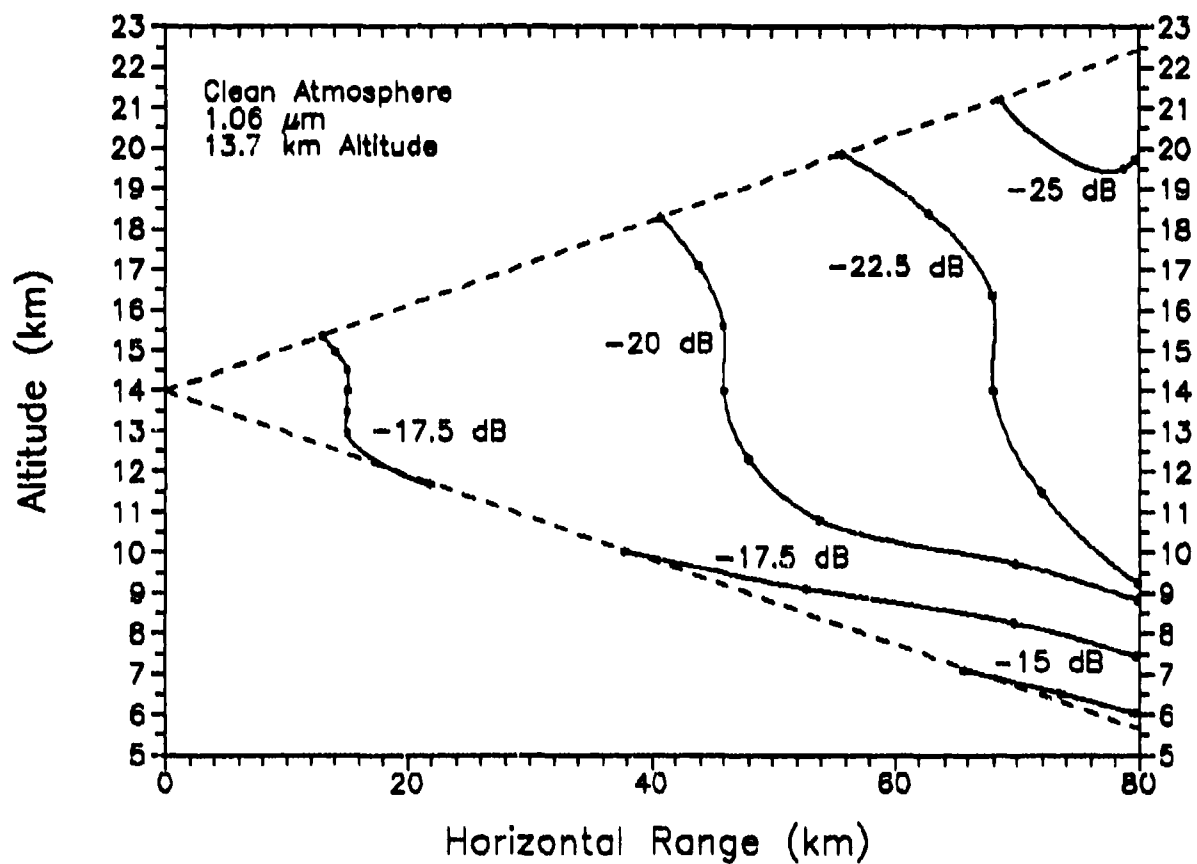


Figure 4-7.a. Signal-to-Noise Ratio for Clean Atmosphere, Aircraft at 13.7 km Altitude, and 1.064 μm

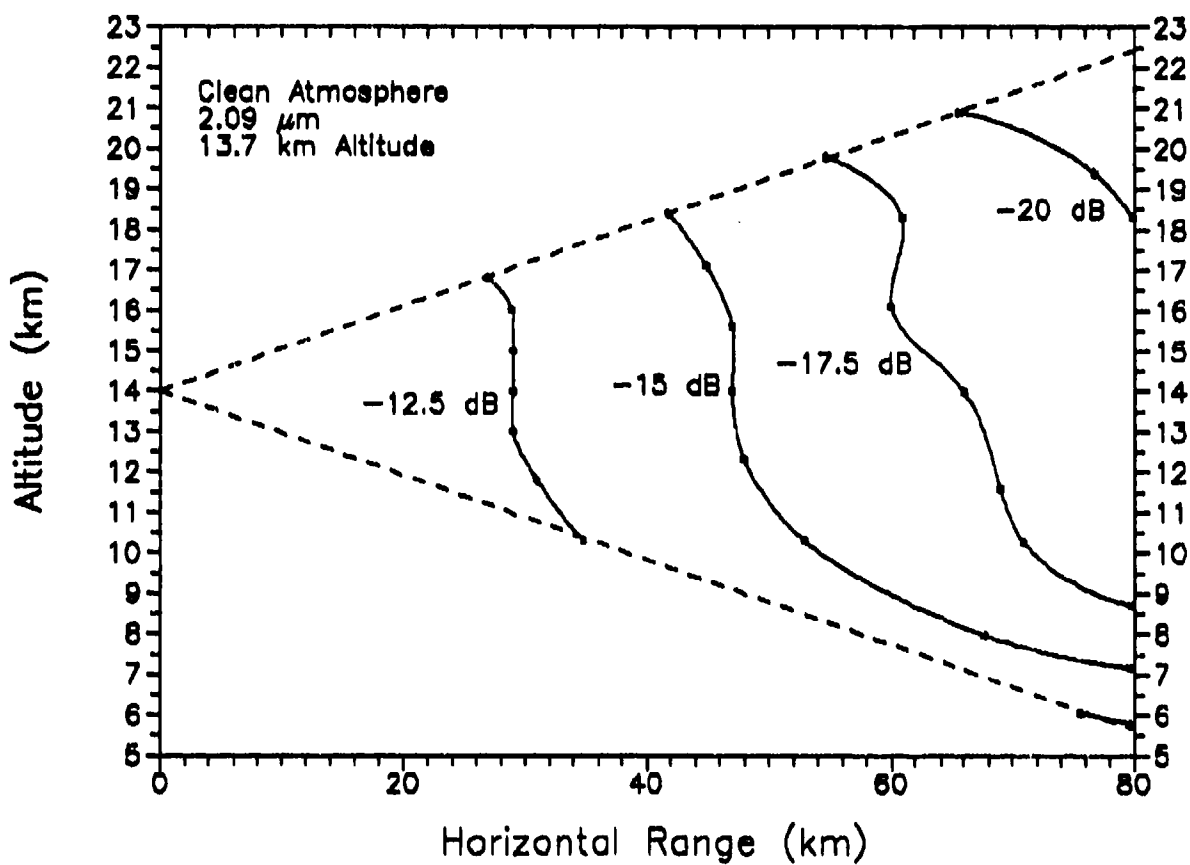


Figure 4-7.b. Signal-to-Noise Ratio for Clean Atmosphere, Aircraft at 13.7 km Altitude, and 2.091 μm

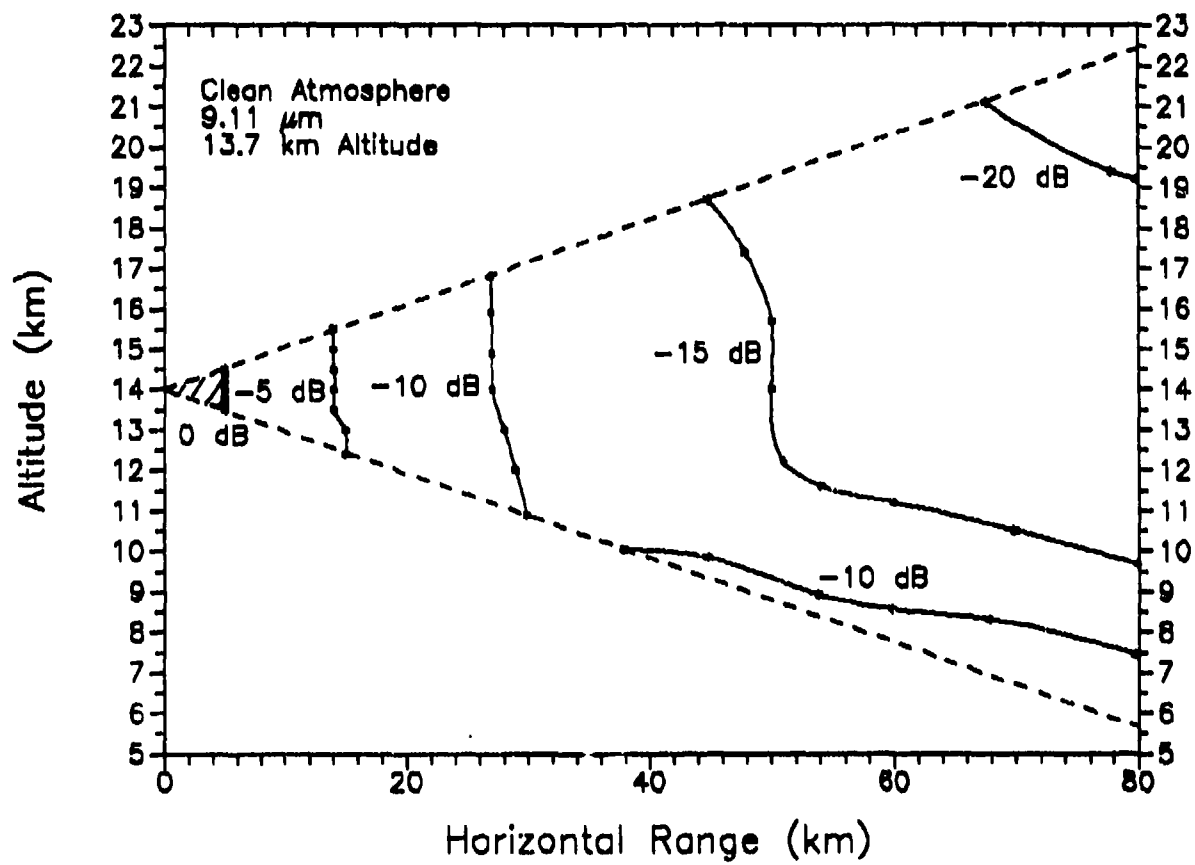


Figure 4-7.c. Signal-to-Noise Ratio for Clean Atmosphere, Aircraft at 13.7 km Altitude, and 9.115 μm

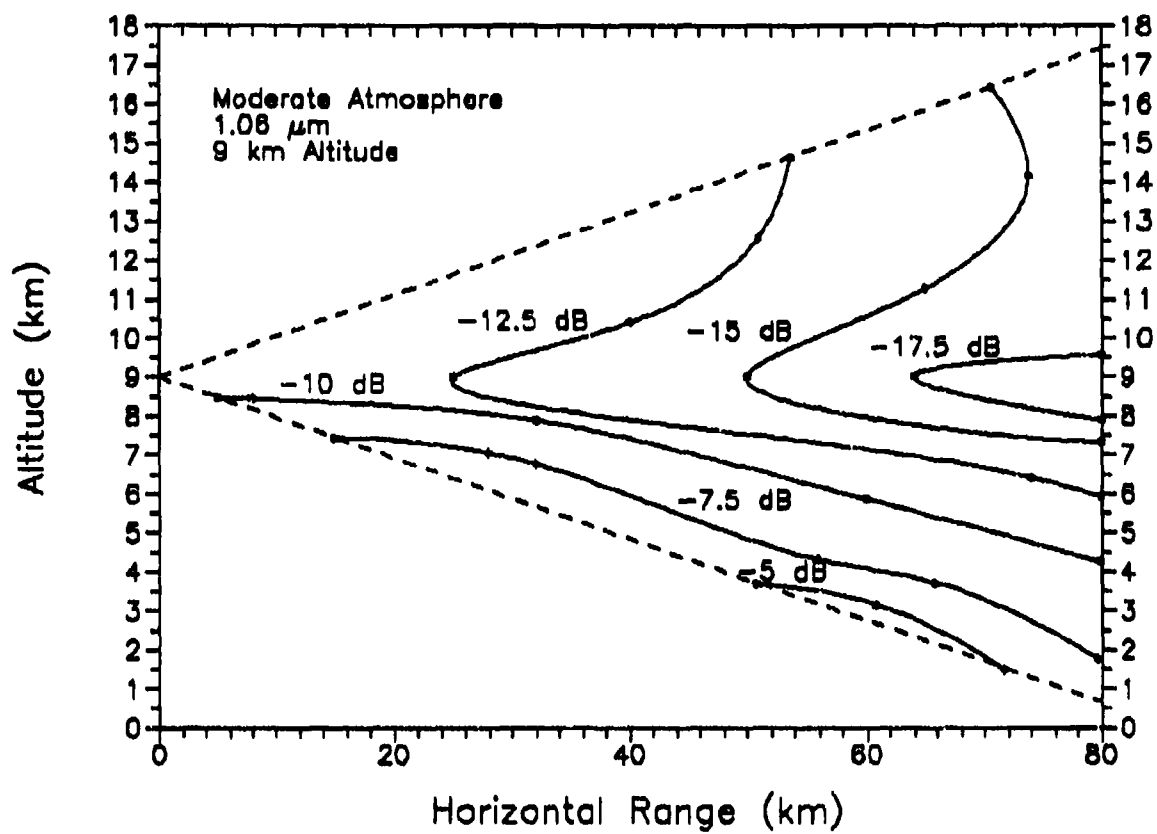


Figure 4-8.a. Signal-to-Noise Ratio for Moderate Atmosphere, Aircraft at 9 km Altitude, and 1.064 μm

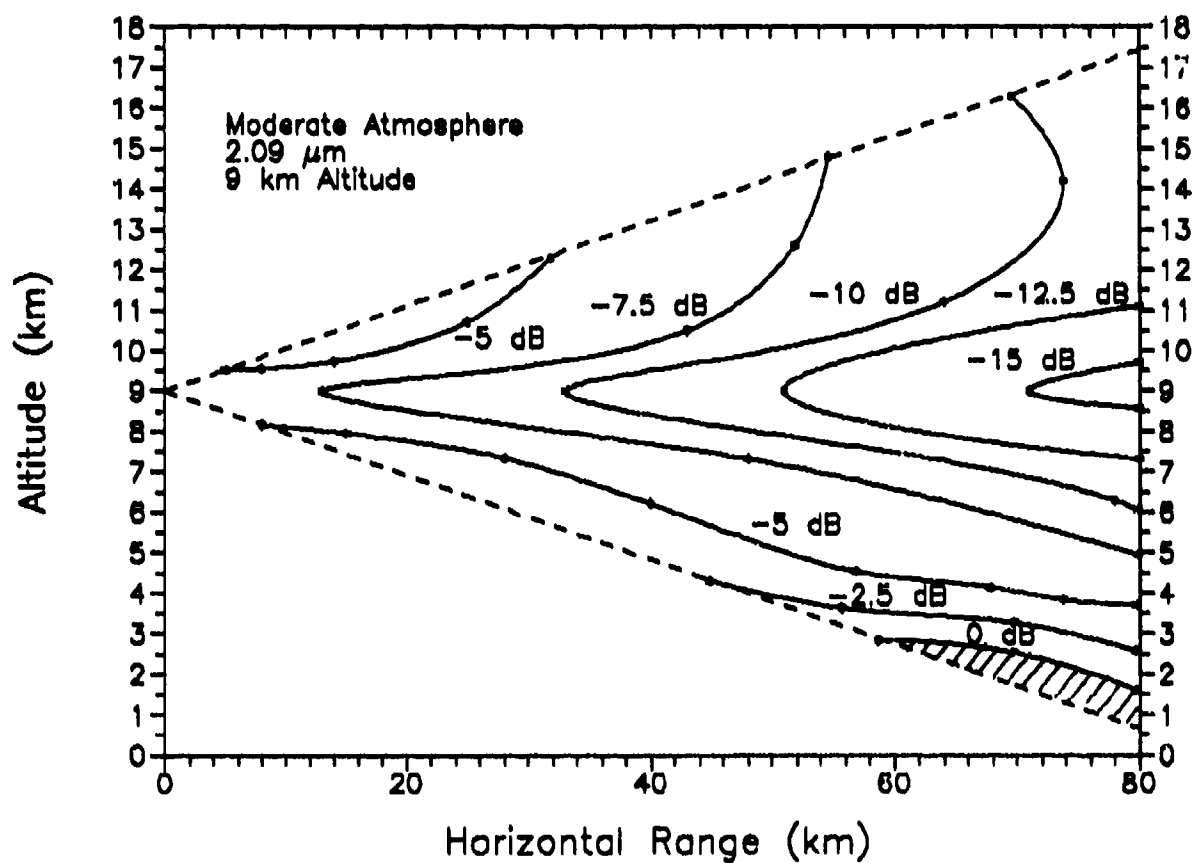


Figure 4-8.b. Signal-to-Noise Ratio for Moderate Atmosphere, Aircraft at 9 km Altitude, and $2.091 \mu\text{m}$

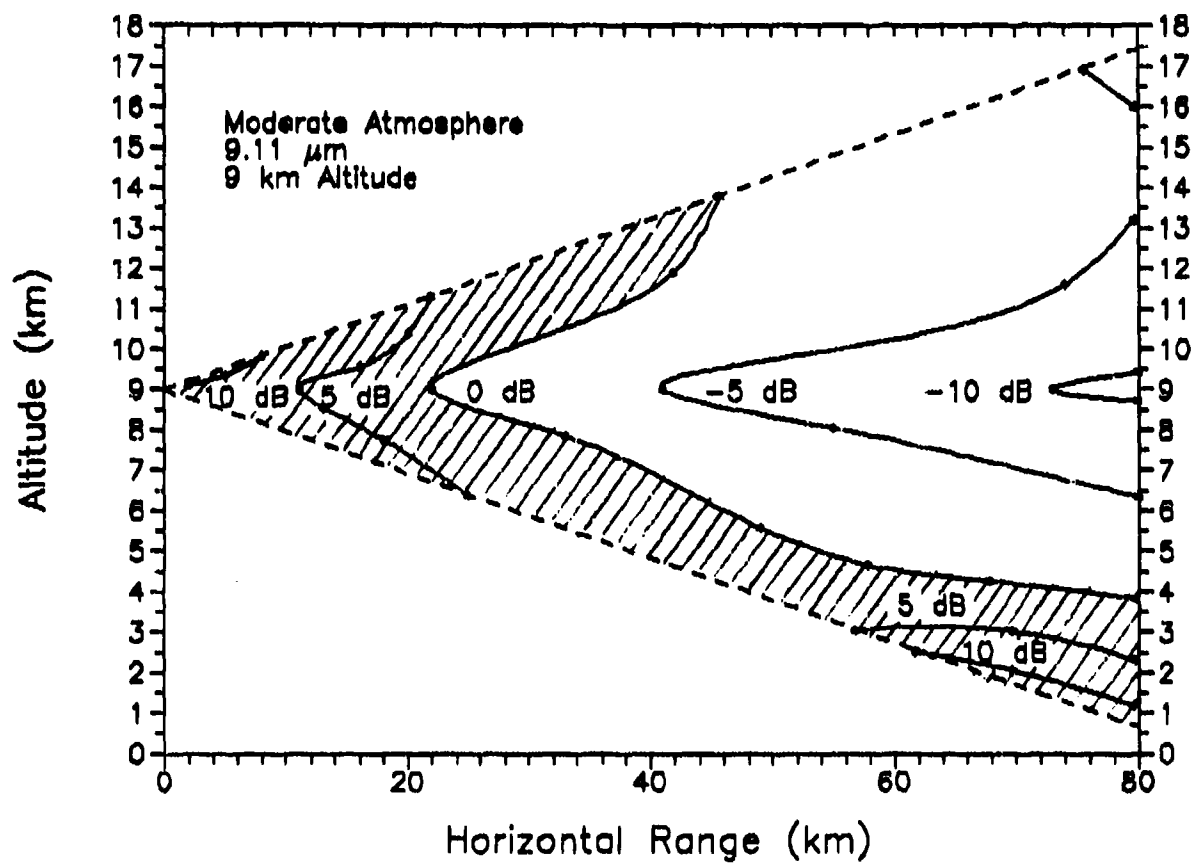


Figure 4-8.c. Signal-to-Noise Ratio for Moderate Atmosphere, Aircraft at 9 km Altitude, and 9.115 μm

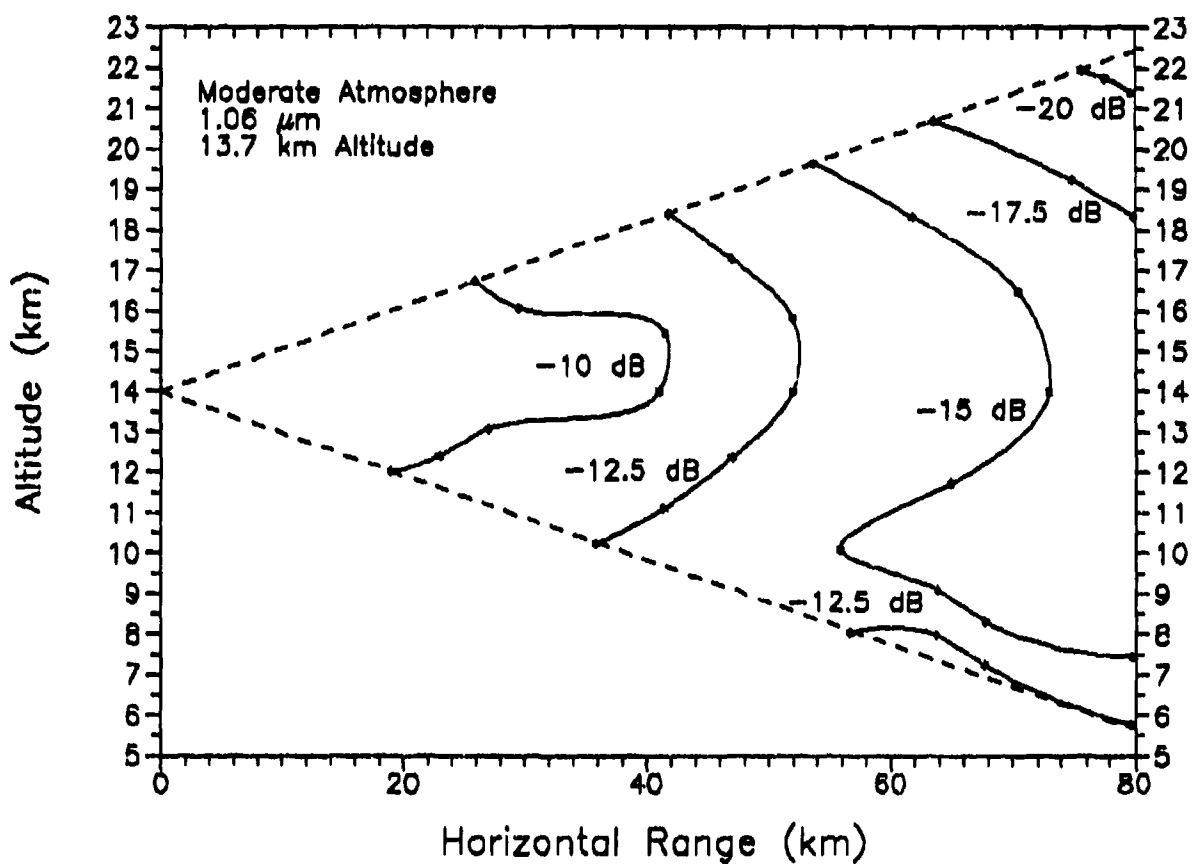


Figure 4-9.a. Signal-to-Noise Ratio for Moderate Atmosphere, Aircraft at 13.7 km Altitude, and 1.064 μm

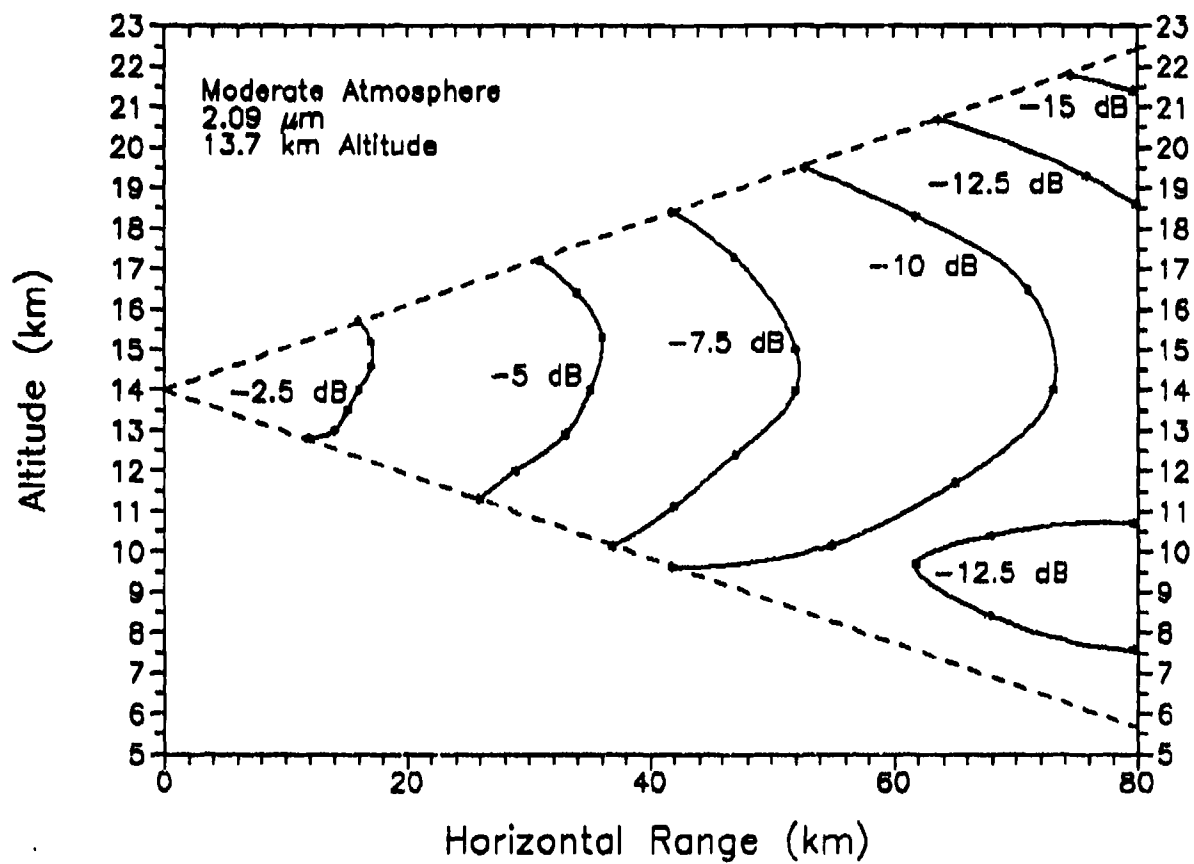


Figure 4-9.b. Signal-to-Noise Ratio for Moderate Atmosphere, Aircraft at 13.7 km Altitude, and 2.091 μm

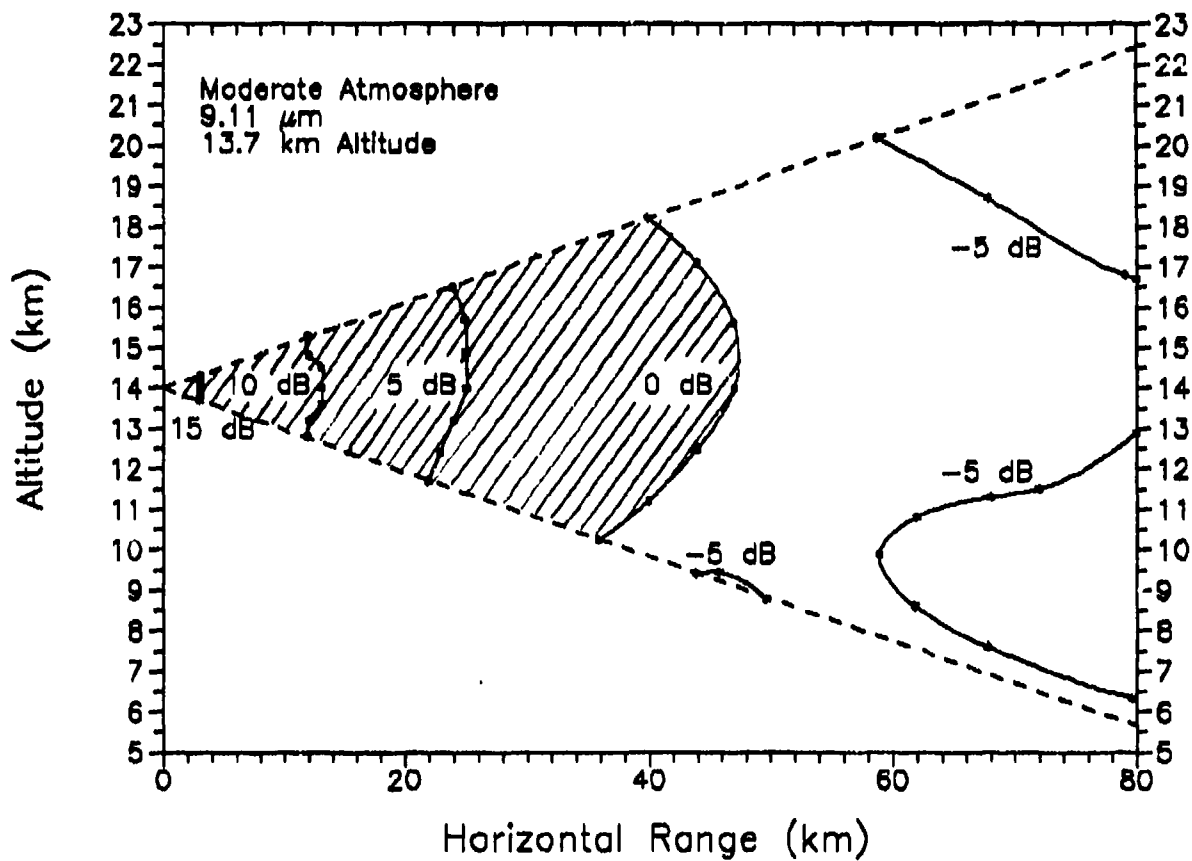


Figure 4-9.c. Signal-to-Noise Ratio for Moderate Atmosphere, Aircraft at 13.7 km Altitude, and 9.115 μm

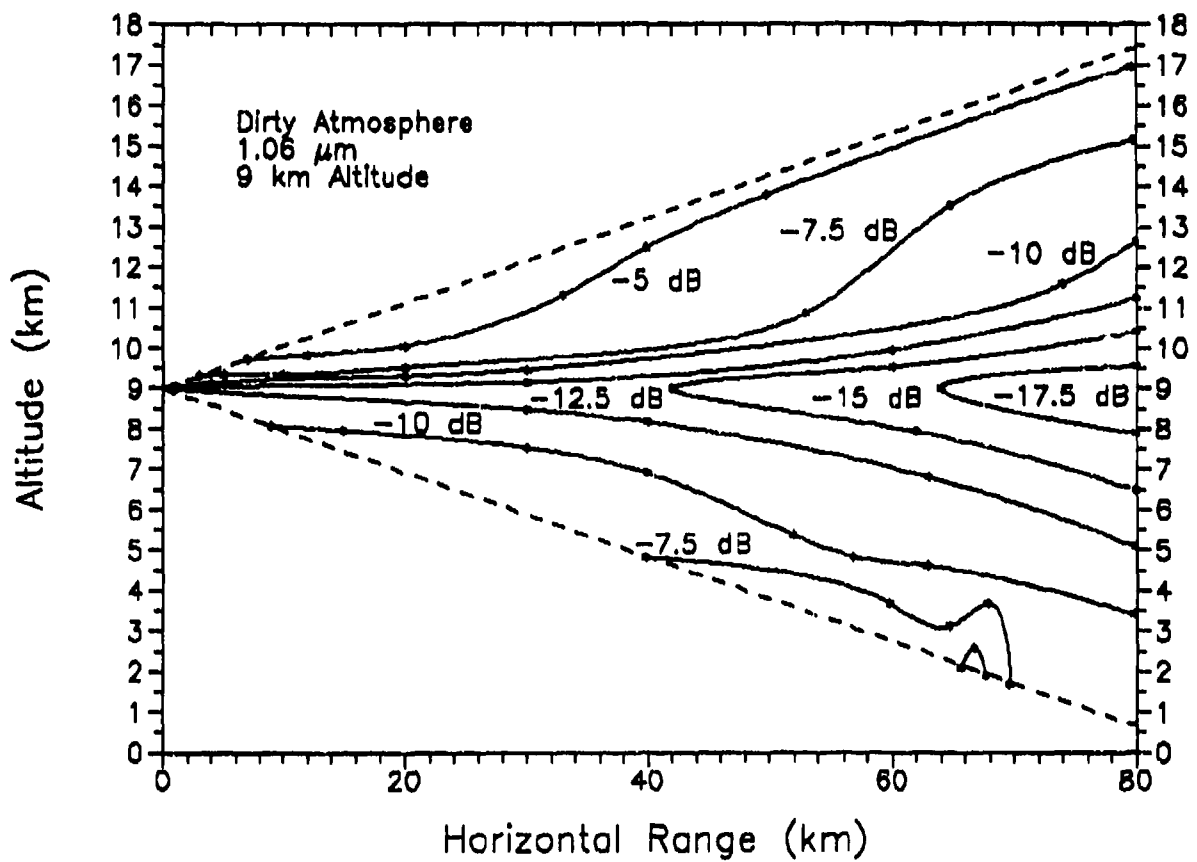


Figure 4-10.a. Signal-to-Noise Ratio for Dirty Atmosphere, Aircraft at 9 km Altitude, and 1.064 μm

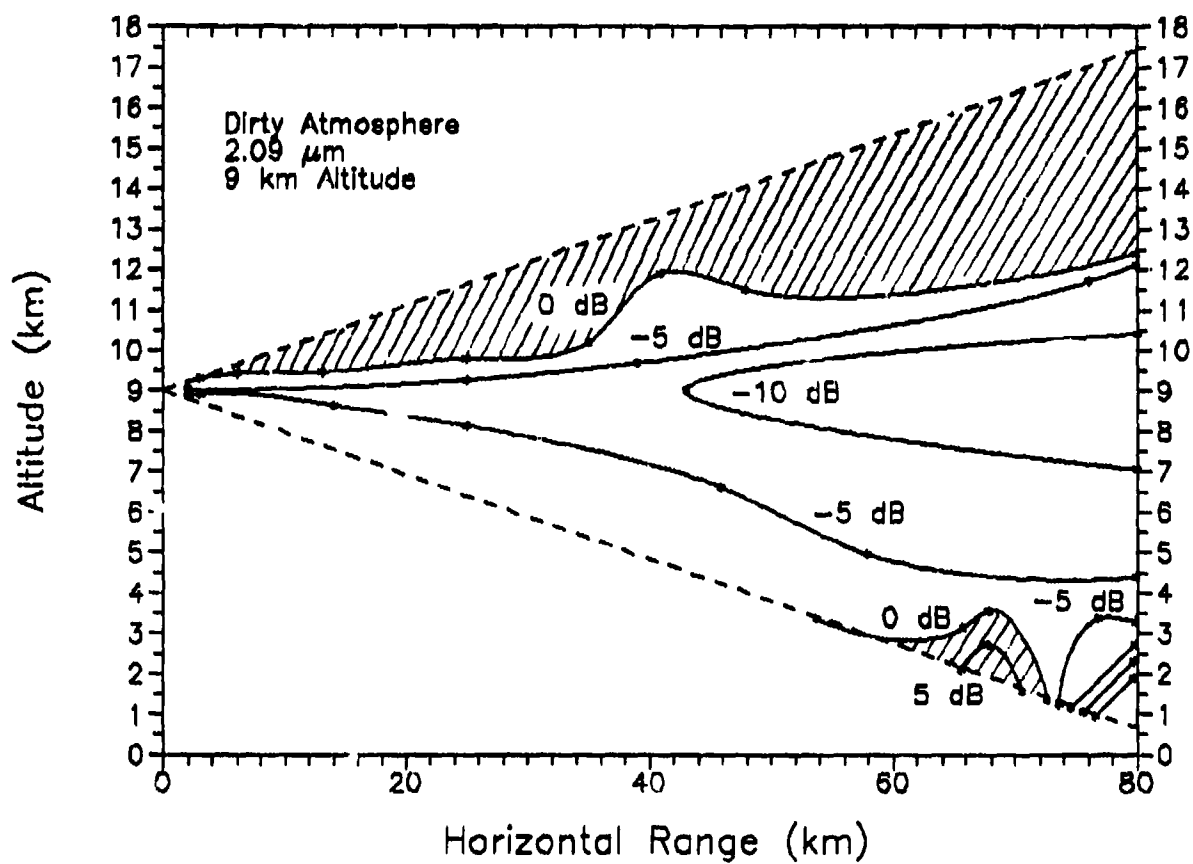


Figure 4-10.b. Signal-to-Noise Ratio for Dirty Atmosphere, Aircraft at 9 km Altitude, and 2.091 μm

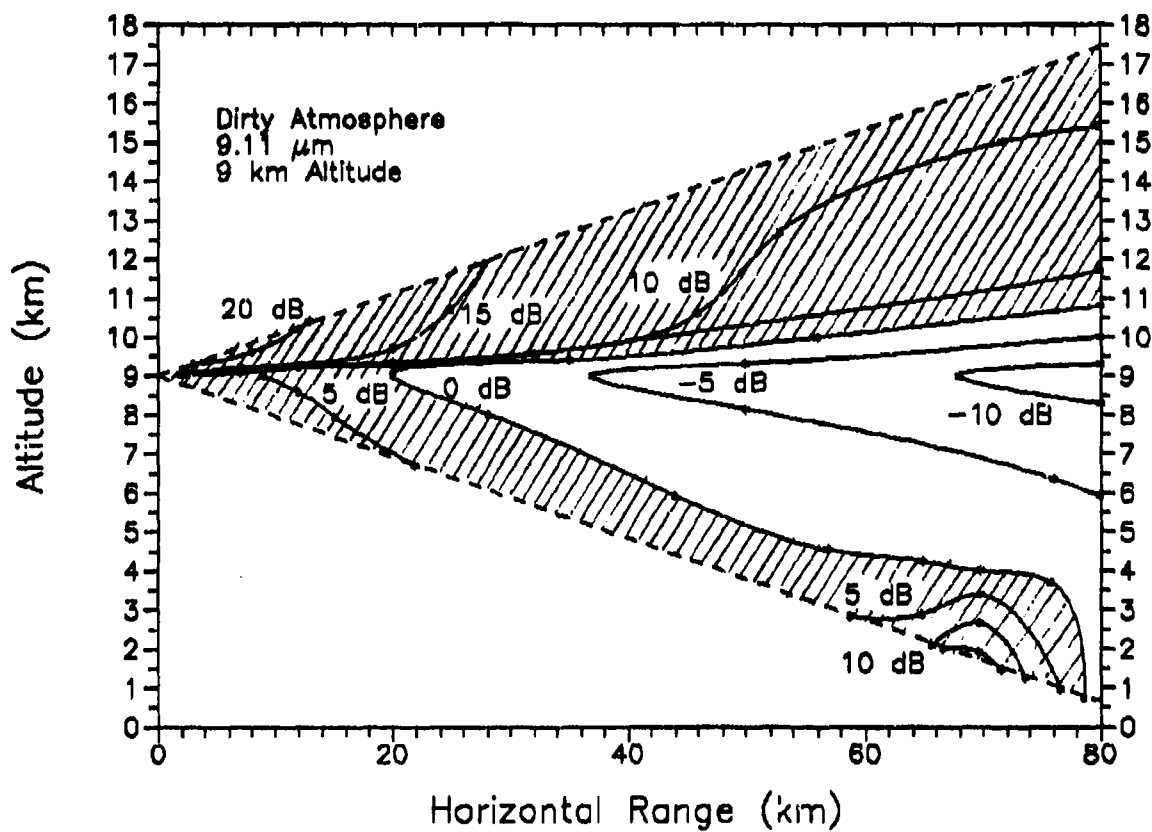


Figure 4-10.c. Signal-to-Noise Ratio for Dirty Atmosphere, Aircraft at 9 km Altitude, and $9.115 \mu\text{m}$

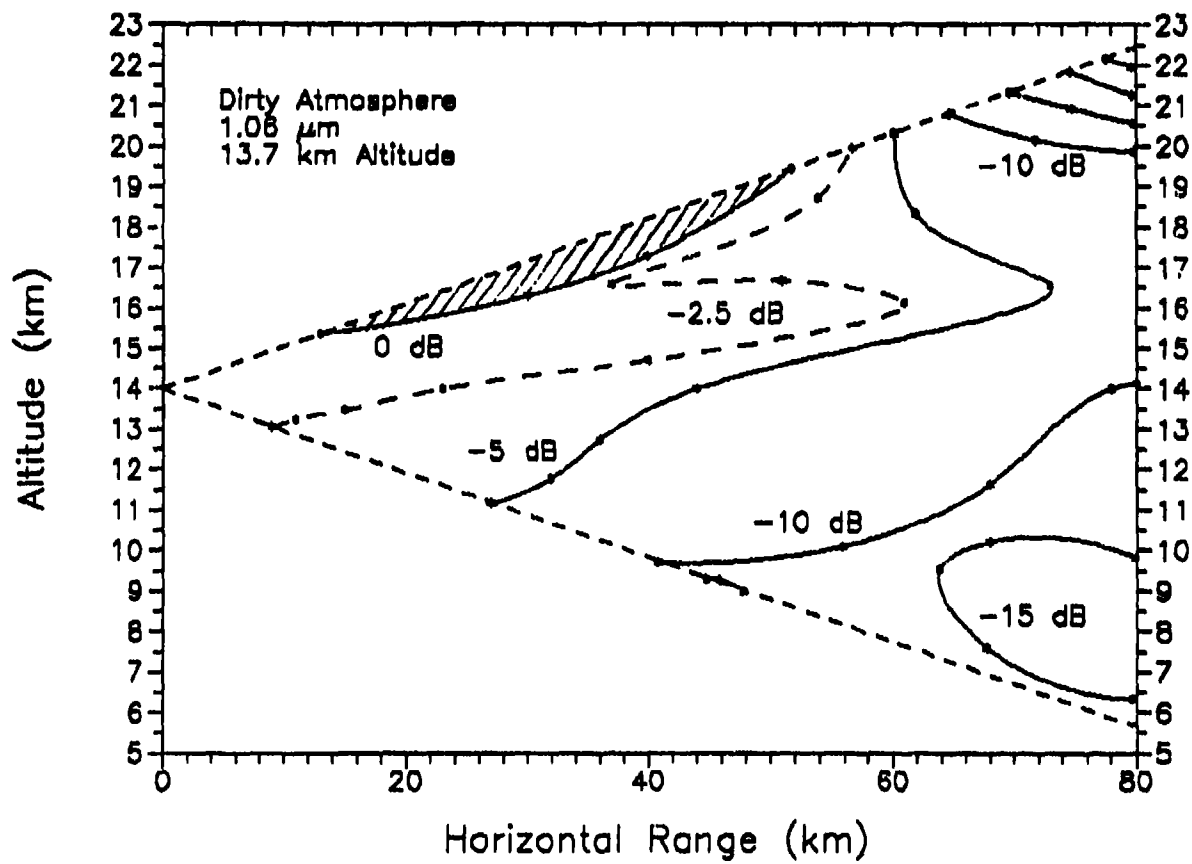


Figure 4-11.a. Signal-to-Noise Ratio for Dirty Atmosphere, Aircraft at 13.7 km Altitude, and 1.064 μm

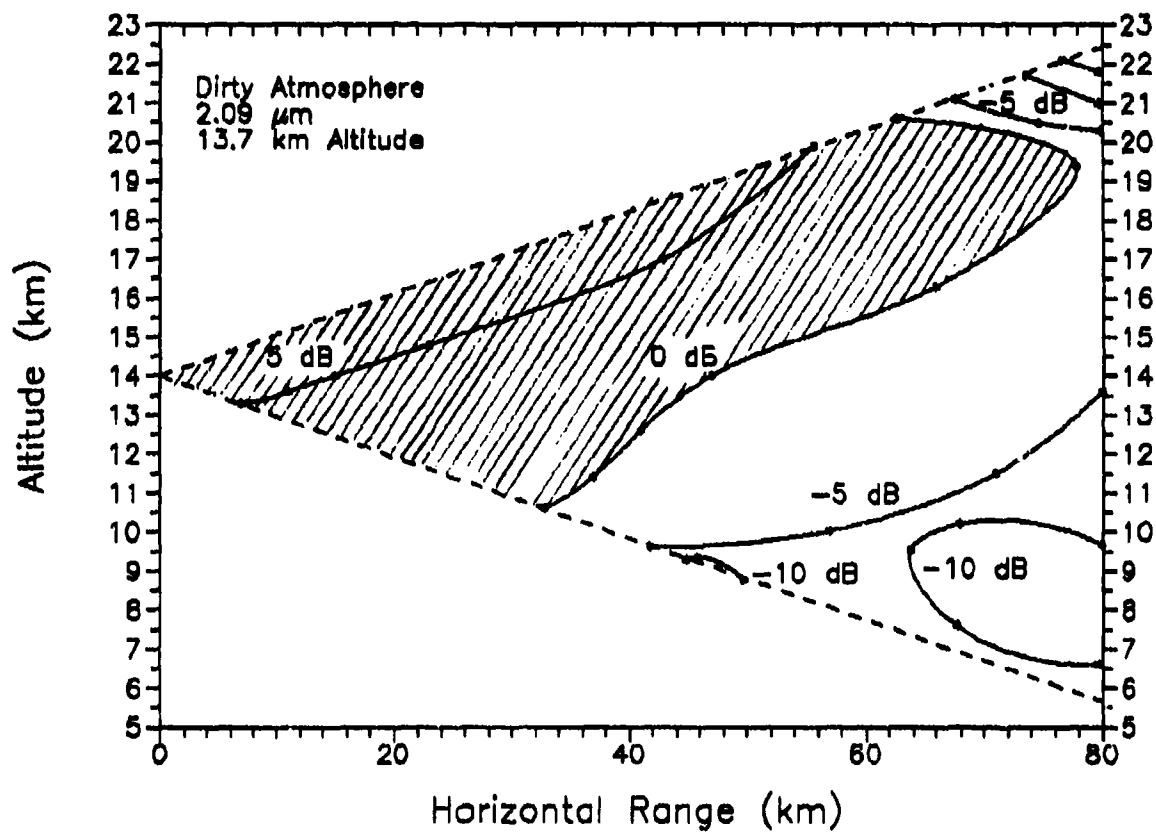


Figure 4-11.b. Signal-to-Noise Ratio for Dirty Atmosphere, Aircraft at 13.7 km Altitude, and 2.091 μm

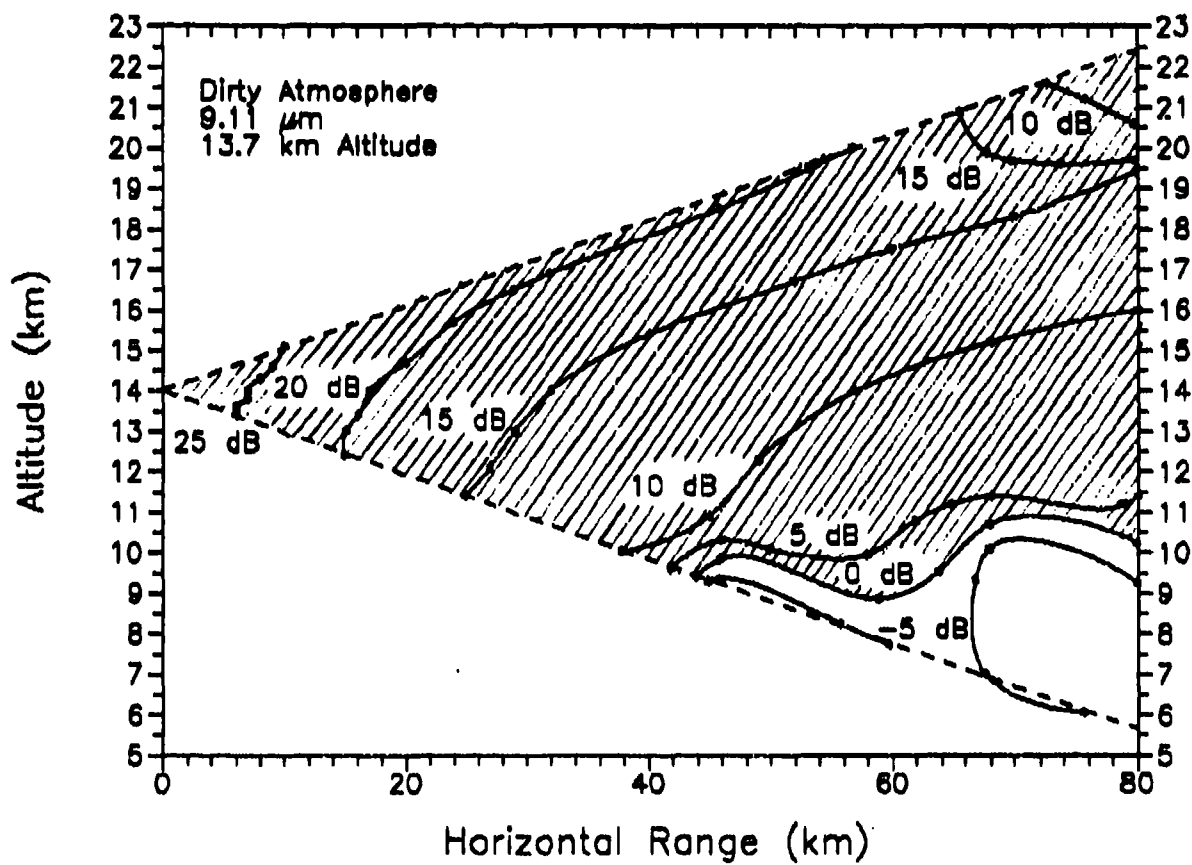


Figure 4-11.c. Signal-to-Noise Ratio for Dirty Atmosphere, Aircraft at 13.7 km Altitude, and 9.115 μm

altitude, maximum detection range is about 22 km horizontally, 45 km at +6 degrees up, and over 80 km at -6 degrees down. As expected, the troposphere has the lowest signal-to-noise values. At 13.7 km altitude, a maximum detection range of about 47 km is evident for near horizontal look angles.

In the dirty atmosphere case, the 1.064 μm lidar again fails to show any reasonable performance. The 2.091 μm lidar does exhibit good signal levels from the stratospheric regions due to the increased volcanic aerosol. Detection ranges beyond 80 km are evident for the 9 km altitude case looking up into the volcanic layer. At 13.7 km altitude, the 2.091 μm lidar shows maximum detection range from 30 km looking down to nearly 80 km looking up. Except for the tropopause and free tropospheric regions, the 9.115 μm lidar shows reasonably good detection capability out to 80 km in range. Stratospheric returns again are the highest of any region; however, comparison with measured stratospheric backscatter data indicates that the dirty atmosphere model is not very realistic.

It is apparent that none of the lidars are capable of detecting wakes in the clean tropopause and free tropospheric regions. This result is unfortunate since this area is the prime location for cruising aircraft. Also evident in these results is that it takes a major volcanic eruption to provide sufficient signal level for wake detection in the stratosphere. Obviously, this is unacceptable. One interesting observation is that while there is a good correlation between backscatter coefficient and extinction coefficient (they both increase together), areas with higher aerosol backscatter coefficient showed high signal levels despite the increase in extinction. Thus, backscatter coefficient appears to be the real factor for determining lidar performance.

Surprisingly, the 9.115 μm lidar performed better than the short wavelength lidars in all cases. This result is surprising since the aerosol backscatter coefficients are *higher* at the shorter wavelengths. There may be several explanations for this observation. First, since shot noise power is inversely proportional to wavelength, shot noise is roughly 9 times higher at 1.064 μm than at 9.115 μm . Signal-to-noise ratio is thus degraded accordingly.

Second, loss in spatial coherence due to refractive turbulence at long ranges is significant at 1.064 μm and even at 2.091 μm . From Figure 2-9, the transverse coherence length at 80 km range is only about 0.13 m for the 1.064 μm case. Transverse coherence length at 9.115 μm is 1.7 m at 80 km range, still much larger than the receiver diameter. The result is that signal-to-noise ratio at 80 km range is reduced by a factor of about 3 at 1.064 μm and by a factor of only 1.02 at 9.115 μm . These calculations assumed a constant value of C_n^2 of $10^{-17} \text{ m}^{-2/3}$, which should be fairly conservative.

Third, for an unfocused system the wavefront mismatch at short ranges is very degrading for the short wavelength lidars due to the fact that even slight curvature of the received wavefront causes destructive interference with the plane wave local oscillator beam at the edges of the detector. The term

$$\left[\frac{\pi D^2}{4 \lambda R} \right]^2$$

in the signal reduction factor (SRF) describes this effect. At the relatively short range of 20 km, this term takes on a value of 11.0 at 1.064 μm . At 9.115 μm , this term is only 0.15. The degradation in signal-to-noise ratio at 20 km range is thus about a factor 12 at 1.064 μm . At 80 km range, this degradation is down to only 1.7, neglecting refractive turbulence losses.

Fourth, the total attenuation at shorter wavelengths is higher. In addition to higher aerosol attenuation, the shorter wavelengths also receive substantial extinction from molecular scattering. At 80 km horizontal range in the tropopause, two way transmissions at 1.064 μm and 9.115 μm are 0.852 and 0.990, respectively. Fifth, the higher molecular backscatter at shorter wavelengths also degrades signal-to-noise ratio, although, as discussed in chapter 2, this effect should be relatively small. The combination of these five explanations appears to account for the relatively poor performance of the short wavelength lidars at all ranges.

It seems reasonable to conclude that high altitude wake detection taking into account only naturally occurring aerosol backscatter is not feasible with the given lidar system parameters; however, improvement in signal-to-noise ratio may be made by using higher laser pulse energies, averaging return signals, or using larger receivers.

Increasing the pulse energy of the transmitter laser will also increase signal-to-noise ratio proportionally. For this analysis, we assumed a pulse energy of 0.2 J. By increasing pulse energy by a factor of 10 to 2 J, signal-to-noise ratio will also increase by a factor of 10. In Figures 4-6 through 4-11, the resulting minimum signal-to-noise ratio would be -10 dB. The 1.064 μm lidar still would not be capable of any appreciable detection range for all but the dirtiest of atmospheres. The performance of the 2.091 μm lidar would be much improved, but long range detection in the tropopause would still be out of the question. The 9.115 μm lidar would perform adequately in the moderate and dirty atmospheres, but would be limited in the clean regions of the atmosphere.

Receiver area is also directly proportional to signal-to-noise ratio; however, refractive turbulence degradations limit the maximum size of the aperture. Figure 2-9 shows that for 80 km detection range,

the maximum usable receiver diameters are 0.13 m at 1.064 μm , 0.3 m at 2.091 μm , and 1.7 m at 9.115 μm . Obviously, no improvements could be made in the 1.064 and 2.091 μm lidar performances at ranges beyond 80 km. Increasing the receiver diameter of the 9.115 μm lidar to 1 m (probably out of the question for a flyable system!) would result in an increase in signal-to-noise ratio of about a factor of 11. As shown above, this would still leave the clean areas of the atmosphere undetectable.

Probably the most realistic improvement in signal-to-noise ratio could come from averaging the return signals from several pulses in the same scattering volume. The ideal improvement in signal-to-noise ratio is $N^{1/2}$ for N independent shots averaged. In reality, however, the improvement is somewhat less due to "a small but long-term temporal autocorrelation caused by time-varying atmospheric effects (Menyuk et al., 1983:186)." Thus, averaging 10 shots would result in a signal-to-noise ratio increase slightly less than 5 dB. The main problem with shot averaging is the scanning limitation that it imposes. Since the lidar probe beam is so narrow, in order to scan large solid angles, a large number of sample pulses would be required. By averaging shots from each beam angle, the required pulse rate to scan a reasonable solid angle in a reasonable amount of time would be, well, unreasonable.

Even with the signal-to-noise ratio improvements discussed above, aircraft wake detection at high altitude for backscatter from atmospheric aerosols alone does not appear practical.

5. Exhaust Trails

Particulates in the exhaust trail of an aircraft may provide an enhancement in backscatter from the wake. In this chapter, a first-look analysis will be made to try and determine the magnitude of this enhancement. Two types of exhaust clouds will be studied: 1) soot particles from engine combustion, and 2) ice particles from condensed water vapor in the exhaust. Since soot is a by-product of combustion, it should always be present at some level in the wake. During certain atmospheric conditions, water vapor from engine exhaust condenses and forms highly visible contrails. It is expected that backscatter from contrail particles is very high and will easily facilitate lidar wake detection. Backscatter from soot, however, may or may not be substantial.

5.1. Soot Emissions

Soot particles are the primary particulate in the hot, uncondensed exhaust from jet engines. Since soot is always present in the exhaust trail, it may provide enhancement in the backscatter coefficient within the aircraft wake. In the following analysis, a brief description of soot formation and particle characteristics will be given. Following that, Mie scattering calculations will be made on several particle size distributions from published jet engine exhaust measurements. From these scattering calculations, backscatter levels in the equilibrium wakes of four aircraft will be estimated to determine the magnitude of enhancement in lidar wake detection performance.

5.1.1. Formation

Soot is the by-product of imperfect, or incomplete, combustion. Some of the carbon atoms that are liberated from fuel during combustion do not combine with oxygen atoms to form exhaust gases such as CO and

CO₂. These free carbon atoms coagulate together to form soot particles. Immediately after combustion, most of the soot particles are composed of clumps of around 60 carbon atoms. These initial soot particles have a particle size of about 0.02 μm (Wander, 1990). As the exhaust flows out of the engine and into the atmosphere, soot particles collide and stick together forming larger particles. This process of agglomeration continues as the exhaust cloud diffuses into the atmosphere. Unfortunately for us, these particles are not spherical but tend toward long chains of connected smaller particles (Iskander et al., 1989; and Wander, 1990).

In steady state, the distribution of soot particles sizes appears to approach a lognormal distribution (Rosen and Greegor, 1974:244). Three published soot size distributions are listed in Table 5-1. The AFGL model is for atmospheric soot from urban sources, and the NRC model for is soot following nuclear detonation in the atmosphere. The model by Rosen and Greegor is the model fit to measured particle size distributions in the wake of an F-104 aircraft at 30,000 feet altitude. These models will be used for comparison of backscatter coefficients calculated from measured jet engine exhaust soot distributions.

Table 5-1. Three Published Soot Particle Size Distribution Models

Model	Distribution	Mean Radius (μm)	Standard Deviation	Relative Number Density (cm^{-3})
AFGL*	Sum of 2 Log-normal*	0.03 0.5	0.35 0.4	0.999875 0.000125
NRC**	Lognormal	0.1	0.30	1
Rosen & Greegor***	Sum of 2 Log-normals	0.08 0.3	0.137 0.2	0.997 0.003

*(Fenn et al., 1985:18-)

** (NRC, 1985)

***Adapted from (Rosen and Greegor, 1974:244)

5.1.2. Mie Scattering Calculations

Several references were located that contained measured particle size distributions from jet engine exhaust (Mathews et al., 1984; Johnson et al., 1985; and Spicer et al., 1987). These size distributions were input to computer and a Mie scattering program was used to calculate the total scattering coefficient and phase functions for each distribution. Using the equations in chapter 2, the volume backscatter coefficient was then computed. Even though soot particles are not spherical, Mie scattering calculations were used to give a rough estimate of the magnitude and range of backscatter coefficients in jet engine exhaust. These results should be accurate to within at least an order of magnitude, if not better. For comparison, backscatter coefficients for the theoretical soot size distributions in Table 5-1 were also computed using the Mie code. The comparison of results will be discussed later in this section.

The measured particle size distributions are listed in the Appendix. Table 5-2 lists the engine type, thrust setting, approximate plume diameter at measurement point, and total particle concentration for each data set. Some extrapolations of the size distributions were necessary since most of the measurements did not cover a wide enough range of particle sizes. The refractive indices of soot at the three wavelengths of interest were taken from Fenn et al. (1985:18-17) and are listed in Table 5-3. For the TF30-P1 and J52-P3 data sets, the particle size distribution data was given in mass density per unit volume. For the Mie scattering calculations, these data were converted to number density using the equation

$$n(r) = \frac{3\rho_c}{8\pi\Delta r^2\rho_s} \left[\frac{1}{r_1^3} - \frac{1}{r_2^3} \right] \quad (5-1)$$

where

$n(r)$ = particle number density ($\text{cm}^{-3}\mu\text{m}^{-1}$)

r = particle radius (cm)

ρ_c = particle cloud density (g/cm^3)

ρ_s = soot density = $1.5 \text{ g}/\text{cm}^3$

$\Delta r = r_2 - r_1$ (cm)

Table 5-2. Jet Engine Exhaust Data Sets Used in Mie Scattering Calculations

Engine Type ^(ref)	Thrust (lbs)	Plume Diameter (m)	Total Particle Concentration (cm^{-3})
TF30-P1 ¹	9,500*	6	9.78×10^8
TF30-P1 ¹	9,500*	8"	4.74×10^8
J52-P3 ²	8,500*	6"	2.35×10^8
J52-P3 ²	8,500*	8"	3.76×10^8
TF30-P103 ³	518	1.2"	4.92×10^8
TF30-P103 ³	2,934	1.2"	5.96×10^8
TF30-P103 ³	7,317	1.2"	5.18×10^8
TF30-P103 ³	9,785	1.2"	3.98×10^8
TF30-P109 ³	563	1.2"	2.17×10^8
TF30-P109 ³	3,200	1.2"	3.68×10^8
TF30-P109 ³	7,998	1.2"	3.44×10^8
TF30-P109 ³	10,633	1.2"	2.82×10^8
TF41-A2 ³	460	1"	3.31×10^8
TF41-A2 ³	3,818	1"	3.76×10^8
TF41-A2 ³	9,554	1"	3.32×10^8
TF41-A2 ³	12,937	1"	4.26×10^8

*Estimate

¹(Mathews et al., 1984)

²(Johnson et al., 1985)

³(Spicer et al., 1987)

NOTE: TF = turbofan, J = turbojet

For each exhaust data set above, the backscatter coefficient at each of the three infrared wavelengths was computed and plotted versus engine thrust divided by plume area. This normalization of engine

Table 5-3. Refractive Index of Soot at Three Infrared Wavelengths

Wavelength (μm)	Refractive Index
1.064	1.750-j0.440
2.091	1.805-j0.495
9.115	2.176-j0.700

thrust allows comparison of backscatter coefficients for all engines since it is assumed that the mass of soot in the exhaust plume is proportional to engine thrust and is inversely proportional to plume area. The actual relationship between engine power setting and backscatter coefficient is probably complex since backscatter is very dependent upon the particle size distribution. Measured data seems to show that mean particle size increases with increasing thrust, while the total number of particles does not change appreciably (Spicer et al., 1987:60). The data is shown in Figures 5-1.a-c. These graphs show that backscatter coefficient can easily span two orders of magnitude between clean and dirty engines. Also shown on the graphs are power law best line fits to data. The power law fit has no known theoretical basis; it was simply chosen for a straight line fit on log-log axes. The best line fits appear to be representative of moderately clean engines. Newer, clean burning turbofan engines will likely fall below these lines.

From chapter 2, we know that the exhaust products become wrapped up in the recirculation cell surrounding the wake vortices. Since no mass is transferred across the recirculation cell boundary, we may assume that all the exhaust particles are entrained within it. In addition, we will assume that these particles are uniformly distributed within the recirculation cell. This assumption seems good due to the highly turbulent air within the recirculation cell itself. The backscatter coefficient in the wake may be estimated from the graphs above by finding the total thrust per unit area in the recirculation cell. The ratios of

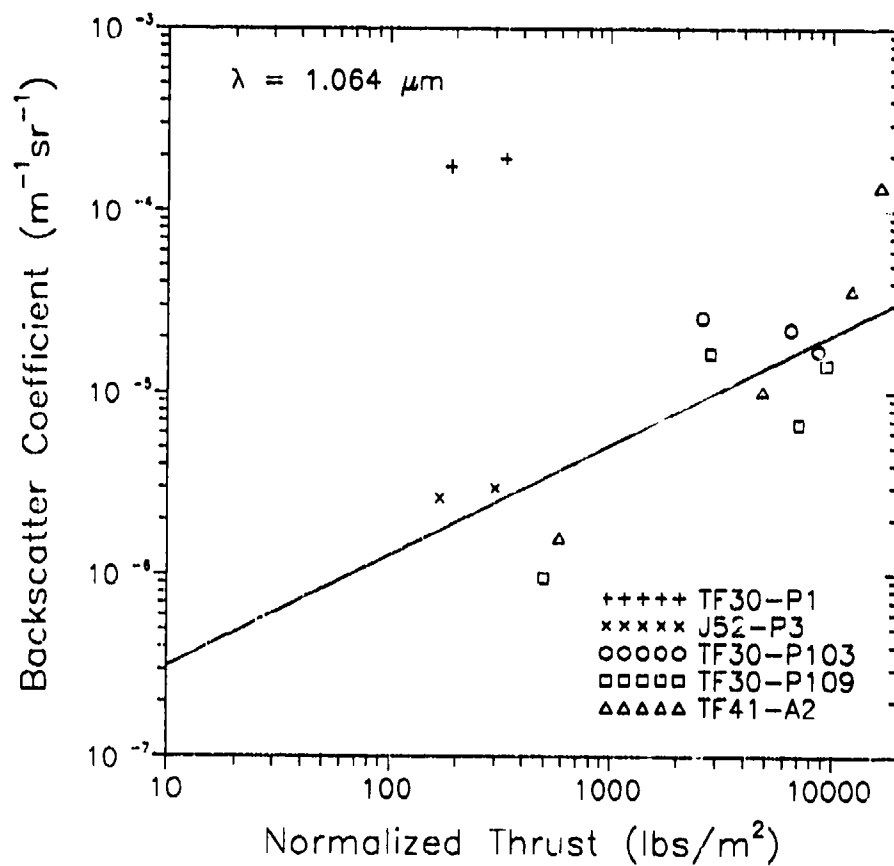


Figure 5-1.a. Exhaust Backscatter Coefficients at $1.064 \mu\text{m}$ versus Normalized Thrust

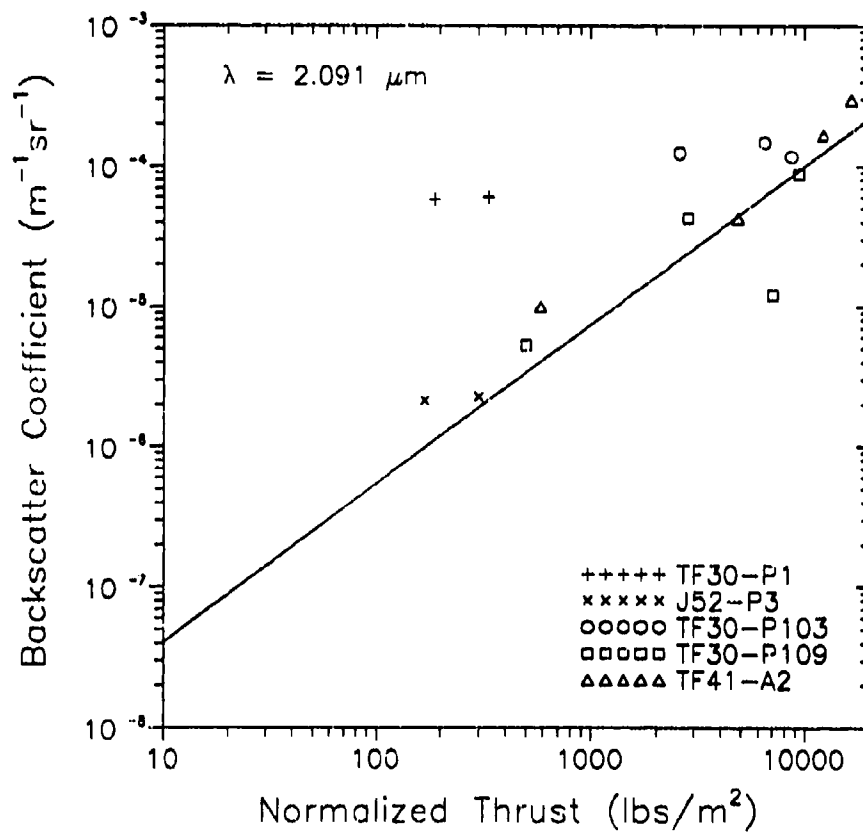


Figure 5-1.b. Exhaust Backscatter Coefficients at $2.091 \mu\text{m}$ versus Normalized Thrust

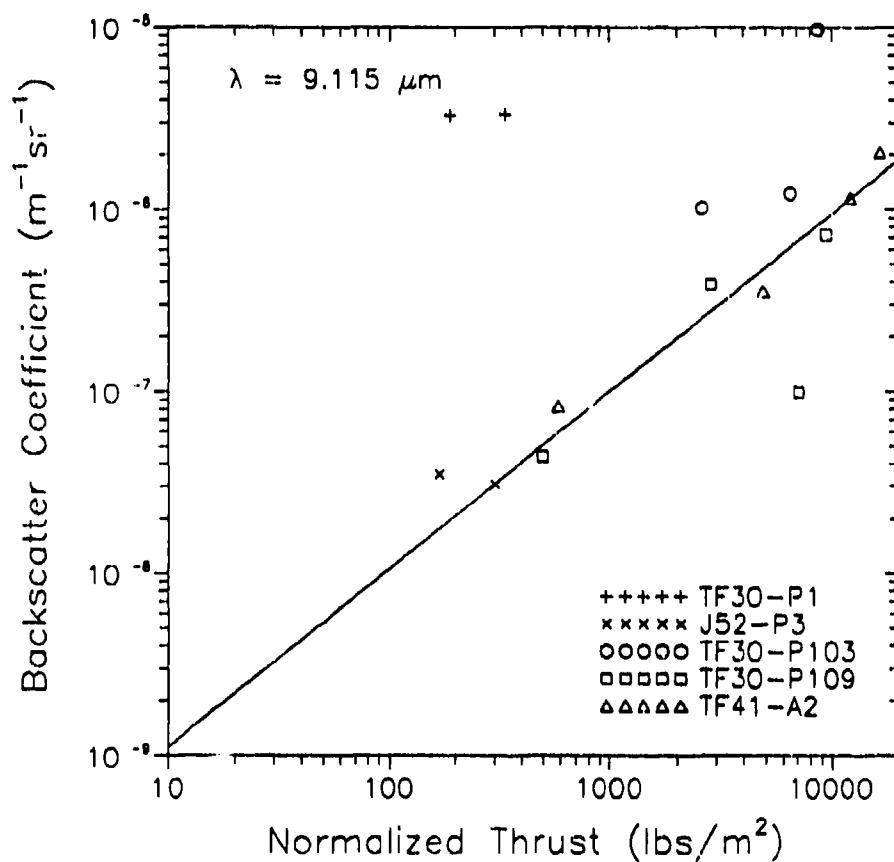


Figure 5-1.c: Exhaust Backscatter Coefficients at $9.115 \mu\text{m}$ versus Normalized Thrust

total maximum thrust to recirculation cell area for the four test aircraft are listed in Table 5-4. Table 5-5 lists the estimated exhaust backscatter coefficients in the wakes of these aircraft taken from the best line fits to the data in Figures 5-1.a-c.

Table 5-4. Ratio of Maximum Thrust to Recirculation Cell Area for Four Aircraft

Aircraft	Thrust/Area (lbs/m ²)
Large Transport	20
Medium Transport	17
Large Fighter	177
Small Fighter	89

Table 5-5. Mean Exhaust Backscatter Coefficients in the Wakes of Four Aircraft

Aircraft	$\beta_p(\pi),$ 1.064 μm (m ⁻¹ sr ⁻¹)	$\beta_p(\pi),$ 2.091 μm (m ⁻¹ sr ⁻¹)	$\beta_p(\pi),$ 9.115 μm (m ⁻¹ sr ⁻¹)
Large Transport	5x10 ⁻⁷	9x10 ⁻⁸	2.2x10 ⁻⁹
Medium Transport	4x10 ⁻⁷	7x10 ⁻⁸	1.8x10 ⁻⁹
Large Fighter	1.7x10 ⁻⁶	1.0x10 ⁻⁶	2.0x10 ⁻⁸
Small Fighter	1.2x10 ⁻⁶	5x10 ⁻⁷	1.0x10 ⁻⁸

For comparison, the three model size distributions in Table 5-1 were also run through the Mie scattering program. Since these models represent relatively steady state soot size distributions, they should be indicative of the soot size distributions in the middle and late wake stages. The total number densities were scaled for clean and dirty engines based on total soot mass per unit volume, which are readily available parameters of jet engine soot emissions. Newer high-bypass engines have soot emissions of less than 2 mg/m³ at the exit nozzle, while some older engines may have emissions as high as 20-30 mg/m³.

(Pitz, 1987:3). Table 5-6 lists the calculated backscatter coefficients for the three models and for clean (1 mg/m³ soot) and dirty (30 mg/m³ soot) engines.

Table 5-6. Modeled Soot Backscatter Coefficients for Clean and Dirty Jet Engines

Soot Model	Engine	$\beta_b(\pi),$ 1.064 μm (m ⁻¹ sr ⁻¹)	$\beta_b(\pi),$ 2.091 μm (m ⁻¹ sr ⁻¹)	$\beta_b(\pi),$ 9.115 μm (m ⁻¹ sr ⁻¹)
AFGL	Clean	1.55x10 ⁻⁶	9.17x10 ⁻⁷	2.76x10 ⁻⁷
"	Dirty	4.66x10 ⁻⁵	2.75x10 ⁻⁵	8.28x10 ⁻⁶
NRC	Clean	1.52x10 ⁻⁶	1.58x10 ⁻⁶	2.65x10 ⁻⁷
"	Dirty	4.57x10 ⁻⁵	4.73x10 ⁻⁵	7.94x10 ⁻⁶
R & G	Clean	1.38x10 ⁻⁵	2.91x10 ⁻⁶	3.34x10 ⁻⁷
"	Dirty	4.14x10 ⁻⁴	8.74x10 ⁻⁵	1.00x10 ⁻⁵

The data above shows surprisingly little variance from model to model. This result lends confidence to the backscatter calculations for soot since backscatter in the infrared seems to be only mildly sensitive to changes in the size distributions. This insensitivity is probably due to the small particle sizes compared to the infrared wavelengths used.

In order to compare these results with calculations based on measured engine particle distributions, some assumptions must be made about engine thrust and nozzle diameter. If we assume engine thrusts from 10,000 to 20,000 lbs and a 1 m nozzle diameter, then the normalized thrust to plume areas would be from 12,700 lbs/m² to 25,400 lbs/m². From Figures 5-1.a-c, the backscatter coefficients for modeled data are generally lower than for measured data, particularly at 1.064 and 2.091 μm . If the normalized thrust for the modeled size distributions was between 100-1000 lbs/m², the data would correlate well with measured data. Only measured data will be used in the performance analysis.

5.1.3. Performance Analysis

The wake backscatter coefficients in Table 5-5 represent the expected levels for moderately clean engines. These values may be compared to the backscatter coefficients for the atmospheric aerosol models developed in chapter 4. Except for boundary layer aerosols and extreme volcanic aerosols, soot backscatter in the four aircraft wakes are higher than the ambient aerosol backscatter levels.

To estimate the improvement in lidar performance due to the presence of exhaust soot, signal-to-noise ratio was computed for a lidar looking horizontally through the clean atmosphere tropopause at 9 km altitude. The backscatter coefficient was taken to be the sum of the ambient aerosol backscatter coefficient and the exhaust backscatter coefficient. Since lidar performance was shown to be worst in the tropopause (chapter 4), this simulation should indicate the minimum performance assuming enhancement by exhaust soot. Data from these simulations are shown in Figures 5-2.a-c. These simulations do not take into account the reduction in signal-to-noise ratio within a single range gate for pulse lengths that are much wider than the wake.

As the data in Figures 5-2.a-c show, the enhancement in signal-to-noise ratio due to exhaust soot is very significant in very clean atmosphere. Interestingly, the fighter aircraft had the highest enhancement due to the much higher thrust/wake area ratios. These simulations show detectability of fighter aircraft wakes in excess of 80 km in the tropopause at all wavelengths. Maximum detection range for the transport aircraft varies from 50-75 km. If the exhaust backscatter coefficients used here are reduced by a factor of 10, the corresponding signal-to-noise ratio will also be reduced by a factor of 10. This reduction would eliminate any wake detection by the $1.064\text{ }\mu\text{m}$ as well as transport wakes by the $2.091\text{ }\mu\text{m}$ lidar. Maximum detection range of fighter air-

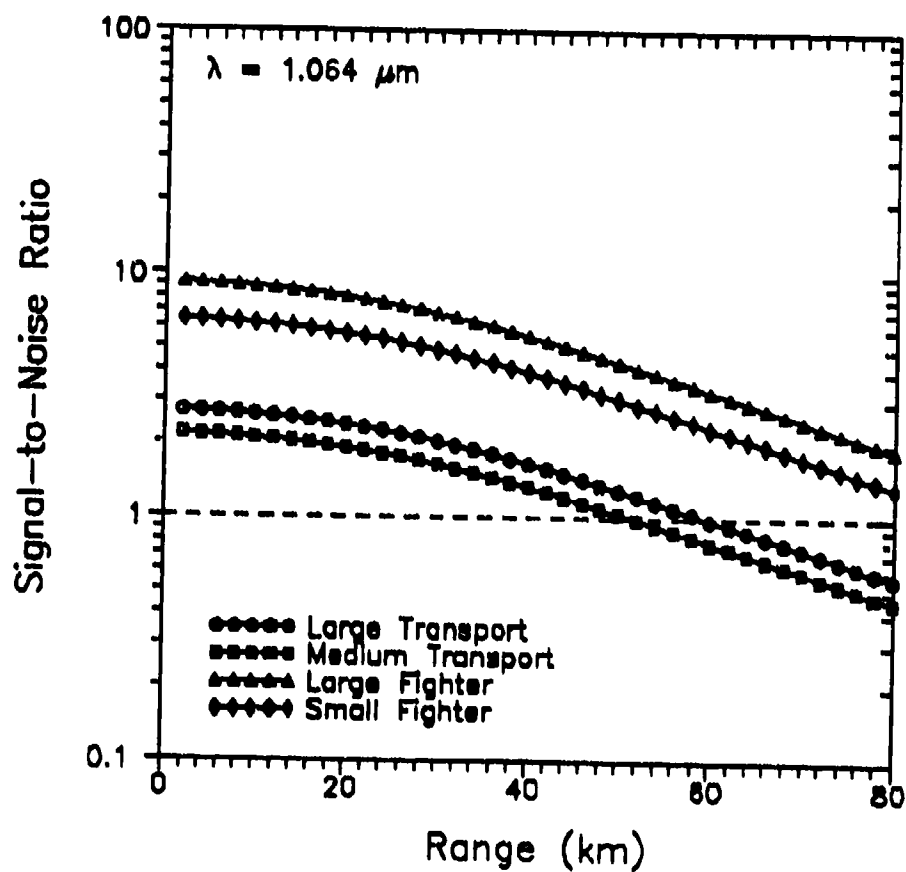


Figure 5-2.a. Signal-to-Noise Ratio in the Soot Enhanced Wakes of Four Aircraft at Ranges from 0-80 km. Wavelength is 1.064 μm, and lidar is at 9 km altitude looking horizontally.

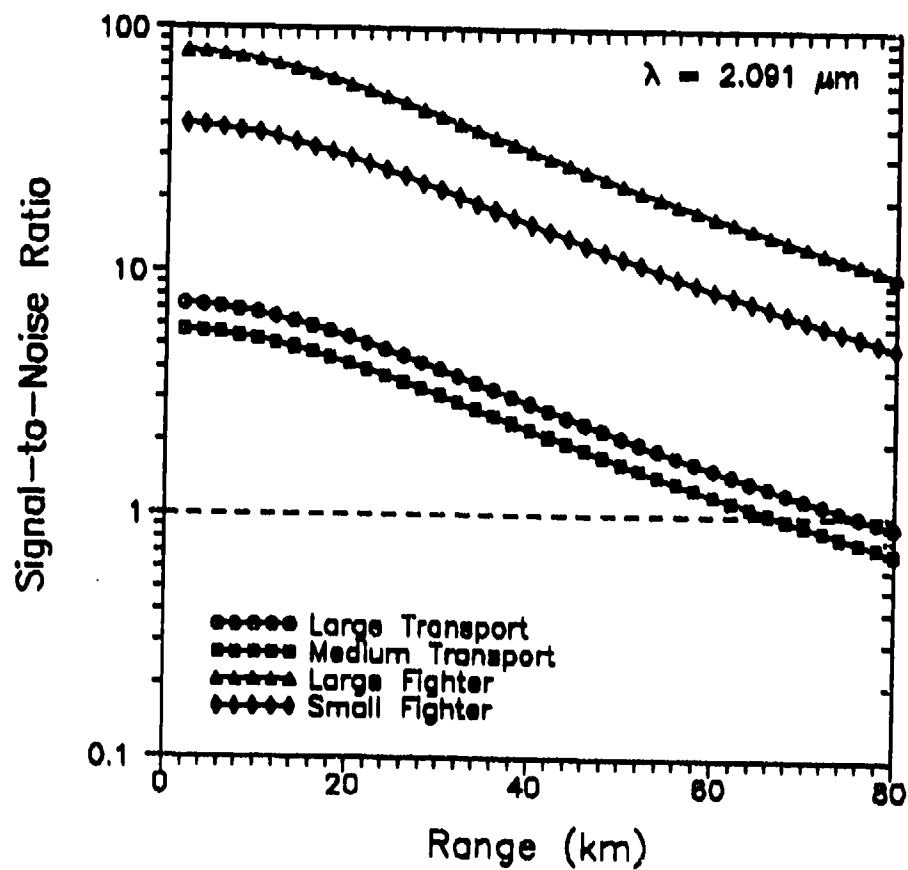


Figure 5-2.b. Signal-to-Noise Ratio in the Soot Enhanced Wakes of Four Aircraft at Ranges from 0-80 km. Wavelength is 2.091 μm, and lidar is at 9 km altitude looking horizontally.

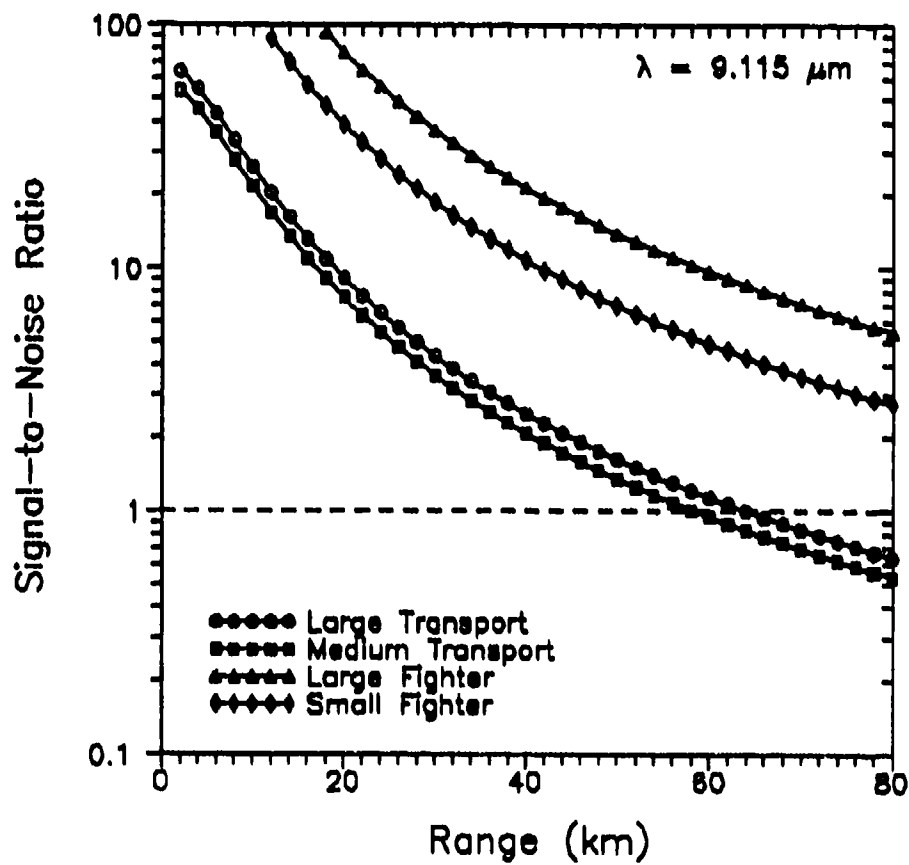


Figure 5-2.c. Signal-to-Noise Ratio in the Soot Enhanced Wakes of Four Aircraft at Ranges from 0-80 km. Wavelength is $9.115 \mu\text{m}$, and lidar is at 9 km altitude looking horizontally.

craft wakes would fall to 50-80 km at 2.091 μm and 40-60 km at 9.115 μm . This is still an improvement over detection performance for atmospheric aerosol backscatter only.

An additional benefit of the enhancement by exhaust particles is the fact that velocity width of the return signal will not be degraded as much by longer pulse lengths. Figures 3-5.a-d showed how this wake signature was reduced at longer pulse lengths; however, these graphs were produced assuming backscatter was homogeneous inside and outside the wake. For exhaust enhanced wake signals, the highly turbulent air within the recirculation cell will contribute more to the signal than the air outside this region. The resulting velocity width of the return signal should be higher and the wake should be even easier to detect than for the ambient aerosol case.

5.2. Contrails

In contrast to soot, contrails are not always present in aircraft wakes; however, due to their high visibility, it is assumed that the enhancement in backscatter from aircraft contrails will be very significant. In this subsection, aircraft contrail formation will be briefly described, estimations will be made of the backscatter levels from contrails, and corresponding detection performance will be analyzed.

5.2.1. Formation

A technical reference put out by the Air Force Air Weather Service gives a good overview of contrail formation (Air Weather Service, 1981:1):

Condensation trails (contrails) are elongated tubular-shaped clouds composed of water droplets or ice crystals which form behind aircraft when the wake becomes supersaturated with respect to water.

The most important type of condensation trail arises when the water vapor in the exhaust gas mixes with and saturates the air in the wake of the aircraft (Appleman, 1953). Combustion of the hydrocarbon fuels used in aircraft - both propeller and jet - injects both water vapor and heat into the wake. The added moisture raises the relative humidity in the wake, while the added heat lowers it. Whether or not the wake will reach saturation depends on the ratio of water vapor to heat in the exhaust gas and on the initial pressure, temperature, and relative humidity of the environment.

Figure 5-3, taken from the same source, shows a graph of the relative humidity, pressure, and temperature required for contrail formation from jet aircraft. The graph is for theoretical behavior; actual contrail formation varies from this predicted behavior slightly (Air Weather Service, 1981:10-11). The diagonal lines across the graph represent the minimum relative humidity required for contrail formation. Regions to the left of the 0% relative humidity line are where contrails should always form, and regions to the right of the 100% relative humidity line are where contrails should never form. Note that at 0% relative humidity, contrails may still form, but it takes a lower temperature than for 100% relative humidity (at constant pressure). Also of note is the fact that engine power setting is nearly independent of contrail formation. Only contrail intensity varies with engine power (Air Weather Service, 1981:8).

In a brief literature search on contrails, no particle size distribution data was located. Additionally, no sources were found that indicated when contrails contained water droplets and when they contained ice crystals. Contrails are likely to be composed of mostly water droplets immediately after formation. After some period of time, these water droplets may form into ice clouds similar in form to cirrus clouds if conditions are right. A more in-depth search is obviously needed.

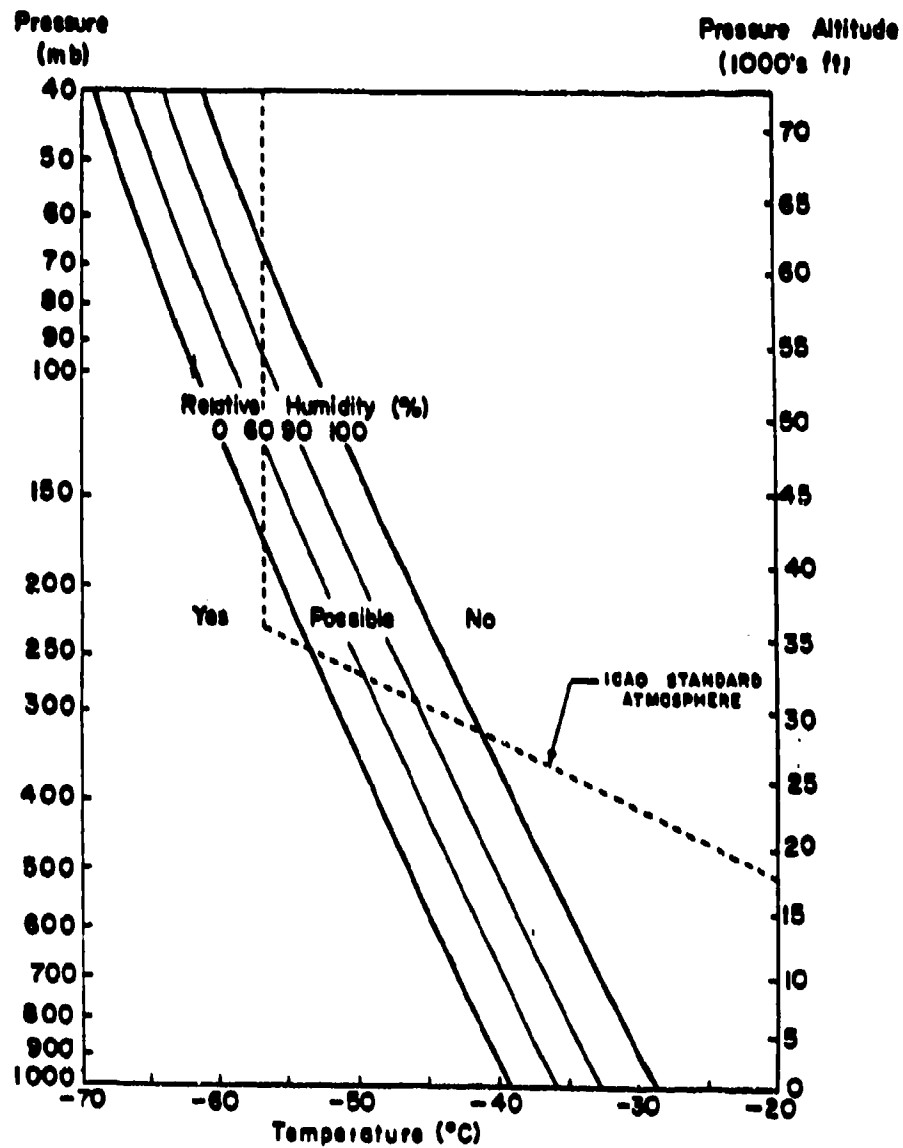


Figure 5-3. Jet Aircraft Contrail Formation as a Function of Relative Humidity, Pressure, and Temperature (Air Weather Service, 1981:5)

5.2.2. Backscatter Estimation

Since no size distribution data were located, some assumptions were made on size distribution and number density in order to calculate backscatter coefficients. It was assumed that contrails would be primarily composed of ice crystals. This assumption should not have a great impact on final results since the backscatter coefficients from water droplet contrails should not be much different as the total water content would be the same. Thus, cirrus cloud particle size distributions were used. The size distributions for four types of cirrus clouds were used: 1) cirrostratus, 2) cirrus uncinus, 3) warm cirrus, and 4) cold cirrus (Takano and Liou, 1989:6). The appendix lists the size distribution data for each cirrus model.

Although ice particles are not spherical, these size distributions were run through the Mie scattering program to calculate total scattering coefficients and phase functions. The complex refractive indices of ice at the three wavelengths of interest are listed in Table 5-7 (Warren, 1984). For comparison, the scattering coefficients derived from Mie scattering calculations are listed in Table 5-8 along with the scattering coefficients at 1 and 2 μm derived by Takano and Liou (1989:9) for hexagonal ice crystals. Unfortunately, no 9 μm data was located. Finally, the backscatter coefficients from Mie scattering results are shown in Table 5-9.

The minimum cutoff wavelength used in the Mie calculations was 0.01 μm ; however, no mention was made in the source article about minimum cirrus particle size. To test the sensitivity of the results to larger minimum particle sizes, the Mie code was run again on the cirrus uncinus model for minimum radii of 0.01 μm , 0.1 μm , 1.0 μm , and 10.0 μm . At a minimum size of 10.0 μm , the 1.064 μm wavelength backscatter coefficient

dropped by a factor of 1.7. The 9.115 μm wavelength was totally insensitive to these changes. The overall results, therefore, should not be affected very much by this assumption on minimum particle size.

Table 5-7. Refractive Index of Ice at Three Infrared Wavelengths

Wavelength (μm)	Refractive Index
1.064	$1.301 - j1.96 \times 10^{-6}$
2.091	$1.270 - j9.0 \times 10^{-4}$
9.115	$1.265 - j4.45 \times 10^{-2}$

Table 5-8. Comparison of the Ice Crystal Scattering Coefficients derived from Mie Scattering and by Takano and Liou for Hexagonal crystals

Cirrus Cloud Model	Wavelength (μm)	β_{Mie} Mie Scattering (km^{-1})	$\beta_{\text{Takano \& Liou}}$ Takano & Liou (km^{-1})
Cirrostratus	1	0.3969	0.3863
"	2	0.3504	0.3550
Cirrus Uncinus	1	5.792	2.601
"	2	3.646	2.084
Warm Cirrus	1	0.8215	0.6521
"	2	0.6312	0.5973
Cold Cirrus	1	0.0963	0.1662
"	2	0.0848	0.1584

Table 5-9. Backscatter Coefficients for Four Cirrus Cloud Models Derived from Mie Scattering

Cirrus Model	$\beta_{\text{b}}(\pi)$, 1.064 μm ($\text{m}^{-1}\text{sr}^{-1}$)	$\beta_{\text{b}}(\pi)$ 2.091 μm ($\text{m}^{-1}\text{sr}^{-1}$)	$\beta_{\text{b}}(\pi)$ 9.115 μm ($\text{m}^{-1}\text{sr}^{-1}$)
Cirrostratus	1.2×10^{-6}	4.0×10^{-7}	1.5×10^{-8}
Cirrus Uncinus	2.9×10^{-5}	1.1×10^{-6}	2.5×10^{-7}
Warm Cirrus	4.8×10^{-6}	3.6×10^{-7}	5.0×10^{-8}
Cold Cirrus	3.7×10^{-7}	2.9×10^{-8}	1.2×10^{-8}

The results in Table 5-9 carry a number of assumptions with them. They assume spherical particles that are randomly oriented and spaced. In addition, they assume the particles are isotropic and that the back-

Table 5-10. Measured Cirrus Cloud Backscatter Coefficients at 10.6 μm

Cloud Altitude (km)	$\beta_s(\pi)$ 10.6 μm ($\text{m}^{-1}\text{sr}^{-1}$)
13.8 ¹	8×10^{-10}
11.6 ¹	2×10^{-8}
12.1 ¹	2×10^{-7}
14.3 ¹	1×10^{-8}
12.1 ¹	8×10^{-7}
11.9 ¹	1.2×10^{-10}
10.2 ¹	3×10^{-10}
11.6 ¹	2×10^{-10}
13.3 ¹	1×10^{-9}
12.6 ¹	3×10^{-8}
12.0 ¹	2×10^{-8}
10.0 ¹	1×10^{-8}
14.2 ¹	2.5×10^{-9}
9.0 ²	7×10^{-7}
6.5 ²	1×10^{-8}
10.2 ²	8×10^{-10}
11.3 ²	3×10^{-9}
10.0 ³	3×10^{-8}

¹Koenig and Alejandro, 1990

²Hall et al., 1988

³Gross et al., 1984

scattered light is of the same polarization as the incident light. Despite all of these assumptions, the results above, at least at 9.115 μm , fare reasonably well with measured data at 10.6 μm . Table 5-10 shows cirrus cloud backscatter coefficients measured at 10.6 μm versus cloud altitude for a number of different cirrus clouds. The data is combined from several sources, though much of it was taken during a joint U.S. Air Force/U.K. Royal Signals and Radar Establishment measurement program above Ascension Island (Koenig and Alejandro, 1990; Hall et al., 1988; and Gross et al., 1984). The wide range of cirrus backscatter coefficients indicates the variability in cirrus cloud

thickness and density. Though this data is by no means a statistically complete data set, it shows the magnitude and range of cirrus backscatter coefficients at 10.6 μm . The geometric mean backscatter coefficient from this data is $6.9 \times 10^{-9} \text{ m}^{-1} \text{sr}^{-1}$, and the geometric standard deviation is 12.6. The mean value from this data is about a factor of 5 lower than the calculated data, which has a geometric mean of $3.9 \times 10^{-8} \text{ m}^{-1} \text{sr}^{-1}$ at 9.115 μm , but this is well within one standard deviation. In addition, based on the trend indicated in calculated results, cirrus backscatter coefficient decreases with increasing wavelength in the infrared region.

The backscatter from within a contrail is expected to be higher than backscatter from naturally occurring cirrus clouds. The basis of this assumption is the dense appearance of contrails compared to nearby cirrus clouds. Some lidar data exists to verify this assumption. A measurement by Koenig using a 0.532 μm lidar shows a strong contrail return at about 10.8 km altitude above a thin cirrus layer at 10.0 km. The contrail signal was roughly an order of magnitude stronger than the cirrus signal and was probed about 15 minutes after the contrail was formed (Koenig, 1990). The contrail thickness was less than 150 m vertically. This data was the only lidar contrail measurement that could be found. Based on this evidence, a conservative estimate of contrail backscatter coefficient would be 10 times higher than the geometric mean cirrus backscatter coefficient from the four cirrus models above. Based on this assumption, Table 5-11 gives the estimated contrail backscatter coefficients at the three infrared wavelengths of interest.

Table 5-11. Estimated Contrail Backscatter Coefficients

Wavelength	$\beta_{\pi}(\pi)$ ($\text{m}^{-1} \text{sr}^{-1}$)
1.064 μm	2.8×10^{-5}
2.091 μm	2.6×10^{-6}
9.115 μm	3.9×10^{-7}

5.2.3. Performance Analysis

As for the soot analysis, signal-to-noise ratio for each lidar was computed for a lidar at 9 km altitude looking horizontally. The backscatter coefficient at this altitude was taken as the sum of the atmospheric aerosol backscatter coefficient and the estimated contrail backscatter coefficient from Table 5-9. The results are plotted in Figure 5-4 for contrails from 0-200 km in range.

As expected, signal-to-noise ratio from contrails appears to be extremely high. Figure 5-4 implies contrail detectability well beyond the 200 km limit of the graph. Again, results indicate that the 9.115 μm lidar performed best, probably due to the degrading refractive turbulence effects at the shorter wavelengths. The 1.064 μm and 2.091 μm lidars had nearly equal performance in this simulation. Even if the contrail backscatter values are a factor of 10 too high, all of the lidars would still be capable of detecting the contrail enhanced wakes at horizontal ranges beyond 100 km.

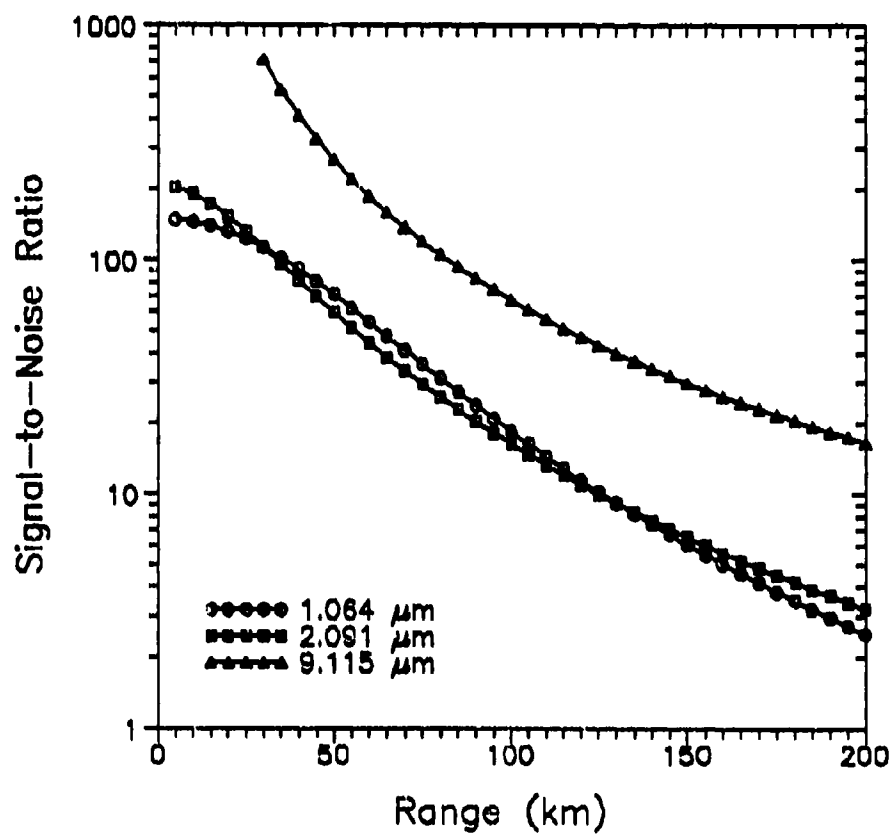


Figure 5-4. Signal-to-Noise Ratio for Contrail Enhanced Wakes at Ranges from 0-200 km. Lidar is at 9 km altitude looking horizontally.

6. Conclusions

This thesis has analyzed the performance of three infrared Doppler lidar systems for detecting aircraft wake vortices at high altitudes. Detection performance assuming backscatter from atmospheric aerosols alone was analyzed. The enhancements in backscatter and resulting wake detectability resulting from exhaust particulates were then analyzed. A short summary of these results and recommendations for further research are outlined below.

6.1. Summary of Results

Probably the easiest wake signature to detect is the increase in spectral width of the return signal from within turbulent wake regions. An analysis of the spread in spectrum width for four aircraft wakes revealed that a minimum signal-to-noise ratio of about 0 dB was necessary to detect the wakes in all cases. This minimum value was used in the subsequent analyses.

Atmospheric aerosols alone are not sufficient for detecting aircraft wakes at ranges up to 80 km in clean atmospheres. The improvements in signal-to-noise ratio discussed at the end of chapter 4 are either impractical or insufficient to bolster performance in very clean regions of the atmosphere. Interestingly, the 9.115 μm lidar performed best in simulations. For the shorter wavelengths, the relative signal-to-noise ratio degradations are due primarily to increased shot noise, wavefront mismatch at short ranges, refractive turbulence at long ranges, and higher overall extinction from both aerosols and molecules.

Enhancement in backscatter due to engine exhaust trails does appear to be sufficient for wake detection beyond 80 km, even in clean atmosphere. The fighter aircraft showed the greatest enhancement in wake backscatter due to the higher thrust to wake area ratio of these aircraft. For the soot backscatter coefficients calculated in chapter

5, detection of fighter aircraft wakes well beyond 80 km may be possible at all three wavelengths. There is, of course, some uncertainty in the backscatter estimates; however, even for backscatter coefficients that are a factor of ten less than these estimates, detection of fighter aircraft wakes appear possible at ranges from 40-80 km by both the 2.091 μm and 9.115 μm lidars.

As expected the estimated improvement in performance due to the presence of contrail particles was very significant. All lidars showed wake detectability for all four aircraft analyzed at ranges beyond 200 km when contrails were present. Even for contrail backscatter values a factor of 10 lower than estimated, wake detection was still possible beyond 100 km in range for all cases.

Currently, there is a great deal of excitement about the prospect of coherent lidar using solid state lasers at 1-2 μm . The poor signal-to-noise ratio revealed in this study for the 1.064 μm and 2.091 μm lidars, however, indicates that longer wavelength lidars, such as CO_2 , may actually perform better despite the higher backscatter coefficients at 1-2 μm .

6.2 Recommendations

The results for the atmospheric aerosol and contrail enhanced wakes seem to be fairly conclusive; however, the results for the soot enhanced wakes, while appearing positive, are not completely conclusive. It appears that soot emissions will provide the necessary enhancement in backscatter for long range detection, but this analysis made a lot of assumptions. Further research into the scattering properties of jet engine soot are needed and should ideally be supported by lidar measurements.

Further study of detection methods for wake return signals is probably also warranted. Wake signatures may exist that could be identified from signals below 0 dB. Such a finding would do much to improve detection range.

Appendix: Particle Size Distributions

Table A-1. Soot Size Distributions for TF30-P1 Engine Data

Particle Radius (μm)	Test #1 Number Density ($\text{cm}^{-3}\mu\text{m}^{-1}$)	Test #3 Number Density ($\text{cm}^{-3}\mu\text{m}^{-1}$)
0.014	1.3E+10	6.26E+9
0.047	1.58E+9	7.50E+8
0.080	1.58E+8	9.50E+7
0.173	4.10E+6	4.45E+6
0.342	1.65E+5	1.57E+5
0.551	9.23E+3	9.02E+3
0.837	2.30E+3	2.26E+3
1.285	0.0	0.0
2.333	0.0	0.0
4.163	0.0	0.0
6.420	0.592	0.576
9.230	0.352	0.160
13.87	0.0	0.0

Table A-2. Soot Size Distributions for J52-P3 Engine Data

Particle Radius (μm)	Test #7 Number Density ($\text{cm}^{-3}\mu\text{m}^{-1}$)	Test #8 Number Density ($\text{cm}^{-3}\mu\text{m}^{-1}$)
0.007	1.86E+8	1.08E+8
0.012	1.63E+7	1.78E+8
0.021	2.34E+7	0.0
0.038	0.0	6.11E+6
0.067	6.96E+5	1.63E+6
0.119	1.87E+5	3.54E+5
0.211	5.25E+4	1.63E+4
0.375	1.56E+4	1.98E+4

Table A-3. Soot Size Distributions for TF30-P103 Engine Data

Particle Radius (μm)	Idle Number Density ($\text{cm}^{-3}\mu\text{m}^{-1}$)	30% Power Number Density ($\text{cm}^{-3}\mu\text{m}^{-1}$)	75% Power Number Density ($\text{cm}^{-3}\mu\text{m}^{-1}$)	100% Power Number Density ($\text{cm}^{-3}\mu\text{m}^{-1}$)
0.002	0.0	0.0	8.1E+4	0.0
0.004	0.0	0.0	0.0	0.0
0.007	4.3E+7	0.0	0.0	0.0
0.012	1.5E+7	0.0	0.0	0.0
0.021	9.2E+6	1.0E+8	0.0	0.0
0.038	0.0	1.4E+8	8.9E+7	5.3E+7
0.067	0.0	1.4E+6	5.5E+7	5.5E+7
0.119	0.0	2.3E+6	4.9E+5	8.3E+4
0.3	0.0	2.1E+6	2.5E+6	2.0E+6

Table A-4. Soot Size Distributions for TF30-P109 Engine Data

Particle Radius (μm)	Idle Number Density ($\text{cm}^{-3}\mu\text{m}^{-1}$)	30% Power Number Density ($\text{cm}^{-3}\mu\text{m}^{-1}$)	75% Power Number Density ($\text{cm}^{-3}\mu\text{m}^{-1}$)	100% Power Number Density ($\text{cm}^{-3}\mu\text{m}^{-1}$)
0.002	0.0	0.0	0.0	4.6E+4
0.004	3.7E+7	0.0	0.0	0.0
0.007	1.1E+8	0.0	0.0	0.0
0.012	5.6E+7	1.8E+8	0.0	0.0
0.021	4.6E+7	1.1E+8	0.0	0.0
0.038	5.1E+6	6.9E+4	2.8E+7	3.0E+7
0.067	4.2E+5	0.0	5.8E+7	3.9E+7
0.119	6.7E+4	2.1E+6	1.9E+5	3.6E+5
0.3	9.0E+4	7.9E+5	2.0E+5	1.5E+6

Table A-5. Soot Size Distributions for TF41-A2 Engine Data

Particle Radius (μm)	Idle Number Density ($\text{cm}^{-3}\mu\text{m}^{-1}$)	30% Power Number Density ($\text{cm}^{-3}\mu\text{m}^{-1}$)	75% Power Number Density ($\text{cm}^{-3}\mu\text{m}^{-1}$)	100% Power Number Density ($\text{cm}^{-3}\mu\text{m}^{-1}$)
0.002	3.1E+6	0.0	0.0	0.0
0.004	4.5E+8	0.0	0.0	3.3E+3
0.007	1.0E+7	0.0	0.0	7.8E+3
0.012	4.6E+6	7.4E+7	0.0	0.0
0.021	9.3E+7	1.0E+8	0.0	0.0
0.038	1.2E+7	2.0E+7	2.6E+6	0.0
0.067	6.7E+5	1.0E+7	6.3E+7	2.3E+7
0.119	8.8E+4	9.2E+5	2.7E+6	1.9E+7
0.3	1.7E+5	7.2E+5	2.8E+6	4.9E+6

Table A-6. Ice Crystal Size Distributions for 4 Cirrus Cloud Models

Particle Radius (μm)	Cs* Number Density ($\text{cm}^{-3}\mu\text{m}^{-1}$)	Ci Uncinus* Number Density ($\text{cm}^{-3}\mu\text{m}^{-1}$)	Warm Ci* Number Density ($\text{cm}^{-3}\mu\text{m}^{-1}$)	Cold Ci* Number Density ($\text{cm}^{-3}\mu\text{m}^{-1}$)
9	1.7E-3	1.4E-3	5.3E-3	2.2E-3
25	2.5E-4	3.1E-4	1.8E-4	1.9E-5
65	8.0E-6	3.0E-5	8.8E-6	2.1E-7
158	3.9E-8	9.8E-6	1.2E-6	1.4E-8
475	0.0	1.4E-6	3.5E-8	0.0

*Cs = cirrostratus, Ci = cirrus

Vita

Captain Michael J. Estes was born on 15 December 1962 in Cleveland, Ohio. He graduated from North Olmsted High School in North Olmsted, Ohio in 1981 and went on to attend Ohio State University under a four year Air Force ROTC scholarship. In 1985, he received a Bachelor of Science degree in Electrical Engineering with a specialization in Computer Engineering. He was commissioned following graduation and began active duty in January 1986 as a Laser Radar Research and Development Project Officer at the Air Force Geophysics Laboratory, Hanscom AFB. During this assignment, he directed signal and data processing system development for several in-house laser radar programs aimed at atmospheric remote sensing applications. In addition, he managed a one million dollar effort to develop advanced coherent solid state lasers for future ground- and space-based laser radar systems. In May 1989, he entered the School of Engineering at the Air Force Institute of Technology, Wright-Patterson AFB, where he studied under the electro-optics program of the Department of Electrical Engineering.

Permanent Address:

6140 Cairo Rd
Westerville, OH 43081

Bibliography

- Air Weather Service. *Forecasting Aircraft Condensation Trails*. Technical Report #AWS/TR-81/001. Scott AFB, IL: HQ AWS/DN, September 1981 (AD-A111876).
- Ancellet, Gerard M., Roberty T. Menzies, and David M. Tratt. "Atmospheric backscatter vertical profiles at 9.2 and 10.6 μm : a comparative study," *Applied Optics*, Vol. 27, No. 23: 4907-4912 (1 December 1988).
- Betz, A. "Behavior of Vortex Systems," NACA TM 713 (translated from *Zeitschrift fur Angewandte Mathematik und Mechanik*, 12, June 1932, XII.3, June 1933).
- Blattner, W. *Utilization Instructions for Operation of the Mie Programs on the CDC-6600 Computer at AFCRL*. Research Note #RRA-N7240. Contract #F19628-70-C-0156. Springfield, VA: National Technical Information Service, 25 October 1972.
- Brown, H.A. and B.A. Kunkel. "Water Vapor, Precipitation, Clouds, and Fog," *Handbook of Geophysics and the Space Environment*, Chpt. 16, edited by Adolph S. Jursa. Springfield, VA: National Technical Information Service (Document Accession Number: ADA 167000), 1985.
- Clifford, Steven F. and Stephen Wandzura. "Monostatic heterodyne lidar performance: the effects of the turbulent atmosphere," *Applied Optics*, Vol. 20, No. 3: 514-516 (1 February 1981).
- Clough, S.A., F.X. Kneizys, E.P. Shettle, and G.P. Anderson. "Atmospheric Radiance and Transmittance: FASCOD2," *Sixth Conference on Atmospheric Radiation*, Williamsburg, VA, May 1986.
- Crow, S.C., and E.R. Bate. "Lifespan of Vortices in a Turbulent Atmosphere," *Journal of Aircraft*, Vol. 13: 476 (1976).
- Edlen, B. "The Refractive Index of Air," *Meteorology*, Vol. 2: 71-80 (1966).
- Fenn, R.W., et al. "Optical and Infrared Properties of the Atmosphere," *Handbook of Geophysics and the Space Environment*, Chpt. 18, edited by Adolph S. Jursa. Springfield, VA: National Technical Information Service (Document Accession Number: ADA 167000), 1985.
- Goodman, Joseph. *Statistical Optics*. New York: John Wiley & Sons, Inc., 1985.
- Gross, Abraham, Madison J. Post, and Freeman F. Hall, Jr. "Depolarization, backscatter, and attenuation of CO_2 lidar by cirrus clouds," *Applied Optics*, Vol. 23, No. 15: 2518-2522 (1 August 1984).
- Guivens, N.R., Jr., S.E. Rafuse, J.R. Hummel, and M.G. Cheifetz. *BACK-SCAT Lidar Backscatter Simulation, User's Manual for Version 1.0*. Scientific Report No. 2, AFGL-TR-88-0331. Springfield, VA: National Technical Information Service, 27 December 1988.
- Hall, Freeman F., Richard E. Cupp, and Seth W. Troxel. "Cirrus cloud transmittance and backscatter in the infrared measured with a CO_2 lidar," *Applied Optics*, Vol. 27, No. 12: 2510-2516 (15 June 1988).

- Hardesty, R.M., R.J. Keeler, M.J. Post, and R.A. Richter. "Characteristics of coherent lidar returns from calibration targets and aerosols," *Applied Optics*, Vol. 20, No. 21: 3763-3769 (1 November 1981).
- Hinkley, E.D., editor. *Laser Monitoring of the Atmosphere*. Berlin, Germany: Springer-Verlag, 1976.
- Huffaker, R.M., A.D. Jelalian, and J.A.L. Thomson. "Laser-Doppler System for Detection of Aircraft Trailing Vortices," *Proceedings of the IEEE*, Vol. 58, No. 3: 322-326 (March 1970).
- and Russell Targ. "Performance Analysis and Technical Assessment of Coherent Lidar Systems for Airborne Wind Shear Detection," *Airborne and Spaceborne Lasers for Terrestrial Geophysical Sensing*, Frank Allario, editor, Proc. SPIE 889, pp. 65-76. Bellingham, WA: Society of Photo-Optical Instrumentation Engineers (1988).
- Iskander, Magdy F., H.Y. Chen, and J.E. Penner. "Optical scattering and absorption by branched chains of aerosols," *Applied Optics*, Vol. 28, No. 15: 3083-3091 (1 August 1989).
- Johnson, J.H., E.D. Erickson, and D.J. Knight. *Analysis of Particulates in the Exhaust Plume of a J52-P3 Turbojet Engine at Military Power, Interim Report, October 1983-September 1984*. Report No. NWC-TP-6618. Springfield, VA: National Technical Information Service, March 1985 (AD-A157840).
- Kent, G.S., P.H. Wang, U. Farrukh, A. Deepak, and E.M. Patterson. *Development of a Global Model for Atmospheric Backscatter at CO₂ Wavelengths*. NASA Contractor Report 3959. Contract #NAS8-35594. Springfield, VA: National Technical Information Service, February 1986.
- Koenig, Lt Col George G. Personal Correspondence. Geophysics Laboratory (AFSC), Hanscom AFB, MA, February through July 1990.
- and Steven B. Alejandro. Personal Correspondence. Geophysics Laboratory (AFSC), Hanscom AFB, MA, June through July 1990.
- Lutchen, K.R. "Strategic Detection of Subsonic Aircraft Wakes: A Theoretic Assessment," Report #CMT-59. Contract F19628-83-C-0002. Lexington, MA: MIT Lincoln Laboratory, 1 November 1984 (AD-C035585).
- Mathews, Larry A., et al. *Analysis of Particulates in the Exhaust Plume of a TF30 Engine at Military Power, Interim Report, Fiscal Year 1983*. Report No. NWC-TP-6508. Springfield, VA: National Technical Information Service, May 1984 (AD-A142510).
- McCartney, Earl J. *Optics of the Atmosphere*. New York: John Wiley & Sons, Inc., 1976.
- Measures, Raymond M. *Laser Remote Sensing*. New York: John Wiley & Sons, Inc., 1984.
- Menzies, Robert T., and R. Michael Hardesty. "Coherent Doppler Lidar for Measurements of Wind Fields," *Proceedings of the IEEE*, Vol. 77, No. 3: 449-462 (March 1989).

- National Oceanic and Atmospheric Administration (NOAA), National Aeronautics and Space Administration (NASA), and United States Air Force (USAF). *U.S. Standard Atmosphere, 1976*. Washington, D.C.: U.S. Government Printing Office, October 1976.
- National Research Council (NRC). *The Effects on the Atmosphere of a Major Nuclear Exchange*. Washington, D.C.: National Academy Press, 1985.
- Neilson, J.N., and R.G. Schwind. "Decay of a Vortex Pair Behind an Aircraft," *Aircraft Wake Turbulence and Its Detection*, edited by Olsen and Goldberg. Plenum Press, 1971.
- Pitz, Robert W. *Advanced Optical Smoke Meters for Jet Engine Exhaust Measurement. Final Report*, NASA CR-179459. Contract #NAS3-24084. Springfield, VA: National Technical Information Service, 1987.
- Post, Madison J. "Aerosol backscattering profiles at CO₂ wavelengths: the NOAA data base," *Applied Optics*, Vol. 23, No. 15: 2507-2509 (1 August 1984).
- *Atmospheric Infrared Backscattering Profiles: Interpretation of Statistical and Temporal Properties*. NOAA Technical Memorandum ERL-WPL-122. Washington, D.C.: Government Printing Office, 1985.
- Rosen, J.M., and R. Greigor. "Jet Engine Soot Emission Measured at Altitude," *Journal of Aircraft*, Vol. 11, No. 3: 243-245 (March 1974).
- Rothermel, Jeffry, David A. Bowdle, J. Michael Vaughan, and Madison J. Post. "Evidence of a tropospheric aerosol backscatter background mode," *Applied Optics*, Vol. 28, No. 6: 1040-1042 (15 March 1989).
- Shettle, Dr Eric P. Telephone Interview. Geophysics Laboratory (AFSC), Hanscom AFB, MA, 23 April 1990.
- Schreiber, Dr Paul. Telephone Interview. Wright Research and Development Center, Wright Patterson AFB, OH, 18 July 1990.
- Sonnenschein, C.M. and F.A. Horrigan. "Signal-to-Noise Relationships for Coaxial Systems that Heterodyne Backscatter from the Atmosphere," *Applied Optics*, Vol. 10, No. 7: 1600-1604 (July 1971).
- Spears, David. Telephone Interview. MIT Lincoln Laboratory, Applied Physics Division, Lexington, MA, 18 July 1990.
- Spicer, C.W., et al. *Aircraft Emissions Characterization: TF41-A2, TF30-P103, and TF30-P109 Engines, Final Report*, December 1985-March 1987. Contract F08635-85-C0122. Springfield, VA: National Technical Information Service, December 1987 (AD-A192053).
- Spreiter, J.R., and A.H. Sacks. "The rolling up of the trailing vortex sheet and its effect on the downwash behind wings," *J. of the Aeronautical Sciences*, Vol. 12, No. 21 (1951).
- Takano, Yoshihide, and Kuo-Nan Liou. "Solar Radiative Transfer in Cirrus Clouds," *Journal of the Atmospheric Sciences*, Vol. 46, No. 1: 3-36 (1 January 1989).

- Thomson, J. Alex, R. Milton Huffaker, Michael J. Kavaya, and Michael L. Smith. *Feasibility Study for Aircraft Wake Vortex Detection Using a Pulsed Coherent Laser Radar*, Report #CTI-TR-8903. Contract #F33615-88-C-1756. Boulder, CO: Coherent Technologies, Inc., October 1989.
- Tipler, Paul A. *Modern Physics*. New York, NY: Worth Publishers, Inc., 1987.
- van de Hulst, H.C. *Light Scattering by Small Particles*. New York: Wiley, 1957.
- Verdeyen, Joseph T. *Laser Electronics*. Englewood Cliffs, NJ: Prentice-Hall, Inc., 1989.
- Wander, Dr Joseph. Telephone Interview. HQ AFESC/RDVS, Tyndall AFB, FL, 16 August 1990.
- Warren, Stephen G. "Optical constants of ice from the ultraviolet to the microwave," *Applied Optics*, Vol. 23, No. 8: 1206-1225 (15 April 1984).
- Young, A.T. "Revised depolarization corrections for atmospheric extinction," *Applied Optics*, Vol. 19: 3427-3428 (1980).
- Zhao, Yanzeng and Madison J. Post. "Receiving Efficiency for Pulsed Coherent Lidars," *Coherent Laser Radar: Technology and Applications*, Proc. SPIE 1181, pp. 186-189. Bellingham, WA: Society of Photo-Optical Instrumentation Engineers (1989).
- Zrnic, Dusan S. "Estimation of Spectral Moments for Weather Echoes," *IEEE Transactions on Geoscience Electronics*, Vol. GE-17, No. 4: 113-128 (October 1979).
- "Spectral Moment Estimates from Correlated Pulse Pairs," *IEEE Transactions on Aerospace and Electronic Systems*, Vol. AES-13, No. 4: 344-354 (July 1977):